Computer Simulation of Cardiac Electrical Activity by Three-dimensional Whole Heart and Heterogeneous Oscillator Models

TOHOKU UNIVERSITY

Graduate School of Biomedical Engineering

Computer Simulation of Cardiac Electrical Activity by Three-Dimensional Whole Heart and Heterogeneous Oscillator Models

A dissertation submitted for the degree Doctor of Philosophy

(Biomedical Engineering)

Department of Biomedical Engineering

by

Elena RYZHII

2015

Abstract

Cardiovascular diseases are the leading cause of death in the modern industrialized world. The most dangerous cardiac arrhythmias are ventricular tachycardia and fibrillation, which increase heart rate and, in severe case, result in chaotic heart muscle contraction leading to sudden cardiac death. Despite intensive research efforts, the mechanisms involved in the origin and maintenance of these arrhythmias remain unclear. Nowadays, mathematical modeling and computer simulations have proved to be perfect instruments to integrate the quantitative data from research and experiments with a qualitative understanding for safely testing different hypothesis without any cardiac risk for the patient.

Computer modeling of cardiac electrophysiology became very important in understanding real processes taking place in healthy and diseased hearts. The most well-known and widely used in clinical and theoretical research set of physiological signals produced by electrical activity of the heart is electrocardiogram (ECG). The ECG is a record of electric potentials generated by the heart on the body surface because of propagation of activation and recovery waves through cardiac muscle tissue.

For the modeling of the electrical processes in the heart, various heart models with different levels of details have been proposed and utilized.

In our thesis, we present two different approaches to study cardiac arrhythmias: modeling with three-dimensional whole heart model and heterogeneous oscillator model of cardiac conduction system.

This dissertation consists of the following chapters:

- Chapter 1 - Introduction

  The chapter presents background and general information on the heart anatomy, physiology on organ and cellular levels.

- Chapter 2 - Computer simulation of atypical Brugada syndrome with whole heart model

  a) Mathematical description of three-dimensional Wei-Harumi heart model, including propagation of the excitation front, cardiac electric source, and calculation of body surface electrocardiographic potentials are given.

  b) Computer simulation of atypical Brugada syndrome

This chapter deals with the development and implementation of computer simulation model for the investigation of sudden cardiac death disease due to specific ventricular arrhythmia (fibrillation).

- Chapter 3 - Study of T wave morphology with combined biventricular and ion-channel models

  a) The chapter presents combination of the heart model with our modified ion-channel model of ventricular myocytes in order to incorporate M cells absent in the original Wei-Harumi model.

  b) With the developed combined model, we investigated the role of M cells in genesis of T wave by verifying different spatial action potential distributions.

- Chapter 4 - Computer simulation of cardiac conduction system with heterogeneous oscillator model

  a) In this chapter, we describe a model of cardiac electrical system consisting of a network of heterogeneous oscillators described by nonlinear differential equations. We used modified van der Pol equations for the cardiac pacemakers and FitzHugh-Nagumo-type equations for atrial and ventricular muscles.

  b) We present the investigation of diffusive voltage and current couplings between natural pacemaker oscillators in the heterogeneous coupled oscillator model. We study the synchronization behavior of the oscillator system for normal and fast cardiac sinus rhythms and reproduce different mode-locked cases, which correspond to incomplete atrioventricular blocks.

- Chapter 5 - Summary and future work

  In this chapter the contents of this thesis is summarized, and some possible directions for future research are proposed.

Contents

List of figures

List of tables

Chapter 1

Introduction

1.1 Background

The human heart is a remarkably engineered oscillator that acts as a variable speed biomechanical pump. This pump continuously works throughout a person's life, under control of electrical impulses originating in specialized cells forming special conduction system. The initialization of the impulses is caused by the flow of ions across the outer cell membrane and give rise to a periodic wave of excitation that spreads through the entire heart. This excitation wave initiates and coordinates the contraction of the cardiac cells delivering blood to the whole body. The heart is disturbed when the normal coordination of its different parts fails. These dangerous and sometimes fatal situations (so called cardiac arrhythmia) can occur due to various reasons. The great challenge of heart research is to understand the mechanism, which causes this sudden change from synchronized contraction to disorganized contraction throughout the heart. Once we understand more about the underlying mechanism, we can better devise ways of detecting and preventing sudden cardiac death.

Cardiac arrhythmias and sudden cardiac death are among the most common causes of death in the industrialized world [1]. Theoretical studies into the mechanisms of cardiac arrhythmias form a well-established area of research. One of the most important applications of these theoretical studies is the simulation of the human heart, which is important for a number of reasons. First, the possibilities for doing clinical and experimental research involving human hearts are very limited. Second, animal hearts used for experimental studies significantly differ from human hearts in heart rate, in size, action potential duration, shape, and restitution, vulnerability to arrhythmias, and so on. Finally, cardiac arrhythmias, especially ventricular, are three-dimensional processes whereas experimental observations are still mostly constrained to heart surface recordings. Computer simulations of the arrhythmias can help to overcome these problems.

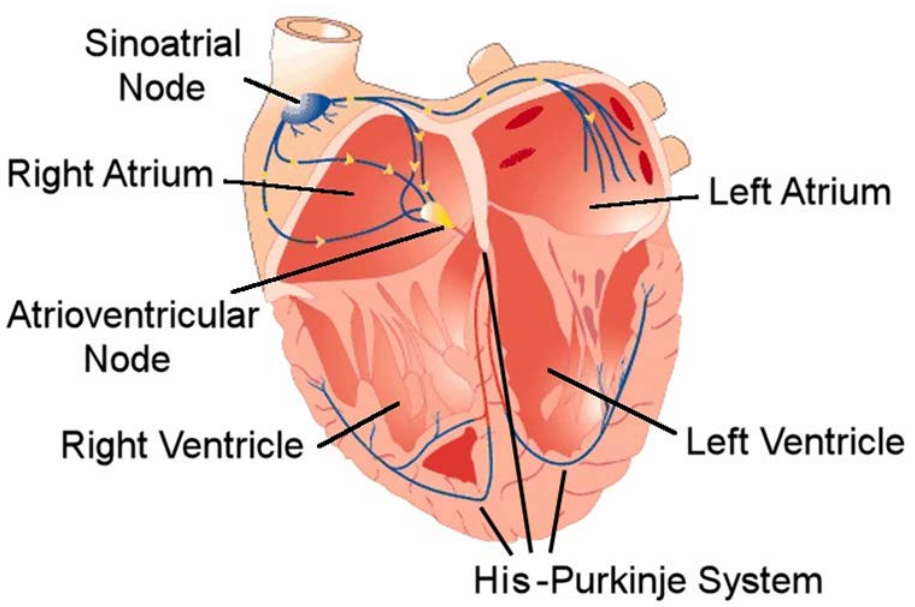

Figure 1.1: The four-chamber heart and its conduction system (adopted from [2]).

1.2 Heart anatomy and electrophysiology

The mechanical activity on blood pumping is controlled by heart's specialized electrical conduction system (Fig. 1.1). This system consists of sinoatrial node (SA), atrioventricular node (AV), and His-Purkinje system (HP), which includes bundle of His (HIS), Purkinje fibers (PKJ), and left and right bundle branches (BB). The rhythmic signal is normally generated at the SA node automatically [3]. The electrical excitation wave then spreads through out the left and right atria and causes their contraction. The wave then reaches the AV node and moves quickly down to the HP. The fast travel of the excitation wave through the left and right BB helps to spread the electrical wave evenly throughout the left (LV) and right (RV) ventricles and causes different parts of the ventricles to contract almost simultaneously. After the contraction, the atria and ventricles relax and wait for next waves of electrical excitation. This process occurs during each normal heartbeat.

Microscopically, the heart is composed of a network of muscle fibers. Each fiber consists of millions of cells (cardiomyocytes) (Fig. 1.2). The boundary of each heart cell is an excitable membrane. The membrane has a resting transmembrane potential resulting from differences in the membrane permeability to the various ions and the

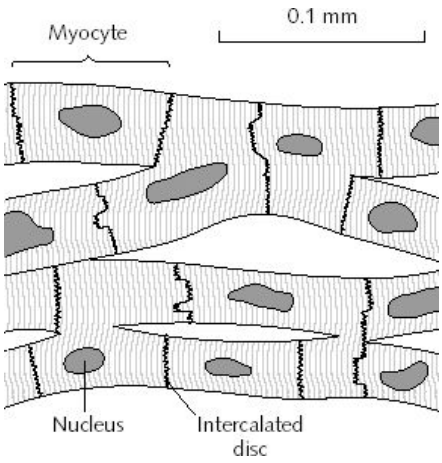

Figure 1.2: Schematic view of myocardial cells (cardiomyocytes) [4].

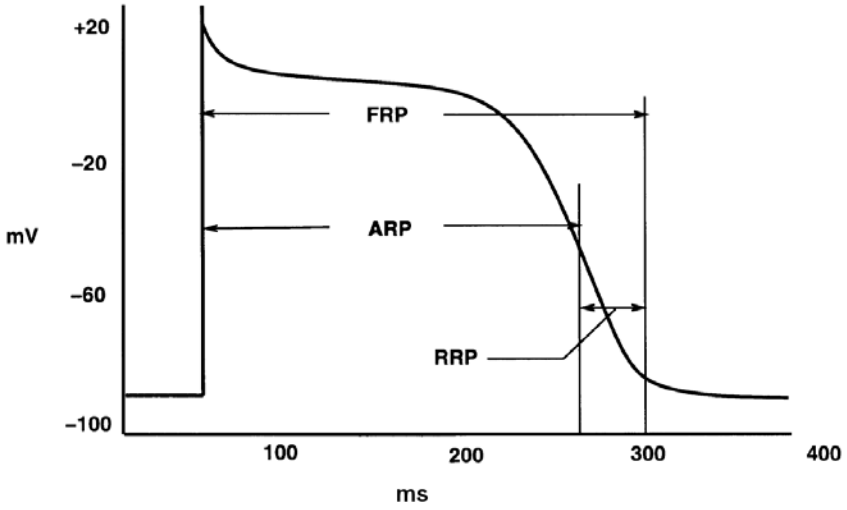

Figure 1.3: Typical action potential of ventricular myocyte, where FRP is functional refractory period, ARP is absolute refractory period, and RRP is relative refractory period, respectively.

differences in the concentrations of the ions on either side of the membrane. Once the membrane has been depolarized by raising its transmembrane potential to its threshold, it responds quickly with an even larger change of transmembrane potential. The transmembrane potential stays at higher level for a while then gradually relaxes back to its resting value. This is called an action potential (AP) (Fig. 1.3).

For understanding the electrophysiology of cardiac myocyte, the *principle of refractoriness* is very important. A refractory period is the amount of time taking to an excitable membrane to be ready for an appropriate response to the next stimulus after returning to the resting state following the previous excitation.

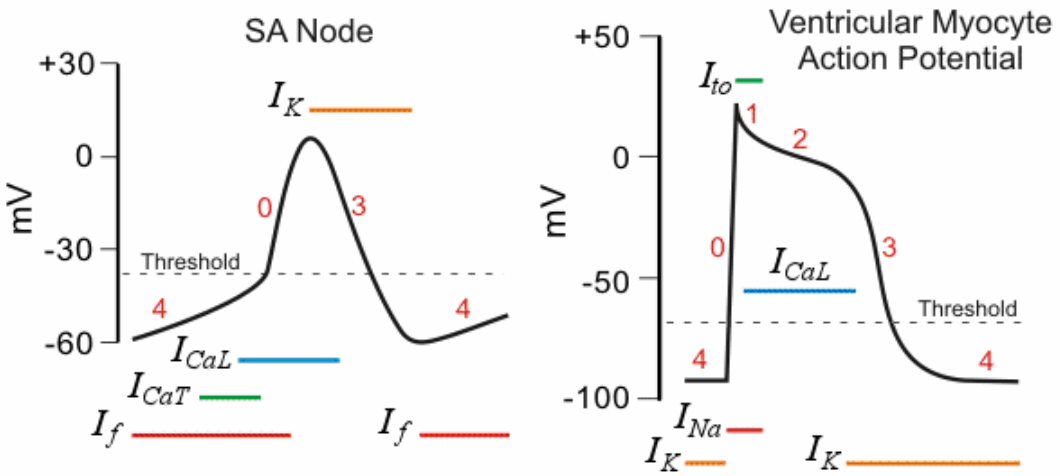

Figure 1.4: Electrochemical phases of action potentials for pacemaker (left) and non-pacemaker (right) cardiac cells (adopted from [5]).

After action potential begins, the membrane will not respond normally to second stimulus. This time is called the refractory period and can be divided into the absolute and relative refractory periods as illustrated in Fig. 1.3. The absolute refractory period (ARP) is the period in which no stimuli can excite the membrane. During the ARP the membrane cannot respond at all. In a ventricular muscle cell (cardiomyocyte) the ARP spans the duration of the plateau and the initial period of rapid repolarization. The ARP is followed by shorter relative refractory period (RRP). The RRP is the period in which only stronger than normal external stimuli can excite the membrane for initiating another AP and the response is smaller and weaker than normal. The functional refractory period (FRP) is the period, which consists of ARP and RRP.

1.3 Electrochemical processes in cardiomyocyte

Living cells maintain a difference in electrical potential between their interiors and their external environments [6]. This potential is called the resting potential (phase 4 on Fig. 1.4).

In pacemaker cells found in SA and AV nodes, HIS, BB and PKJ, phase 4 is the spontaneous depolarization that triggers the action potential once the membrane potential reaches threshold between -40 and -30 mV). Phase 0 is the depolarization phase of the action potential. This is followed by phase 3 repolarization.

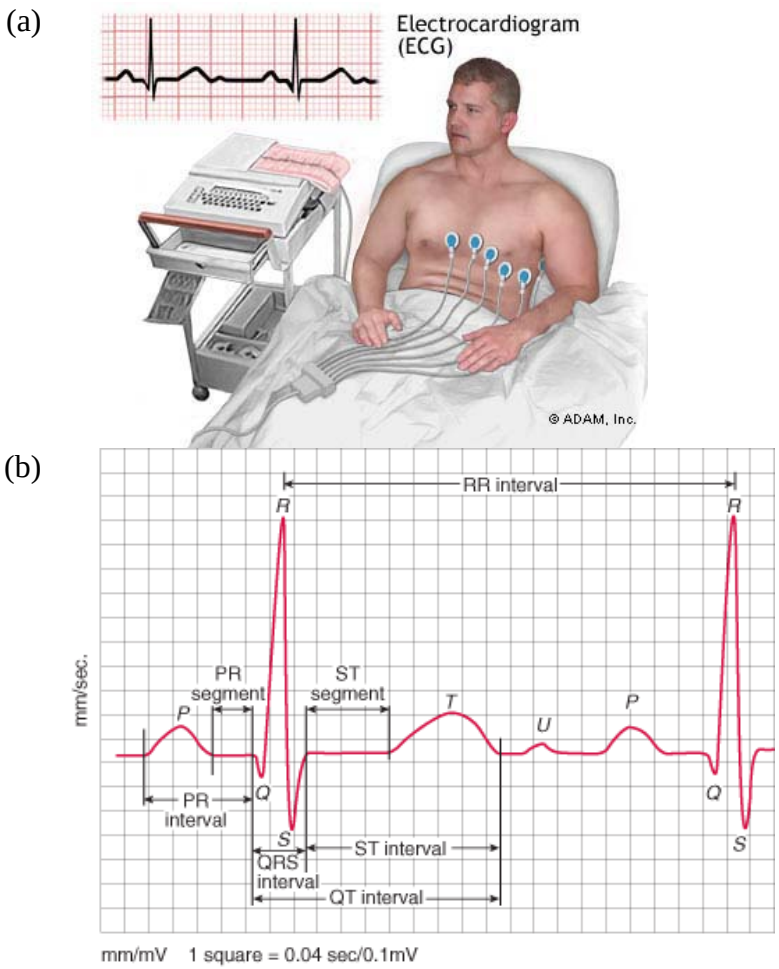

Figure 1.5: Electrocardiography device (a) and typical electrocardiogram (b) [8].

After complete repolarization at about -60 mV the ion channels open that conduct slow, inward mixed sodium-potassium current called "funny" current causing the spontaneous depolarization (initiating phase 4).

In contrast to pacemaker cells, non-pacemaker cells have a true resting membrane potential (phase 4) that remains near the equilibrium potential for K+ and is about -90 mV. The resting potential is associated with K+ currents, when positive potassium ions are leaving the cell and making the intracellular membrane potential more negative. At the same time, fast sodium channels and L-type slow calcium channels are closed. A rapid depolarization (phase 1) is caused by a transient increase in fast Na+ channel conductance through fast sodium channels (a threshold voltage of about -70 mV). This increases depolarizing inward directed Na+ currents (I_{Na}) creating "fast response" action potentials. At the same time sodium channels open, outward directed K+ currents (I_{to}) all as potassium channels close. These two conductance changes

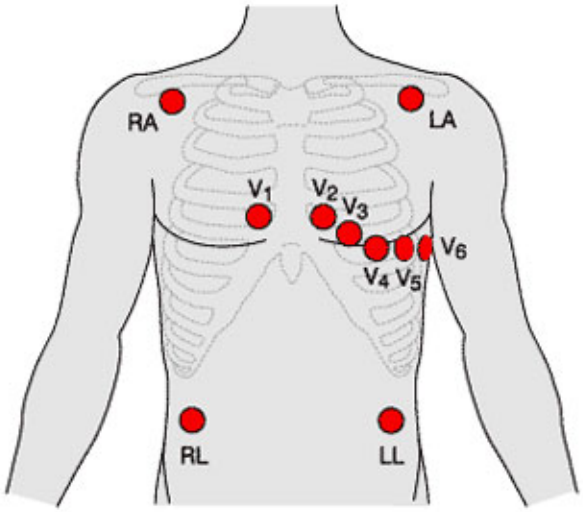

Figure 1.6: Positions of ECG leads [9].

move the membrane potential away from resting state (which is negative) and closer toward the equilibrium potential for sodium, which is positive. The an initial repolarization that is caused by the opening of a special type of transient outward K+ channel which causes a short-lived, hyperpolarizing outward K+ current. However, simultaneous large increase in slow inward calcium current (I_{CaL}) delays the repolarization and produces a plateau phase (phase 2) prolonging action potential of cardiac myocyte. Slow repolarization (phase 3) occurs when outward K+ current increases; along with the inactivation of L-type Ca++ channels (decreased Ca current).

1.4 Body surface ECG

The electrical activity of the heart can be measured from the human body surface by attaching electrodes to the chest [7]. This traditional method of detecting the electrical activity is called the electrocardiography [Fig. 1.5(a)]. A typical electrocardiogram (ECG) is shown on Fig. 1.5(b). Each of the electrochemical processes described above can be detected on body surface ECG as an averaged signal of the temporal and spatial gradients generated during each phase.

During each heartbeat, a healthy heart will have an orderly progression of a depolarization wave triggered by the SA node cells, spreading out through atria and

ventricles. This is detected as tiny changes in the voltage between two electrodes placed either side of the heart, and displayed as a line either on a screen or on paper.

Usually, more than two electrodes are used, and they can be combined into a number of pairs (For example: left arm (LA), right arm (RA), and left leg (LL) electrodes form the three pairs LA+RA, LA+LL, and RA+LL). The output from each pair is known as a lead. Each of the 12 leads represents a particular orientation in space (Fig. 1.6).

Bipolar limb leads (frontal plane):

Lead I: RA (-) to LA (+) (Lateral)

Lead II: RA (-) to LL (+) (Superior Inferior)

Lead III: LA (-) to LL (+) (Superior Inferior)

Augmented unipolar limb leads (frontal plane):

Lead aVR: RA (+) to [LA and LL] (-) (Rightward)

Lead aVL: LA (+) to [RA and LL] (-) (Leftward)

Lead aVF: LL (+) to [RA and LA] (-) (Inferior)

Unipolar (+) chest leads (horizontal plane):

Leads V1, V2, V3: (Right precordial)

Leads V4, V5, V6: (Lateral)

Electrical excitation in the atria (atrial depolarization) manifests on the ECG [Fig. 1.5(b)] as P wave, while ventricular depolarization is seen as the QRS complex. Ventricular repolarization is reflected in the T wave. During normal rhythm, atrial repolarization (Ta wave) is not seen on ECG since it coincides with QRS complex. The origin of the U wave is unknown. This wave possibly results from the repolarization of Purkinje fibers.

ECG abnormalities are related to changes in cellular AP morphologies, which may be due to altered cell-to-cell coupling, heart disease, congenital ion-channel abnormalities, drug intervention, or electrolyte imbalance. In general, membrane potential, extracellular and intracellular ionic concentrations, as well as regulatory proteins that modulate the activity of channels influence ionic currents. The shape and duration of the AP is therefore an integrative cellular feature that is a result of the interaction of many underlying cellular processes.

Since whole-heart function, both in physiological and diseased states, often reflects the processes that occur in individual myocytes, it is critical to understand the physiological properties of single cardiac myocytes.

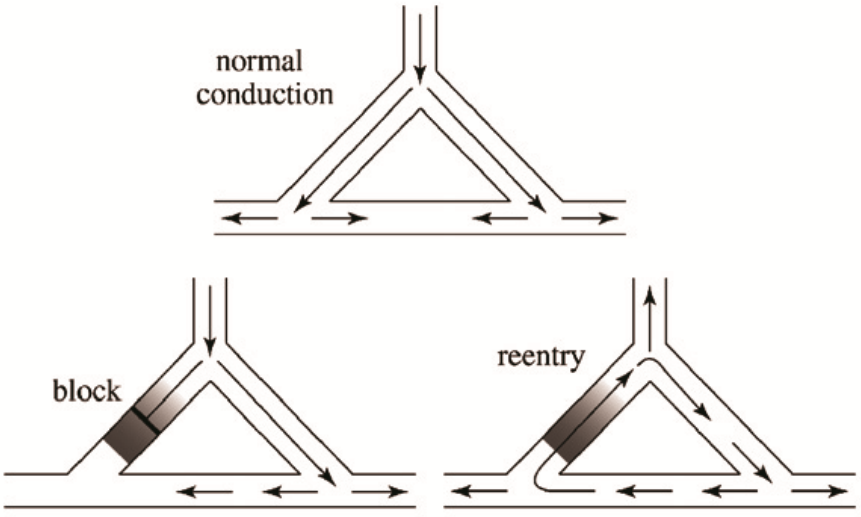

Figure 1.7: Schematic representation of normal conduction and a reentrant circuit [10].

1.5 Reentry and fibrillation

One of the most interesting forms of abnormal cardiac conduction is reentry. During reentry, an excitation wave front remains active while a neighboring region of cells has recovered from the previous excitation thus permitting the excitation wave front to reenter the neighboring region. Figure 1.7 shows a simple situation when a reentry of electrical excitation wave is formed. In normal heart, an impulse is generated by the SA node and decays when the whole heart has been activated. Reentry occurs if the same impulse continues to re-excite tissue. The presence of a unidirectional block, slow conduction and short refractory periods facilitate a formation of re-entrant circuit. Reentry wave can be more complicated than what is shown here. Self-sustaining reentry loops of activity, which means that the reentry can go on without any external help, are believed to be the underlying mechanism for the potentially lethal rhythm disturbances such as ventricular tachycardia and fibrillation.

In the case of ventricular tachycardia, the reentry wave front is thought to repetively traverse a loop around a region of ventricular tissue so that the loop can generate its own rhythm, which is usually faster than the normal sinus rhythm. In ventricular fibrillation, it is believed that there are many wandering small reentrant loops so that many part of the ventricle contract independently.

Chapter 2

Computer simulation of atypical Brugada syndrome with whole-heart model

2.1 Introduction

The term “whole-heart model” was first used by Lorange and Gulrajani in 1988 [11]. In narrow sense, whole-heart model may refer to three-dimensional heart models, which include realistic geometry and are capable of simulating the activation process of the heart and the body surface ECG potentials. In a broad sense, the whole-heart model can be characterized in the following way:

1) Whole-heart model generally means a macroscopic model, which represents the entire heart or a portion of the heart such as the left ventricle or both ventricles. Most whole-heart models include realistic heart geometry and anatomy.

2) The macroscopic nature of the whole-heart model also lies in the scale of its elements. The elements of a whole-heart model usually have a size ten or more times larger than the size of true cardiac cell (0.05-0.1 mm). In this sense, the element in a whole-heart model is lumped model of tissue.

3) The main purpose of a whole-heart model is to investigate the global behavior of the heart. Therefore, some whole-heart models do not incorporate a cellular mechanism directly relating the activation process of the whole heart to the transmembrane ionic current. Rather, these models employ Huygens’ Principle of propagation to simulate the excitation process of the heart.

4) Most whole-heart models are accompanied by a torso model of the body, aimed at reproducing surface ECG potentials. This kind of models yields clinically comparable ECG waveforms. In this sense, the whole-heart models are closer to the clinical

Table 2.1: Comparison of whole heart models.

N. Trayanova group, Johns Hopkins Univ. (USA)		cellular models	reaction-diffusion	electro-mechanics	ECG	super computer
A. McCulloch group, Univ. of California (USA)	Continuity 6 environment	cellular models	reaction-diffusion	electro-mechanics	ECG	super computer
B. Rodriguez group, Univ. of Oxford (UK)	CHASTE package	cellular models	reaction-diffusion	electro-mechanics		super computer
G. Seemann, O. Dössel group, Karlsruhe Institute of Technology (Germany)	acCELLerate package	cellular models	reaction-diffusion	electro-mechanics	ECG	super computer
G. Plank, Med. Univ. of Graz (Austria), E. J. Vigmond, Univ. of Calgary (Canada)	CARP	cellular models	reaction-diffusion	electro-mechanics		super computer
M. Potse, Univ. of Lugano (Switzerland)		cellular models	reaction-diffusion (prev. CA)		ECG	super computer
T. Hisada group, Univ. of Tokyo (Japan)	UT-Heart	cellular models	reaction-diffusion	electro-mechanics blood flow	ECG	super computer
A. van Oosterom, T. Oostendorp, P. van Dam Radboud, Univ. in Nijmegen (Netherlands)	ECGSIM		equivalent surface source model		ECG	realtime on normal desktop PC, education
Peter Spector group, Univ. of Vermont (USA)	VisibleEP	cellular models	cellular automaton		ECG	realtime on normal desktop PC, education
Wei-Harumi model Univ. of Aizu (Japan)	Cardiomaster	cellular models	cellular automaton		ECG	realtime on normal desktop PC

ECG waveforms.

The majority of the modern whole heart models simulate propagation of a wave of transmembrane potential by solving a large number of the mono- or bidomain reaction–diffusion partial differential equations (for example [12-15]) over the volume of the heart. Active processes of ion exchanges across myocyte membranes are represented by different cellular ionic models. In these models, sets of ordinary differential and algebraic equations describe current flow through ion channels, pumps, and exchangers [16].

Some models take into account the mechanical function of the heart, such as deformation of ventricles during the contraction (see, for example, [17-19]) and even blood flow in/out the cardiac chambers [20].

For solutions to electrophysiological or electromechanical whole heart models mostly finite element method (FEM) is used. Thus, the governing equations should be solved on a spatially discretized heart volume represented by the computational mesh. The electrical and mechanics parts of the model have different requirements regarding the size of elements, as well as the element type, thus such combined model may require two different computational meshes. Both the electrical and mechanical meshes of the heart can be generated directly from segmented MR images.

Simulations with the whole heart electromechanical models are typically performed on parallel high performance computing hardware and require a lot of computational time. In contrast, the whole heart model used in this work being rather simple, allows easy manipulation of cellular structure of the model heart and yields adequate results in with utilization of ordinary desktop personal computers over reasonably short simulation time. Comparison of main features of recent whole heart models is presented in the Table 2.1.

2.2 Wei-Harumi heart model

2.2.1 General description

Methodology in heart modeling includes many kinds of technical issues such as the heart and torso shape modeling techniques, the way of inclusion of specialized conduction system, incorporation of rotating fiber directions, assignment of electrophysiological properties, propagation models, the cardiac electric source, and the volume conductor problem to solve electrocardiograms.

The 3D heart model utilized in this study was first proposed by Aoki *et al*. [21] based on theoretical studies of the T-wave by Harumi *at al*. [22]. The model was expanded to the whole heart by Wei *at el*. [23-26] and allows simulating the body surface ECGs, and recently the catheter-based intracardiac potentials, based on anatomical and electrophysiological settings [27]. The model was utilized in different simulation studies (see, for example, [28-30]). The model was implemented in the

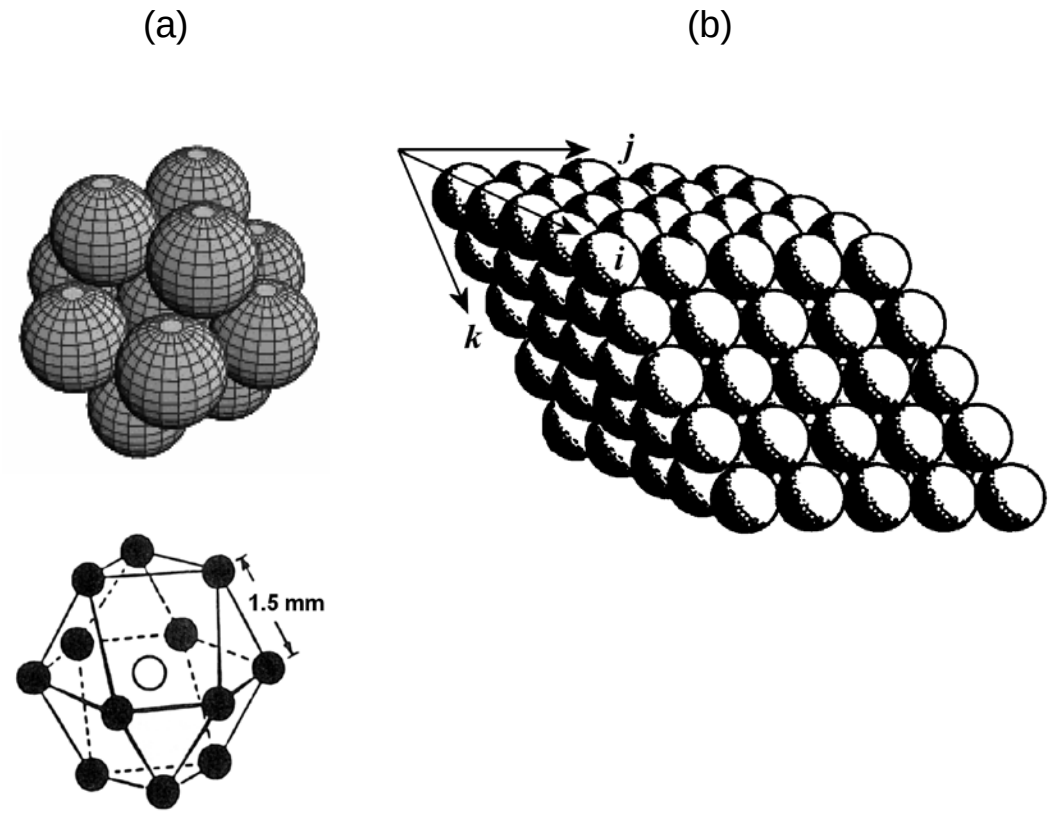

Figure 2.1: Cubic close packing cluster (a) and configuration of heart model cells (b) (adopted from [22] and [32]).

Cardiomaster 2.0 heart simulation software [31] for Microsoft Windows operating system.

The heart model is constructed in an inclined, 3D coordinate system with equal axial angles of 60^{o}. The heart is discretized by parallel planes *i = const*, *j = const*, and *k = const* into the discrete volume of 56×56×90 voxels, which are called model cells. Such construction represents the cubic close-packed structure (known to be the densest possible packing of equal spheres), where each voxel is in direct contact with 12 adjacent neighbors which are in equal distance of 1.5 mm from it (Fig. 2.1). The total number of model cells is approximately 55,000. The model has realistic heart shape. The cells are categorized into different cell types including the atria, the ventricles, and the specialized conduction system. The AV node model cells connect the atrial model cells in one end and HIS model cells in another. One layer of PKJ fibers is arranged in the endocardial surfaces of the ventricles. Excitation automaticity is assigned only to SA node model cells. Other types of cells are activated from neighboring cells when those cells became excitable. Extra stimuli can be set at any

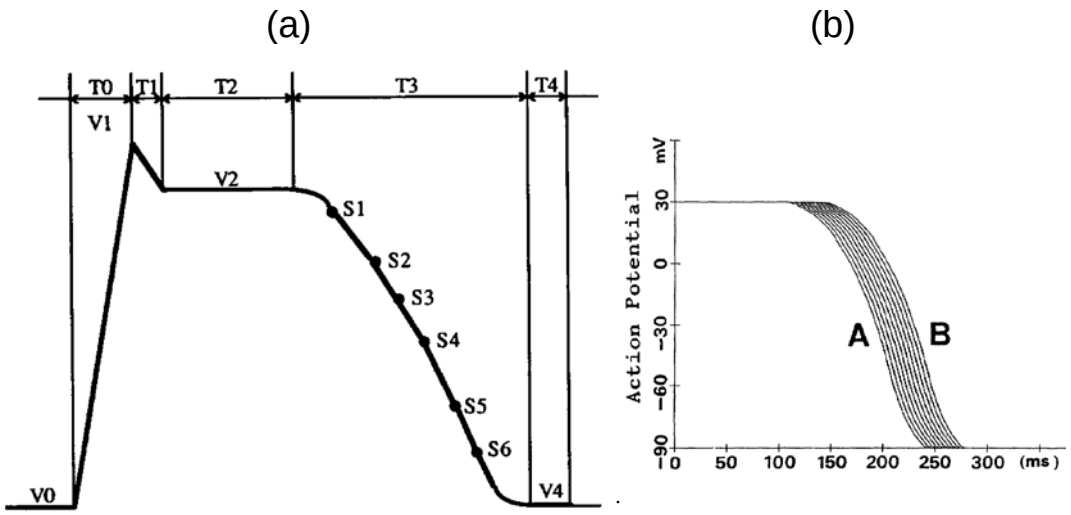

Figure 2.2: (a) - Definition of an action potential in Cardiomaster 2.0 software: phases 0, 1, 2, and 4 are simplified by lines that are determined by their duration (T0, T1, T2, and T4) and voltages (V0, V1, V2, and V4). Phase 3 is represented by a curve interpolating samples of S1 through S6 [21]. (b) - Distribution of AP durations from epicardium (A) to endocardium (B) in Wei-Harumi model [22].

location in the heart model. The Purkinje network is mounted in the endocardial surface of heart model and its distribution was adjusted based on Durrer's data of isochrones of human heart excitation [33]. The overall setting of the specialized conduction system is adjusted to generate normal patterns of excitation over the heart and normal ECG waveforms. The cell-by-cell fiber directions are calculated for ventricular cells so that the ventricular fibers orientations rotate gradually from the epicardium to the endocardium in about 90^{o} [34]. The incorporated anisotropy in excitation propagation and in electrical conductivity is based on the rotating fiber orientations.

In the Cardiomaster 2.0 software, AP is parametric (not calculated), but is set as input parametres to the heart model based on experimental data. At first, the AP waveform of each phase is mathematically defined and is taken as the sum of phases 0 through 4 [Fig. 2.2(a)]. The period of phase 2 is distributed over the entire heart model so that the AP duration (APD) is distributed as described above. Phase 3 is defined by a curve through interpolation (second-order Lagrange interpolation) of sample data. In the simulations, APD is equivalent to full recovery time (FRT). For simplicity, the absolute refractory period (ARP) is defined independently. The period

after ARP and before full recovery time (FRT minus ARP) is considered as relative refractory period (RRP) (see also Fig. 1.3).

It is known that APD of myocardial cells varies depending on their location in the heart in accordance with an old concept of ventricular gradient. To distribute the defined APD over the ventricles of the model a sequence number, SQ(*i*,*j*,*k*) is assigned to each model cell from the epicardium toward the endocardium and from the base to the apex. The stimuli are applied to the epicardial model cells in the base area, instead of the whole epicardium, to yield an epicardial-to-endocardial and base-to-apex propagation. The parameter GRD is used to specify the difference in APD (in ms) between each sequential number. The value of the APD for a model cell (*i*, *j*, *k*), APD(*i*,*j*,*k*), is determined by

$$\mathrm{APD}(i,\, j, k) = \mathrm{APD}_{\mathrm{d}} + \mathrm{GRD} \cdot \mathrm{SQ}(i,\, j, k)\,, \tag{2.1}$$

where $\mathrm{APD}_{\mathrm{d}}$ was the predefined value for the cell type. A positive GRD value yields a distribution where the APD is shortest on the epicardium and apical region and gradually changes along the directions from the epicardium to the endocardium and from the apex to the base [22] [see Fig. 2.2(b)]. Thus, Wei-Harumi model did not take into account the current concept of M cells during the early time of development. Later in Chapter 3, in contrast to the standard definition of AP we calculate APD values and distribution taking into account modern M cell concept utilizing biophysically based ion-channel model and a special algorithm for automatic distribution of three types of myocardial cells [30].

As additional feature of the model, a random APD distribution can be defined with parameter DVT that specifies the deviation of APD from its predefined value. In this case, the APD for a model cell (*i*, *j*, *k*) is modified by

$$\mathrm{APD}(i,\, j, k) = \mathrm{APD}_{\mathrm{d}} + \mathrm{DVT} \cdot \mathrm{NR}\,, \tag{2.2}$$

where NR is a random number in the range (-1, 1). The random distribution of the APD is used in Cardiomaster as a measure of vulnerability of ventricles to arrhythmia and fibrillation.

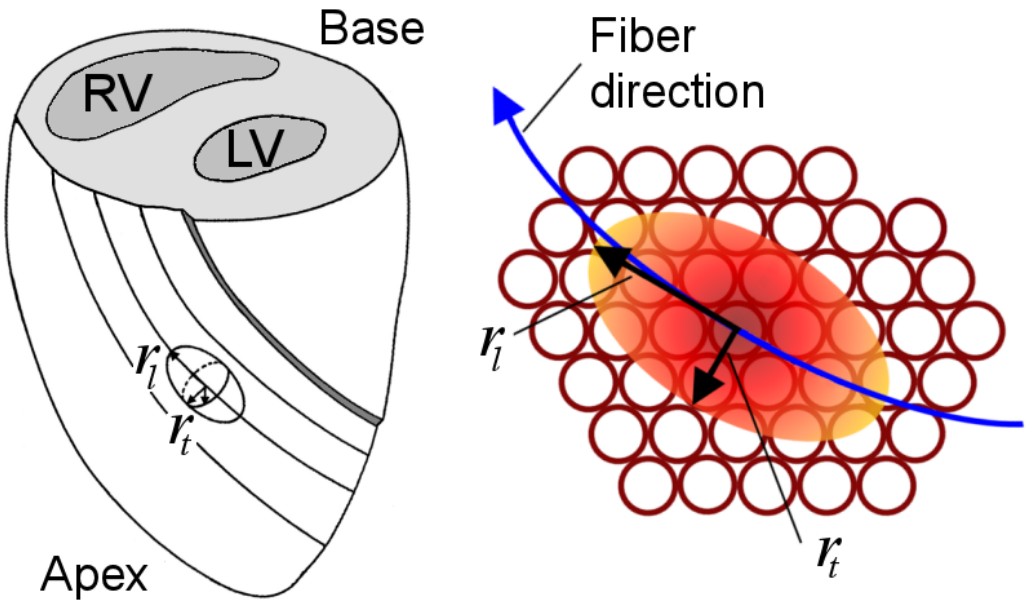

Figure 2.3: Ellipsoidal wavelet of excitation based on local muscle fiber direction. r_l and r_t are the semiaxis along the longitudinal and transversal fiber directions. RV and LV are the right and left ventricles, respectively (adopted from [26]).

Another important property of the model is that the APs of the model cells are not static, but taking dynamic values during the simulation depending on the coupling interval (CI) as a real heart does, according to Harumi *et al.* [32]. This property is defined by a parameter called dynamic coefficient (DC) so that the value of APD at time instant s is determined by

$$\mathrm{APD}(s) = \mathrm{APD}(s-1) + \mathrm{DC} \cdot \Delta\mathrm{CI}(s)\,, \tag{2.3}$$

where ΔCI is the change in CI for the model cell at time instant s. Values of 0.8 in PKJ and 0.2 in ventricular model cells are assigned for the DC, following the approximation given in [32].

2.2.2 Propagation of the excitation front

The excitation process in the Wei-Harumi heart model is based on cellular automaton (CA) method utilizing Huygens' Principle for wave front reconstruction [24]. The excitation process of the heart is simulated with discrete time step $\Delta t = 3$ ms. Activation of model cells is one of two types: "conductive" or "non-

conductive". The pacemaker model cells (SA, AV, BB, HIS, and PKJ) are referred to the non-conductive activation type, and their activation is obligatory whenever the firing time comes. The conductive activation in the ventricular model cells takes place due to propagation from exciting neighboring cells and is considered in three steps. At the first step, the extent of propagation around each exciting model cell is calculated. At a given time instant *s*, an ellipsoidal wavelet at the center of an exciting cell is calculated based on the local fiber direction, as illustrated in Fig. 2.3. This ellipsoid represents the extent within which the model cells will be activated during the time instant *s* + 1. If a cell location satisfies the inequality

$$\left(L_l / r_l\right)^2 + 2\left(L_t / r_t\right)^2 < 1 \ . \tag{2.4}$$

it is judged inside the ellipsoid. Here L_l and L_t are the distances along and across the fiber direction in the local coordinate system established at the exciting model cell (*i*, *j*, *k*),

$$r_l = V_l(t) \cdot \Delta t \tag{2.5}$$

is the long semiaxis of the wavelet along the principal (longitudinal) fiber direction, and

$$r_t = r_l \cdot r_\sigma \tag{2.6}$$

is one of other two short semiaxes along the transversal directions (Fig. 2.3). Here V_l is the longitudinal conduction velocity of the cell at time *t*, and r_σ is the ratio of transversal and longitudinal conductivities.

The model cells within the wavelet can be activated if they are excitable at that time. The second step is to judge the excitability of the model cells according to the principle of refractoriness by

$$t - \tau^{pre} > \mathrm{ARP}(t) \, , \tag{2.7}$$

where τ^{pre} is the starting time of the previous excitation of the model cell and ARP(t) is the absolute refractory period at time t. If the model cell is excitable, the third step is to assign a conduction velocity to it for propagation at the next time step. The above procedure is repeated for each time step until the preset total simulation time is reached.

2.2.3 Cardiac electric source

The propagation of excitation results in time dependent distributions of the transmembrane potential over the heart. Thus, to determine the cardiac source the relationship between the transmembrane potential distribution and the resulting source of the electromotive force should be determined.

Since the intracellular space is interconnected throughout the heart, and the junction resistance is very low, the intracellular space is considered as a continuous space with averaged parameters. At a global scale, since the remaining space outside the myocardial cells is also interconnected, it is regarded as another continuous space. Thus, two domains for the myocardial tissue are accounted for in the bidomain model [35] – the intracellular and extracellular domains. Both domains are coincident with the actual heart region and thus coincident with each other.

The deduction of the relationship between equivalent dipole source and distribution of transmembrane action potentials was first proposed in the study by Miller and Gesolowitz [35, 36]. Applying Ohm's Law to intracellular and extracellular spaces and considering anisotropic conductivity, the current dipole moment per unit volume (current density) $\vec{J}$ can be related to electric potential Φ as:

$$\vec{J}_{in} = -\mathbf{D}_{in}\vec{\nabla}\Phi_{in} \tag{2.8}$$

and

$$\vec{J}_{ex} = -\mathbf{D}_{ex}\vec{\nabla}\Phi_{ex}, \tag{2.9}$$

where **D** is the conductivity tensor, and *in* and *ex* are subscripts representing intracellular and extracellular spaces (domains), respectively [37]. Under a quasistatic assumption the conservation of current requires

$$\vec{\nabla} \cdot \vec{J}_{\text{in}} = -\vec{\nabla} \cdot \vec{J}_{\text{ex}}, \tag{2.10}$$

or

$$\vec{\nabla} \cdot (-\mathbf{D}_{\text{in}} \vec{\nabla} \Phi_{\text{in}}) = \vec{\nabla} \cdot (\mathbf{D}_{\text{ex}} \vec{\nabla} \Phi_{\text{ex}}). \tag{2.11}$$

Wei *et al.* [24] proposed a solution to simplify the problem with intracellular and extracellular anisotropies, assuming an anisotropic intracellular domain and an isotropic extracellular domain. Disregarding the anisotropy of conductivity in the extracellular domain, we obtain the following Poisson equation:

$$\nabla^2 \Phi_{\text{ex}} = \frac{1}{\sigma_{\text{ex}}} \vec{\nabla} \cdot (-\mathbf{D}_{\text{in}} \vec{\nabla} \Phi_{\text{in}}) = \frac{1}{\sigma_{\text{ex}}} \vec{\nabla} \cdot \vec{J}_{\text{in}}. \tag{2.12}$$

The intracellular conductivity tensor can be represented as

$$\mathbf{D}_{\text{in}} = \sigma_{\text{in}}^{t} \mathbf{Z}. \tag{2.13}$$

Here the matrix

$$\mathbf{Z} = \mathbf{E} + \left(\frac{\sigma_{\text{in}}^{l}}{\sigma_{\text{in}}^{t}} - 1 \right) \vec{u} \vec{u}^{T}, \tag{2.14}$$

contains anisotropy coefficients and is calculated for each model cell before simulation, σ_{in}^{l} and σ_{in}^{t} are the intracellular conductivities along the longitudal and transverse directions, $\mathbf{E}$ is the unity matrix, $\vec{u}$ is the unity vector along local fiber direction, and the symbol T represents a matrix transpose operation. Finally, the cell dipole source of model cell is determined as

$$\vec{J} = -\sigma_{\text{in}}^{t} \mathbf{Z} \vec{\nabla} \Phi_{\text{in}}. \tag{2.15}$$

The simplified assumption of anisotropic intracellular domain and an isotropic extracellular domain is reasoned by the measurement data from typical experimental studies. The conductivity ratios measured by Clerc [38] are approximately 9.0 for the intracellular space and 2.4 for the extracellular space. Those measured by Roberts *et al.* [39] are approximately 5.8 and 1.5, respectively. Evidently, as the extracellular

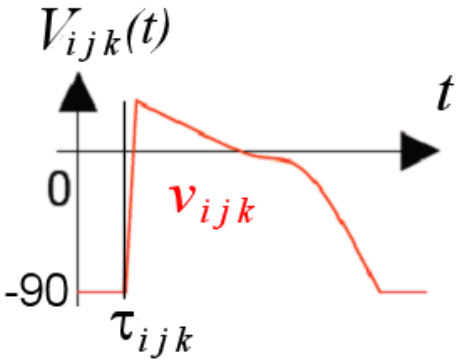

Figure 2.4: Action potential for a model cell (*i*, *j*, *k*).

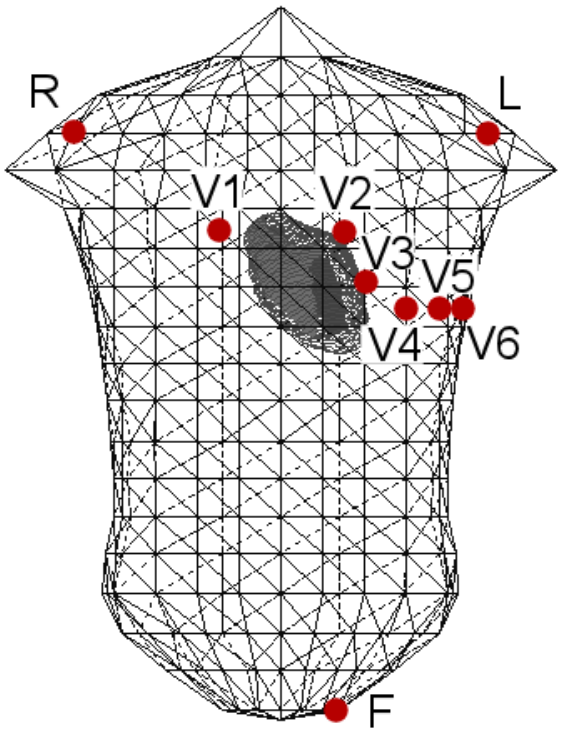

Figure 2.5: The heart-torso model. The circles indicate standard electrode positions for ECG recording (adopted from [21]).

conductivity ratio is significantly smaller than intracellular one the anisotropic effect of conductivity is predominantly caused by the intracellular anisotropy.

In the whole-heart model, each model cell with location denoted by three integers *i*, *j*, *k* has been assigned an action potential waveform $v_{ijk}(t)$ (see Fig. 2.4), which is a function of time τ^{pre} measured from the onset of previous excitation. When the excitation sequence of the whole heart is simulated, the transmembrane potentials are determined at each model cell at any time step. If time *t* is greater than or equal to τ_{ijk}^{pre},

it has passed $t-\tau_{ijk}^{pre}$ since the model cell (*i*, *j*, *k*) was activated, otherwise it is not ignited yet. Thus, AP is determined as:

$$V_{ijk}(t)=\begin{cases} v_{ijk}(t-\tau_{ijk}^{pre}), & t \geq \tau_{ijk}^{pre} \\ \text{resting potential (-90 mV)}, & t < \tau_{ijk}^{pre} \end{cases} . \tag{2.16}$$

2.2.4 Calculation of body surface ECG potentials

Simulation of surface ECG potentials is a typical volume conductor problem. In our study, the model is composed of current dipole sources located inside the myocardial tissue, homogeneous medium of torso, and surface boundary represented by 684 triangular meshes, as shown in Fig. 2.5.

To solve the Poisson's equation and calculate the body surface potentials on 344 nodal points on the torso surface model, we use the algorithm [21] developed on the base of the boundary element method. For a homogeneous torso model, the following equation for potentials can be established applying Green's theorem to the torso surface:

$$\Phi(\vec{r})=\frac{1}{4\pi\sigma}\int_{\Gamma}\vec{J}\cdot\vec{\nabla}\left(\frac{1}{r}\right)\mathrm{d}\Gamma+\frac{1}{4\pi}\int_{S}\Phi(\vec{r})\vec{\nabla}\left(\frac{1}{r}\right)\mathrm{dS}, \tag{2.17}$$

where Φ is the surface potential, Γ denotes the heart region, *S* represents the outer torso surface, σ is the conductivity, and *r* is a scale distance from $d\Gamma(\vec{r})$ to $dS(\vec{r})$. The first term of this equation is equal to the potential that would be yielded in an infinite homogeneous medium owing to the cardiac source. The second term reflects the boundary effect.

Since the conductivity is zero outside the torso, the normal component of the electric field must be zero on the body surface, which is the Neumann's boundary condition

$$\sigma\left.\frac{\partial\Phi}{\partial n}\right|_{S}=0. \tag{2.18}$$

For the solutions of potential theory, the boundary element method was used. The Poisson's equation given by (2.17) with homogeneous boundary condition of (2.18) is modified into the Laplace equation with inhomogeneous boundary condition. For this purpose an intermediate variable ψ is introduced

$$\psi(r) = \Phi(r) - \Phi^{\infty}(r), \tag{2.19}$$

where $\Phi(r)$ and $\Phi^{\infty}(r)$ are the potentials at point *r* in the presence of current source *J* but in bounded and infinite media, respectively. Then $\psi(r)$ satisfies the Laplace equation in the torso and the boundary condition on the torso surface

$$m(r) = \left.\frac{\partial \psi(r)}{\partial n}\right|_S = \left.\frac{\partial \Phi(r)}{\partial n}\right|_S - \left.\frac{\partial \Phi^{\infty}(r)}{\partial n}\right|_S = -\left. q^{\infty}(r)\right|_S . \tag{2.20}$$

Now ψ instead of Φ is calculated by means of the boundary element method and the method of weighted residuals on the base of the following equation

$$\int_{\Gamma} \left(\nabla^2 \psi\right) w \mathrm{d}\Gamma + \int_{S_1} \left(\psi - \overline{\psi}\right) \frac{\partial w}{\partial n} \mathrm{d}S = -\int_{S_2} \left(m - \overline{m}\right) w \mathrm{d}S . \tag{2.21}$$

Here S_1 and S_2 are the parts of the torso surface, where the values of ψ and its normal derivative *m* are equal to $\overline{\psi}$ and $\overline{m}$, respectively. The weighting function *w* has two parameters $\vec{r}$ and $\vec{r}\,'$ and the integration is performed with respect to $\vec{r}\,'$. In the case under consideration, S_2 coincides with the whole torso surface and *m* is given in (2.20). Choosing the Green function

$$G = \frac{1}{4\pi \left|\vec{r} - \vec{r}\,'\right|} \tag{2.22}$$

as the weighting function *w*, we get

$$\int_S \psi \frac{\partial G}{\partial n} \mathrm{d}S = -\int_S q^{\infty} G \mathrm{d}S . \tag{2.23}$$

Discretization of the integral equation (2.23) leads to the system of linear equations

$$\sum_{j=1}^{N} a_{ij}\psi_j = -\sum_{j=1}^{N} b_{ij} q_j^{\infty} \qquad i = 1, 2, ..., N, \tag{2.24}$$

where a_{ij} and b_{ij} are coefficients depending on the torso geometry and N is the number of nodes on the torso surface. To provide a unique solution for (2.24) an additional condition

$$\sum_{i=1}^{N} c_i \Phi_i = \sum_{i=1}^{N} c_i \left(\psi_i + \Phi_i^{\infty}\right) = 0 \tag{2.25}$$

is further imposed, where coefficients c_i are proportional to the area of an elemental triangle which has node i as an apex. This condition is used to ensure that the surface potential integral equals zero. Equations (2.24) and (2.25) can be written in a matrix notation form as

$$\mathbf{A}\vec{\psi} = -\mathbf{B}\vec{q}^{\infty} - \vec{C}\ , \tag{2.26}$$

where **A** and **B** are the matrices with N+1 rows and N columns composed of a_{ij} and b_{ij} in equation (2.24). Their elements in the (N+1)-th row are c_i-s in (2.25) and zeros, respectively. Vectors $\vec{\psi}$ and $\vec{q}^{\infty}$ are the N-dimensional with elements ψ_i and q_i^{∞}, respectively. $\vec{C}$ is the (N+1)-dimensional vector whose elements are all zero except the (N+1)-th one which is

$$c_{N+1} = \sum_{i}^{N} c_i \Phi_i^{\infty}\ . \tag{2.27}$$

The final solution for surface potentials Φ_i in the nodes on the torso surface is expressed in vector form as:

$$\vec{\Phi} = \vec{\Phi}^{\infty} - \mathbf{M}\vec{q}^{\infty} - \vec{p}^{\infty}, \tag{2.28}$$

where

$$\mathbf{M} = (\mathbf{A}^{\mathrm{T}}\mathbf{A})^{-1}\mathbf{A}^{\mathrm{T}}\mathbf{B} \tag{2.29}$$

and

$$\vec{p}^{\,\infty} = (\mathbf{A}^{\mathrm{T}}\mathbf{A})^{-1}\mathbf{A}^{\mathrm{T}}\vec{C}\,. \tag{2.30}$$

The torso model used in this study does not include conductivity inhomogeneity. The effect of the torso inhomogeneity on the body surface potentials has been widely investigated, resulting in the suggestions that the latter gives little quantitative changes to the ECG and body surface potential maps [40]. Also, Shahidi and Savad [41] using a torso model constructed from 1-mm computer tomography image cross-sections, concluded that inclusion of the conductivity inhomogeneity changed the minimum and maximum values of the body surface potentials but did not alter the patterns of potential distribution.

Using the calculated body surface potentials, the standard 12-lead ECG can be easily obtained. Many previously reported results demonstrated that the simulated ECGs were reasonable as compared to clinical ECGs [42].

2.3 Computer simulation of atypical Brugada syndrome

2.3.1 Brugada syndrome

The Brugada Syndrome (BS) was described first in 1992 [43]. It is characterized by the presence of ST-segment elevation in the right precordial leads (V_1, V_2, and V3) in patients with structurally normal heart. Sudden death and syncope are the most important clinical manifestations through the occurrence of ventricular fibrillation (VF) or fast ventricular tachycardia with polymorphic characteristics.

Recently, an atypical (variant) type of the BS has been reported in some patients [44–52]. Their ECG showed J-wave and ST-segment elevation not only in the right precordial leads, but in the inferior (II, III, and aVF) or high lateral leads (I, V_5, and V_6) as well, while other characteristics were quite similar.

In some of these cases, spontaneous VF was observed [45–48, 50]. It is supposed in the works [48–50, 52] that typical and atypical BS forms could differ in the location of electrophysiological substrate. Furthermore, Potet *et al.* provided genetic

demonstration that Brugada ECG anomalies related to a unique SCN5A (sodium channel, voltage-gated, type V, alpha subunit) mutation can be observed either in the inferior or in the right precordial leads [53]. Thus, the purpose of this study was to investigate the hypothesis that the atypical BS can distinguish from the typical form in anatomical location of abnormal cells, which has not been clarified yet.

So far, significant advances have been made to underpin the clinical, genetic, cellular, ionic, and molecular mechanisms of this disease (see, for example, [53–55]). Obviously, still there are many unanswered questions about original mechanism of BS. Investigation on human ventricular myocardium with BS is still very limited due to lack of available experimental data. Therefore, alternative methods such as computer simulation are of great importance and the usable way to study BS pathophysiology.

Many biophysically detailed cardiac models have been developed in order to better understand the physiological and pathological functions of the heart [56–59]. Such models incorporate both single cell and three-dimensional (3D) tissue models that simulate important features of cardiac electrophysiology, mechanics and metabolism (see, for example, [56–59] and references therein). Few of these models, however, have been adapted to simulate BS heart.

In this Section, we extend the application of Wei-Harumi model to the simulation of the atypical BS and VF closely associated with the disease [29]. Such investigation of the electrophysiological manifestations of the disease including its atypical forms is useful for in-depth understanding of the pathological mechanism of the syndrome and probably will improve the recognition of the disease in general.

2.3.2 Simulation method

The simulations in this chapter were performed using software based on whole-heart Wei-Harumi model. The standard 12-lead ECG was calculated based on standard electrode positions. As in the simulations the ECG manifestations change in accordance with the volume and orientation of Brugada model cells, we adjusted the electrophysiological parameters, such as AP distribution and conduction velocity (CV), localization, and number of BS model cells to obtain BS (for typical and for atypical types) ECG waveforms similar to clinical data. In this section, surface ECGs were simulated by the heart model under the following cases:

Table 2.2: Parameters of the ventricular epicardial cell characteristics: action potential duration (APD), absolute refractory period (ARP), functional refractory period (FRP), and conduction velocity (CV).

	APD (ms)	ARP (ms)	FRP (ms)	CV (m/s)
Normal model cell	255	200	295	0.50
BS model cell	80	120	327	0.20

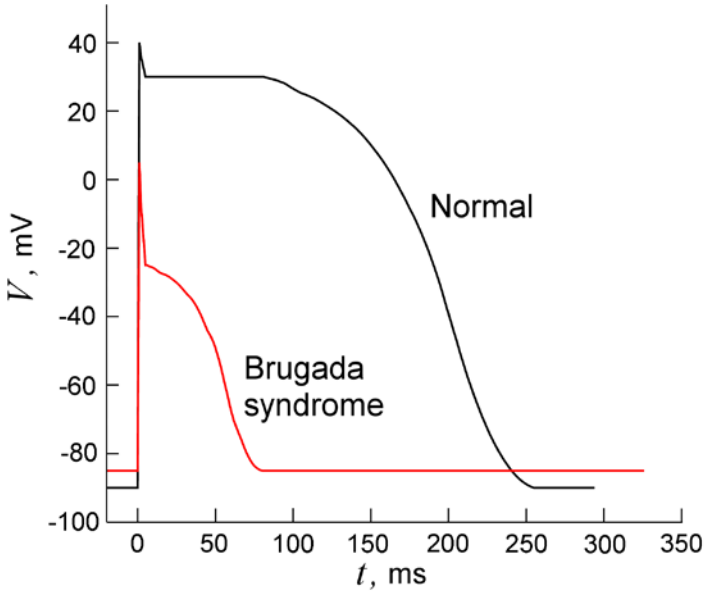

Figure 2.6: Action potentials for normal and Brugada epicardial model cells.

a. Normal sinus rhythm without abnormal cells (normal heart);

b. Normal sinus rhythm in the heart with typical BS in the RV outflow tract (RVOT);

c. Normal sinus rhythm in the heart with atypical BS in the RV apex (RVA);

d. Normal sinus rhythm in the heart with atypical BS in the LV lateral wall;

e. VF induced applying extra stimuli in the conditions of the case **b**;

f. VF induced applying extra stimuli in the conditions of the case **c**;

g: VF induced applying extra stimuli in the conditions of the case **d**;

We set up parameters of action potentials for normal and Brugada epicardial model cells as shown in Table 2.2 to fit the shapes to experimental data [54]. The calculated APs for normal and Brugada epicardial model cells are shown in Fig. 2.6. According to experimental report of Antzelevitch [54], the reduction of sodium current in the BS epicardial cell in comparison to the normal cell, results in decreased

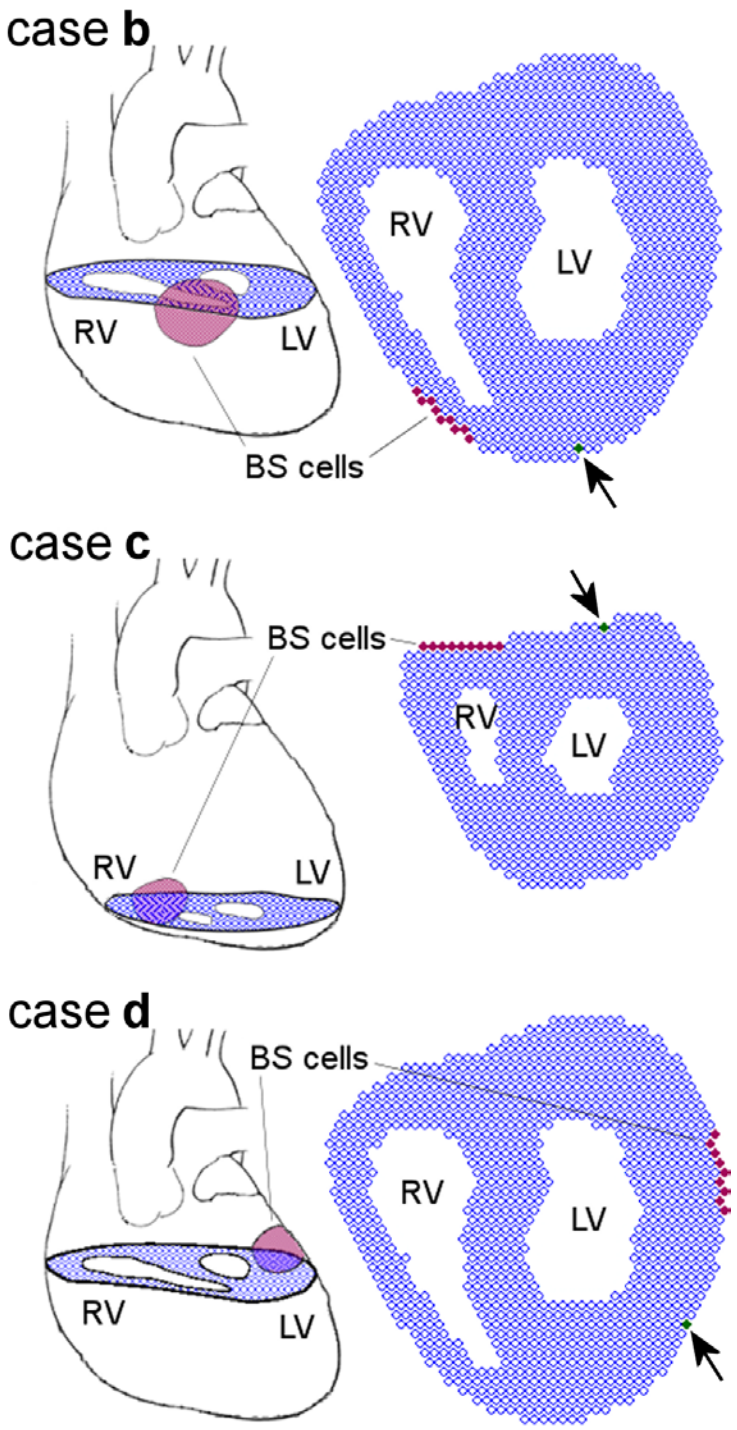

Figure 2.7: Schematic illustrations of anterior heart view with locations of Brugada model cells (left column) and horizontal cross-sections of the heart model (right column): in the right ventricular outflow tract (case **b**), in the right ventricular apex (case **c**), and in the left ventricular lateral wall (case **d**). The arrows indicate the positions of extra stimulation for cases **e** – **g**, respectively.

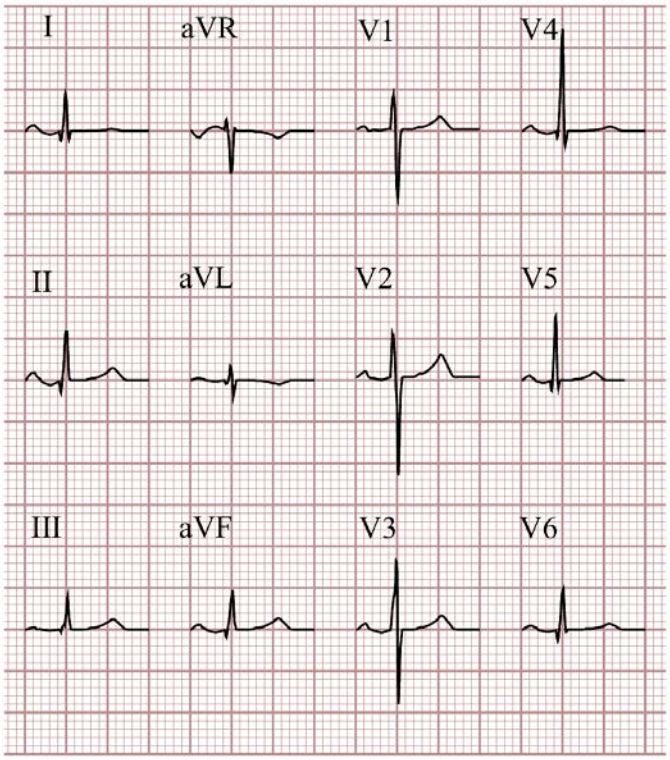

Figure 2.8: Simulated 12-lead ECG waveforms for the case **a**.

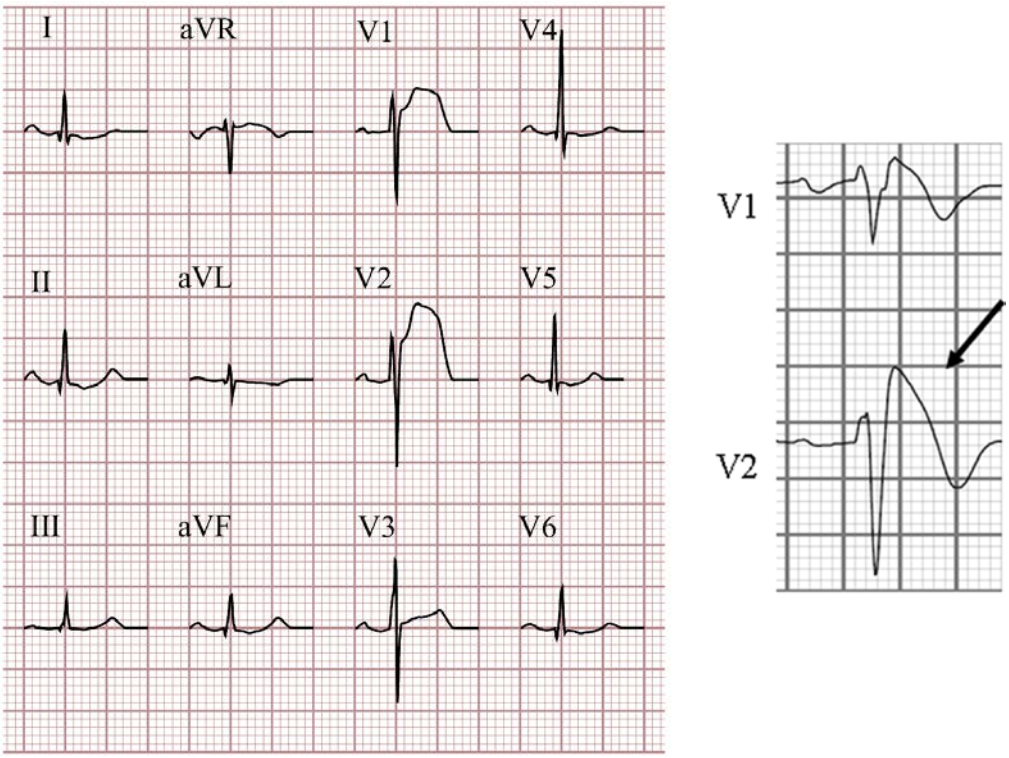

Figure 2.9: Simulated 12-lead ECG waveforms (left) and clinical data [61] (right) for typical Brugada syndrome form (case **b**).

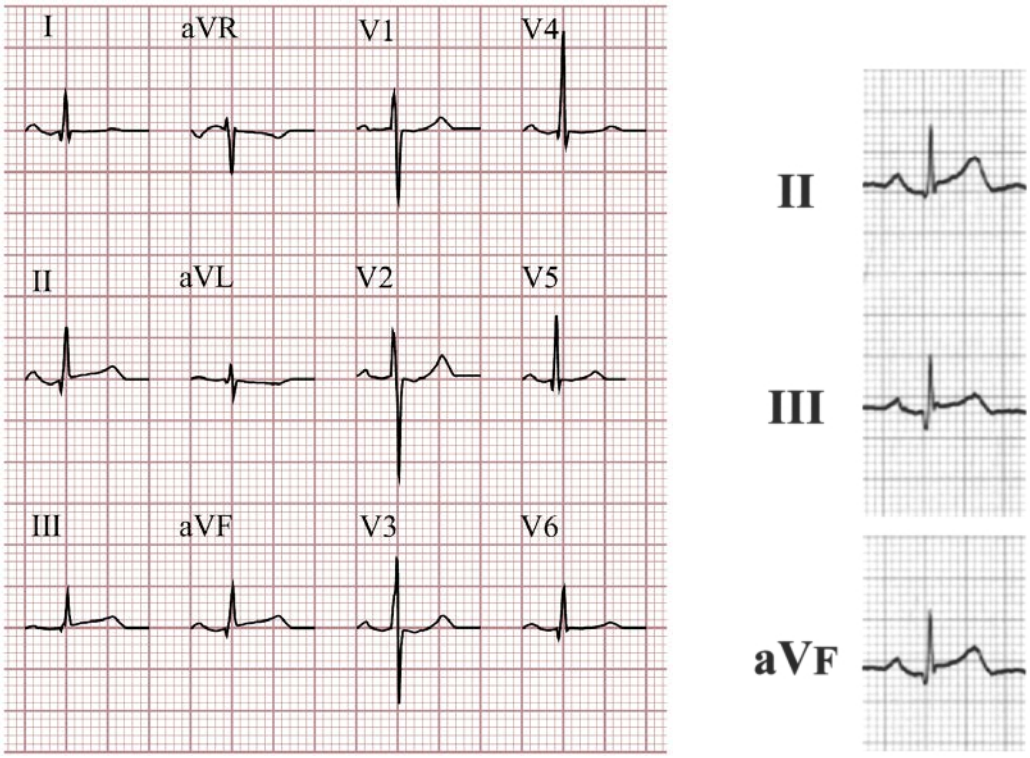

Figure 2.10: Simulated 12-lead ECG waveforms (left) and clinical data [44] (right) for atypical inferior Brugada syndrome form (case **c**).

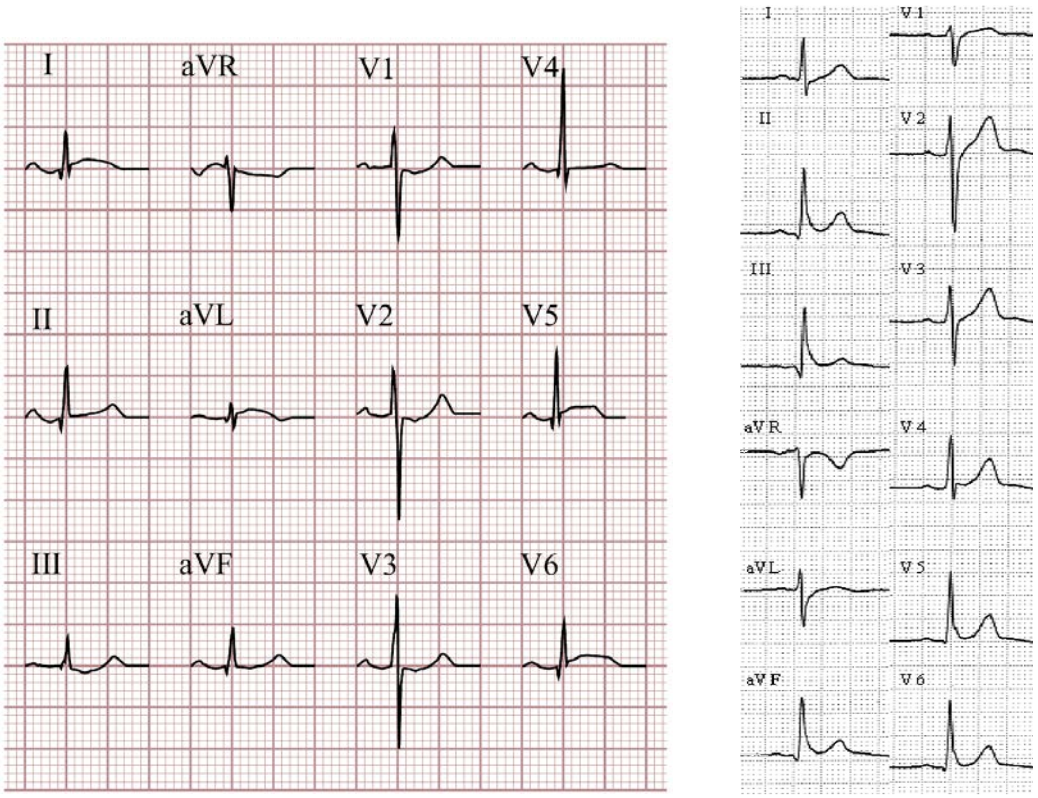

Figure 2.11: Simulated 12-lead ECG waveforms (left) and clinical data [45] (right) for atypical lateral Brugada syndrome form (case **d**).

maximum AP peak value. On the other hand, the increased transient outward potassium current perturbs the balance between the outward and inward currents during the phase 2 AP, and accentuates the spike and dome morphology of the AP, resulting in a delay in the development of the dome and the disappearance of the AP notch. A loss of the AP dome at the epicardium but not at the endocardium creates a transmural voltage gradient that leads to the accentuation of J wave causing an apparent ST segment elevation in the right precordial ECG leads, which is one of the principal signs of the BS.

We defined special regions of BS model cells lying across seven ventricular horizontal layers of the in the RVOT, RVA, and LV lateral wall for the simulation cases **b**, **c**, and **d**, respectively (see Fig. 2.7, left column). Since the BS ECG manifestations and the VF inducibility augment with increasing volume of BS cells, we fitted the number and location of the model cells in such a way as to correspond to clinical findings. In simulation cases **e**, **f**, and **g** five trains of electrical stimuli were applied to the non BS ventricular model cell located 2 cm from the BS area with a delay of 300 ms after the first sinus pacing beat with a cycle length of 160 ms (Fig. 2.7, right column). Slow conduction in these simulations was defined as 0.2 m/s, in regarding to the normal ventricular setting of 0.5 m/s [60].

2.3.3 Results

First we simulated 12-lead ECG of normal sinus rhythm without abnormal cells (normal heart, case **a**). The obtained normal ECG is shown in Figure 2.8. Next simulation was performed to reproduce normal sinus rhythm in the heart but with BS model cells in the RVOT (case **b**). Figure 2.9 successfully reproduces the characteristic configurations of 12-lead ECG for typical BS with ST-segment elevation in the right precordial ECG leads (V1 – V3) similar to demonstrated in [43].

Simulated ECG waveforms corresponding to case **c** are demonstrated in Fig. 2.10. It is seen that the ECG ST-segments are elevated in the inferior leads (II, III, and aVF), and accompanied by the so-called J waves, which corresponds to clinical case reports [44].

We repeated the same procedure with Brugada AP applied in LV lateral wall (case **d**) and observed (see Fig. 2.11) ST segment elevation and J waves in high lateral leads (I, V5, and V6) in agreement with clinical data [45–51].

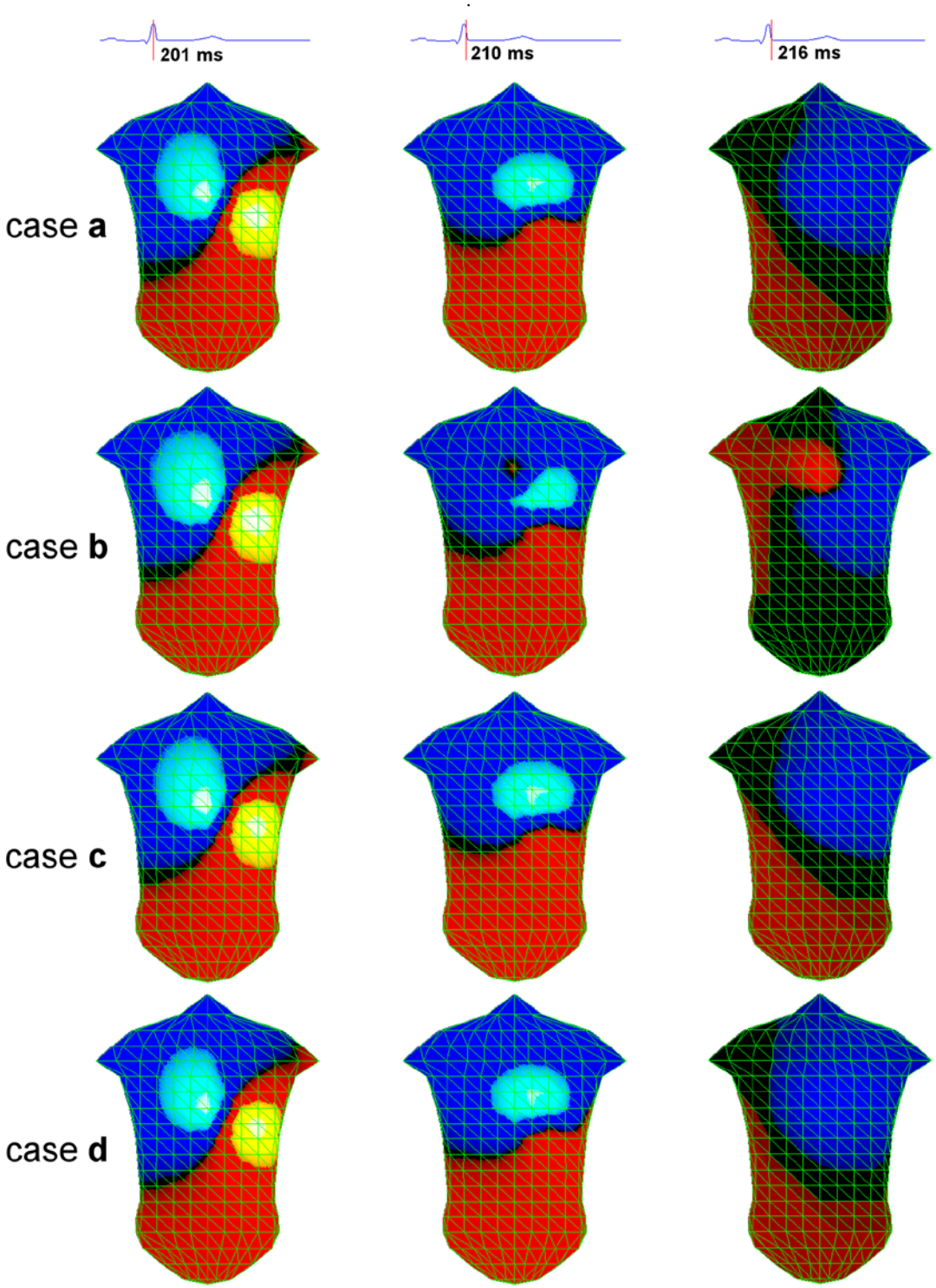

Figure 2.12: Simulated body surface potential distributions for cases **a** – **d** at three time snapshots. The vertical lines on the lead II ECG waveforms (on the top) correspond to 201 ms, 210 ms and 216 ms.

Body surface potential distributions can reflect the abnormalities in repolarization and clarify the mechanism of ECG changes. In the case of typical Brugada syndrome the positive potential region appears in the high median precordial area in the beginning of J wave, while in the normal subject there is no such positive potential region in this location. Similar changes were expected in corresponding areas in the cases of atypical BS. In this work, we calculated for first time body surface potential distributions for atypical forms of the disease.

Figure 2.12 shows the calculated body surface potential distributions corresponding to cases **a** – **d** at three different time snapshots, chosen to demonstrate the most remarkable distinctions. It is seen that the potential distribution in the middle of R-wave (201 ms) does not show significant difference between normal and BS subjects. On the other hand, at the end of the R wave (210 ms) one can observe significantly smaller negative potential area (bright spot, blue in color version) for typical BS form (case **b**) in comparison with normal condition (case **a**). However, in the cases of atypical BS forms (cases **c** and **d**) at the same moment this negative potential area is not so distinguishable.

At the beginning of the J wave (216 ms) a positive potential region (red color) appears in the median precordial lead area of typical BS subject (case **b**), that doesn't exist for normal subject (**a**) and atypical BS forms (cases **c** and **d**). The negative potential region (dark blue color on left anterior side) in the cases of atypical BS is slightly wider in comparison with normal case. By our opinion, this difference could be explained by electrophysiological alterations associated with anatomical locations of BS sources. Calculated body surface potential distributions for the typical BS case correspond to the clinical findings [62], while we do not have any comparable clinical data for the atypical cases.

Next simulation was performed to reproduce such important electrocardiographic feature of BS leading to sudden cardiac death as ventricular tachyarrhythmia in order to elucidate the pathophysiological basis of BS. To examine whether VF could be induced, we applied additional electrical stimuli to the normal ventricular cells outside of the BS area. Arrows on Fig. 2.7 indicate the positions of the extra stimulations. For presentation in this section, we used conditions (number and delay of electrical stimuli, position of extra stimuli) similar to ones described in the works on simulation of arrhythmias and peri-infarctional ventricular fibrillation [63] and simulation of idiopathic ventricular fibrillation [60]. On the other hand, in the simulation of normal

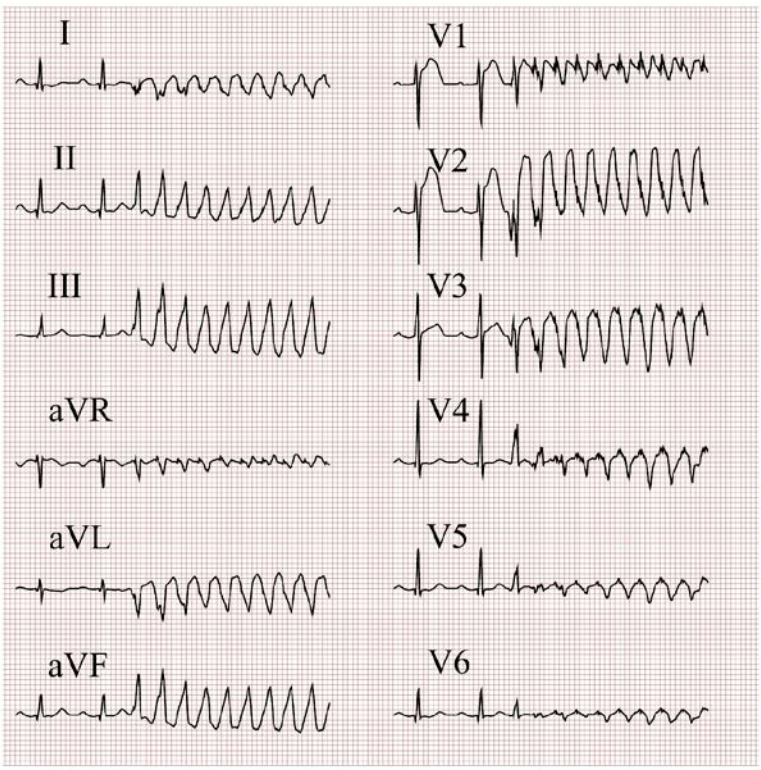

Figure 2.13: Simulated 12-lead ECG waveforms of ventricular fibrillation for typical Brugada syndrome form (case **e**).

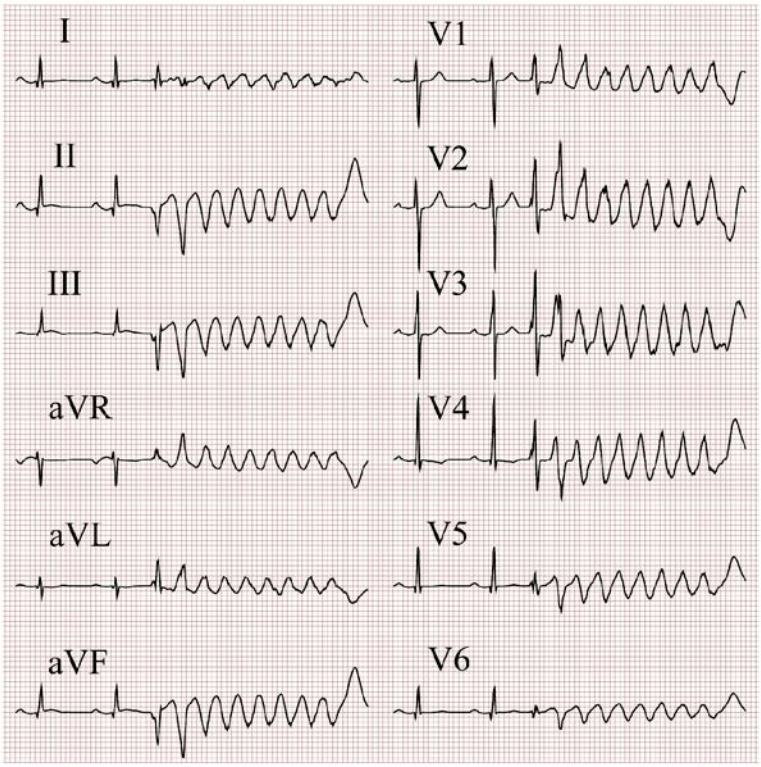

Figure 2.14: Simulated 12-lead ECG waveforms of ventricular fibrillation for atypical inferior Brugada syndrome form (case **g**).

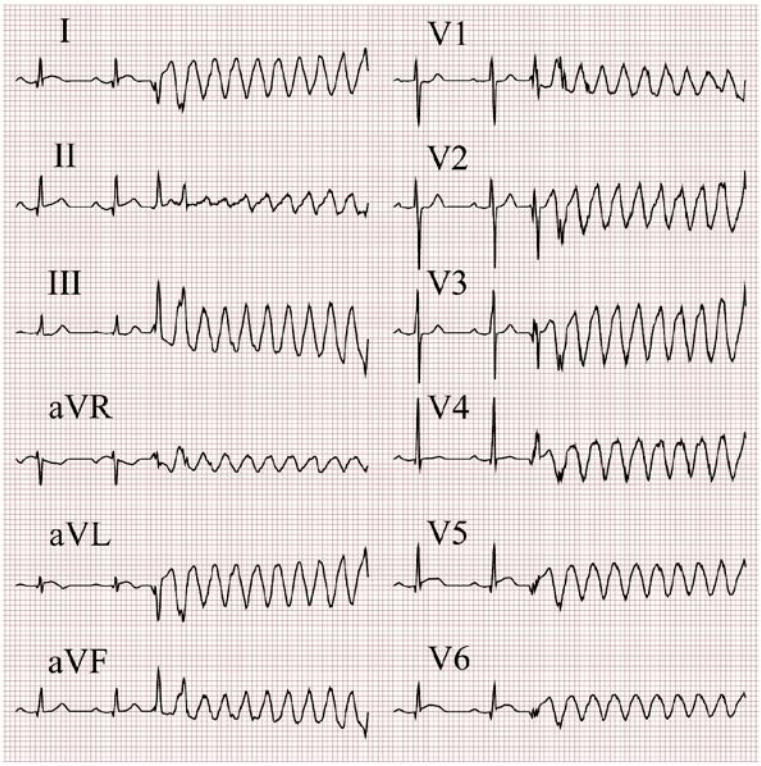

Figure 2.15: Simulated 12-lead ECG waveforms of ventricular fibrillation for atypical lateral Brugada syndrome form (case **f**).

heart application of the same extra stimuli did not induce VF. In case of the BS the epicardial AP is shorter than the endocardial one, which causes intrinsic transmural heterogeneity of ventricular electrical activity producing dispersion of ventricular repolarization and generates the reentry leading to fibrillation.

Figures 2.13, 2.14, and 2.15 show resulting simulated ECG waveforms of VF with typical location of pathological Brugada model cells, atypical lateral, and atypical inferior locations, respectively, upon application of five trains of stimulation to the model heart. The obtained ECG waveforms of VF, which are characteristic feature of the Brugada disease, correlate well with clinical observations [44–48, 50].

2.3.4 Discussion and conclusion

Since the discovery of Brugada syndrome, many research papers have been dedicated to the exploration of the mechanism of BS based on modeling and simulation methods. Compared with animal and human experimental approaches, an advantage of the 3D whole-heart model is that it can set up various pathological model parameters easily and optionally; hence, it is convenient to study a variety of

cardiac conditions. Computer simulations utilizing the model are effective alternative tool for investigation of the causes and mechanisms of the origin of different electrocardiological diseases and can be effectively applied for education and research purposes.

Previous simulation studies were dedicated only to the typical form of BS, whereas the atypical form of BS has not been investigated so far. Recently, few cases of BS with anomalous localizations of ECG manifestations were reported in literature [44–52]. Potet *et al*. have shown a G752R mutation on SNC5A that produced ST segment elevation and prominent J wave in leads II, III, and aVF [53]. Van Den Berg *et al*. reported about the case of a patient with Brugada signs in lateral leads [51].

In this section, we analyzed the cases of BS atypical localizations carrying out computer experiments utilizing the 3D whole-heart model. Setting up model cells with the AP typical for Brugada disease (Fig. 2.6), in different localizations (Fig. 2.7), we observed that calculated ECG waveforms (Figs. 2.9 – 2.11) correspond to clinical data [44–52]. Accentuation of the RV notch under pathophysiological conditions (increasing of transient outward current) leads to increasing of transmural voltage gradient and thus to emphasis of the J wave [54]. This would be give rise to saddle-back ECG morphology. Further accentuation of the notch is accompanied by a prolongation of the epicardial AP leading to the development of a coved-type ST segment elevation and inversion of the T wave (observed by Kurita *et al.* [55]).The loss of the AP dome in epicardium but not in endocardium produces a marked transmural dispersion of repolarization responsible for reentrant arrhythmia. In this work, we used shortened AP corresponding to the most severe case of BS because our aim was to investigate the inducibility of VF. The case of spike-and-dome AP morphology considered by Kurita *et al.* with longer APD may be a good subject for future studies.

In our simulations, we used conduction velocity of 0.2 m/s for BS model cells instead of 0.50 m/s for normal condition (Table 2.1). This setting is supported by several studies. In Wang *et al.* it is described that in the case of BS, biophysical ion disbalance is augmentation of slower forms of sodium channel inactivation, which may lead to an activity-dependent loss of sodium channel functionality, resulting in reduction of myocardial sodium current density. The latter will increase time of the cardiac action potential and slow conduction velocity [64]. In addition, Nagase *et al.* demonstrated in their study that there is a close relation between prolongation of

repolarization in the epicardium and Brugada ECG, and longer repolarization in the epicardium (type 1 Brugada ECG) could be explained by reduced conduction velocity at the RVOT [56].

Next, applying additional stimuli, we successfully provoked VF in all cases (Figs. 2.13 – 2.15). Similar cases with induced and spontaneous VF observed in patients with atypical Brugada ECG waveforms were reported in literature [44–48, 50].

As supposed in literature and demonstrated in previous section, Brugada-type ECG waveforms can be observed in different precordial leads. It is seen that electrophysiological basis of the disease could be originated not only from RVOT, but from RVA and LV lateral regions as well. In contrast with typical BS form, ST segment elevation was smaller when BS model cells are located at RV apex and LV lateral wall that can be attributed by our opinion to the regional repolarization pathological effects. Because the transient outward current is better represented in the right ventricular that in the left ventricular myocardium, the transmural (epi – endo) voltage gradient is increased in the right precordial leads where the typical ECG repolarization abnormalities usually take place [54, 55].

However, in contrast with typical BS form, distributions of body surface potentials for the inferior and lateral atypical BS forms did not demonstrate significant difference comparing with normal case (Fig. 2.12), that can be attributed, by our opinion, to the regional repolarization abnormality effects.

We speculate, that the presence of ST segment elevation also in the inferior or lateral leads indicates that the loss of epicardial AP dome could take place in the right precordial, inferior, and lateral regions with the possibility of more extensive electrophysiological alteration of ECG pattern.

The results of this chapter emphasize the clinical and anatomical heterogeneity of BS, possibly influenced by multiple factors including, for example, a hormonal and genetic substrate. Further clinical and experimental investigations are necessary to clarify this hypothesis.

2.3.5 Limitations of the model

In current model, parameters of AP were manually inputted and did not take into account ion current densities, which create AP in cardiac myocytes. Moreover, the

model did not include properties of midmyocardial cells, which play very important role in transmural heterogeneity in heart AP distribution. In our next study, we developed modified whole-heart model combining ion-channel model of human ventricular myocytes with heart model [30].

2.4 Chapter summary

In the first part of this chapter, we gave detailed description of the whole-heart Wei-Harumi model including rules of excitation propagation and calculations of cardiac electric source and body surface ECG potentials.

Next, we presented a computer simulation study of the atypical BS using the heart model. The obtained simulated ECG waveforms for typical, inferior, and lateral BS forms are in a good agreement with clinical data. We demonstrated that AP and ECG changes in case of atypical BS lead to the same inducibility of VF and increased risk of sudden cardiac death as in the typical BS form. The obtained results confirm similar electrophysiological basis for both typical and atypical BS forms. We conclude that BS can be observed not only in the right precordial leads, but in the inferior and lateral leads as well.

Chapter 3
Study of T wave morphology with combined biventricular and ion-channel models

3.1 Overview of ion-channel models of human ventricular myocytes

The membrane of cardiac myocytes contains large number of ionic channels and pumps, which provide passage of different ions through the membrane, and thus the action potential is created. To perform simulation studies of reentrant arrhythmias in human ventricles we need a mathematical model that on the one hand reproduces detailed properties of single human ventricular cells, such as the major ionic currents, APD, and important properties of wave propagation in human ventricular tissue, such as CV restitution. On the other hand, it should be computationally efficient enough to be applied in the large-scale spatial simulations needed to study reentrant arrhythmias.

In recent years, more and more data on human ionic currents have been collected from human cardiomyocytes. Consequently, in recent years, several models for human ventricular cells have been developed.

In 1998 Priebe and Beuckelmann (PB) published the first model for human ventricular myocytes [66]. Their model was largely based on the Luo–Rudy phase 2 model (LR) for guinea pig ventricular cells [57] where formulations for the major ionic currents were adjusted to the insufficient data available for human ventricular cells at that time. In addition, for the computer power available at that time, the model was too complex for large-scale spatial simulations of reentrant arrhythmias.

This limitation was overcome in a reduced version of the PB model (redPB) proposed by Bernus *et al.* [67], where the number of variables was reduced from 15 to 6 by reformulating some currents and fixating intracellular ionic concentrations.

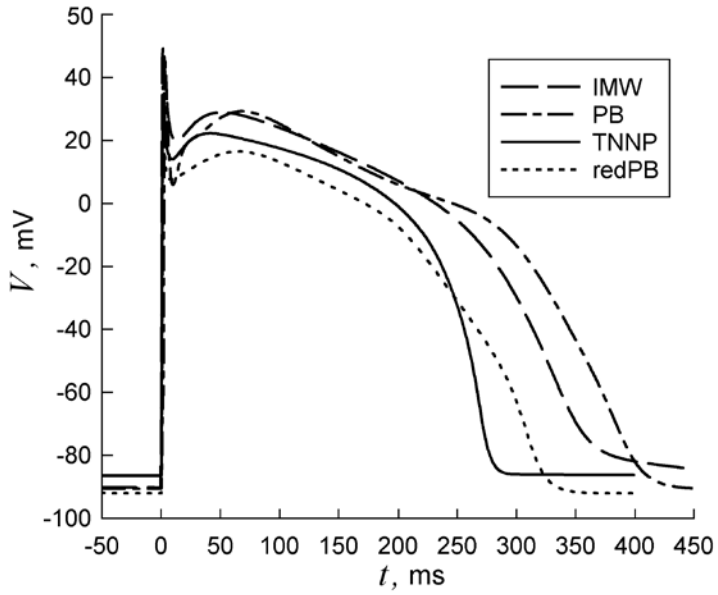

Figure 3.1: Action potentials for different ion-channel models of human ventricular myocytes.

In 2004, a new model for human ventricular myocytes by ten Tusscher, Noble, Noble, and Panfilov appeared (TNNP) [68]. This model uses recent formulations for all major ionic currents based on experimental data, largely from human ventricular cell experiments but also from ion-channel expression experiments. TNNP model was constructed to create a compromise between a considerable level of physiological detail and computational efficiency.

Another model for human ventricular myocytes by Iyer, Mazhari, and Winslow *et al.* (IMW) [69] was published in 2004. As compared to the TNNP model, the IMW model is more strongly based on expression data on human cardiac ionic channels than on data on human ventricular cells. In addition, formulations for most major ionic current are of the Markov chain rather than Hodgkin–Huxley type, causing the model to consist of a larger number of variables: 67 in the IMW model compared to 16 in the TNNP model. The large number of variables and the small time step required for integration make the IMW model computationally extremely demanding, with simulations running about 900 times slower than either the PB or TNNP model. Comparison of AP for these models is demonstrated on Fig. 3.1.

In 2006 ten Tusscher and Panfilov developed a version of human ventricular cell model (TP) [70], which is based on newly available experimental measurements of human APD restitution and includes a more extensive description of intracellular

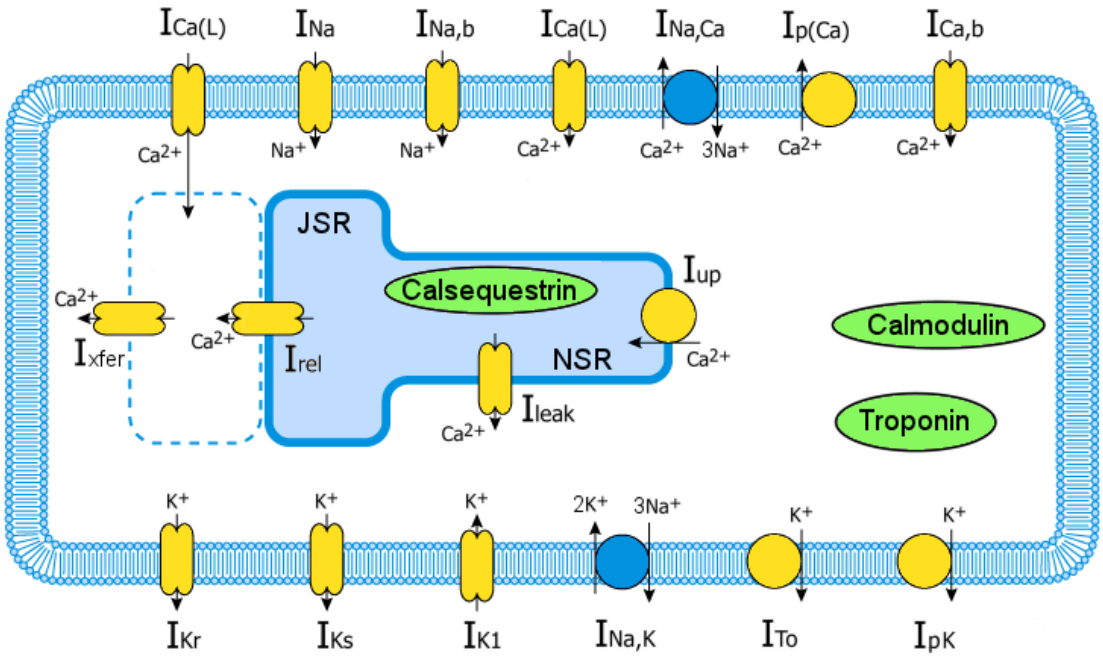

Figure 3.2: A schematic diagram for Ten Tusscher *et al*. 2006 mathematical model of human ventricular myocyte (adopted from [71]).

calcium dynamics (the latter is very important for arrhythmia initiation). In this chapter, we modified the recent TP model and applied it to study T wave morphology.

3.2 Ten Tusscher and Panfilov model

The model [70] fits experimentally measured APD restitution properties of human myocardium and agree better with experimental data than those of previously developed ionic models. The model is able to reproduce the different AP shapes and duration corresponding to the endo-, epi-, and midmyocardial regions of the ventricles. A schematic diagram describing the ion movement across the cell surface membrane and the sarcoplasmic reticulum for Ten Tusscher *et al*. 2006 mathematical model of human ventricular myocyte is shown on Fig. 3.2.

The cell membrane is modeled as a capacitor connected in parallel with variable resistances and batteries representing the different ionic currents and pumps. The electrophysiological behavior of a single cell is described using Hodgkin-Huxley-type formalism [72]:

$$\frac{\partial V}{\partial t} = -\frac{I_{ion} + I_{stim}}{C_m}, \tag{3.1}$$

where V is voltage, I_{ion} is the sum of all transmembrane ionic currents, I_{stim} is the externally applied stimulus current, and C_m is cell capacitance per unit surface area.

Similarly, ignoring the discrete character of microscopic cardiac cell structure, a 2D sheet of cardiac cells can be modeled as a continuous system with the following partial differential equation:

$$\frac{\partial V}{\partial t} = -\frac{I_{ion} + I_{stim}}{C_m} + \frac{1}{\rho_x \eta_x C_m}\frac{\partial^2 V}{\partial x^2} + \frac{1}{\rho_y \eta_y C_m}\frac{\partial^2 V}{\partial y^2}, \tag{3.2}$$

where ρ_x and ρ_y are the cellular resistivity in the x and y directions, η_x and η_y are the surface-to-volume ratio in the x and y directions, and I_{ion} is given by the following equation:

$$I_{ion} = I_{Na} + I_{K1} + I_{to} + I_{Kr} + I_{Ks} + I_{CaL} + I_{NaCa} + I_{NaK} + I_{pCa} + I_{pK} + I_{bCa} + I_{bNa}, \tag{3.3}$$

where I_{Na} is Na^+ current, I_{K1} is inward rectifier K^+ current, I_{to} is transient outward current, I_{Kr} is rapid delayed rectifier current, I_{Ks} is slow delayed rectifier current, I_{CaL} is L-type Ca^{2+} current, I_{NaCa} is Na^+/Ca^{2+} exchanger current, I_{NaK} is Na^+/K^+ pump current, I_{pCa} and I_{pK} are plateau Ca^{2+} and K^+ currents, and I_{bCa} and I_{bNa} are background Ca^{2+} and Na^+ currents. The pertinent equations describing membrane ionic current formulations of TP mathematical model are presented in the Appendix. Physical units used in the model are as follows: time t in milliseconds, voltage V in millivolts, current densities I_X in picoamperes per picofarad, conductances G_X in nanosiemens per picofarad (except for G_{CaL}), and intracellular and extracellular ionic concentrations (X_{in}, X_{ex}) in millimoles per liter. However, the independent and dependent variables in the some model equations are used in dimensionless form [73].

All parameters and physical values used in the model description are given in Table 3.1. Here I_{pCa} is sarcolemmal Ca^{2+} pump current, I_{rel} is calcium-induced calcium release current, I_{up} is sarcoplasmic reticulum (SR) Ca^{2+} pump current, I_{leak} is SR Ca^{2+} leak current, I_{xfer} is diffusive Ca^{2+} current between dyadic subspace and bulk cytoplasm, O, R, I, and RI are open conducting state, resting closed state, inactivated closed state, and resting inactivated closed state of I_{rel}, respectively.

Table 3.1: Parameters for ten Tusscher and Panfilov model [70].

Parameter	Definition	Value
R	Gas constant	8.3143 $J \cdot K^{-1} \cdot mmol^{-1}$
T	Temperature	310 K
F	Faraday constant	96.4867 C/mmol
C_m	Cell capacitance per unit surface area	2.0 $\mu F/cm^2$
η_x, η_y	Surface to volume ratio	0.2 μm^{-1}
ρ	Cellular resistivity	162 $\Omega \cdot cm$
Γ_c	Cytoplasmic volume	16.404 μm^3
Γ_{sr}	Sarcoplasmic reticulum volume	1.094 μm^3
Γ_{ss}	Subspace volume	0.05468 μm^3
K_{ex}	Extracellular K^+ concentration	5.4 mM
K_{in}	Extracellular K^+ concentration	138.3 mM
Na_{ex}	Extracellular Na^+ concentration	140.0 mM
Na_{in}	Extracellular Na^+ concentration	7.67 mM
Ca_{ex}	Extracellular Ca^{2+} concentration	2.0 mM
Ca_{in}	Extracellular Ca^{2+} concentration	7.0×10^{-5} mM
G_{Na}	Maximal I_{Na} conductance	14.838 nS/pF
G_{K1}	Maximal I_{K1} conductance	5.405 nS/pF
G_{to}^{epi}, G_{to}^{mid}	Maximal epi- and midmyocardial I_{to} conductance	0.294 nS/pF
G_{to}^{endo}	Maximal endocardial I_{to} conductance	0.073 nS/pF
G_{Kr}	Maximal I_{Kr} conductance	0.153 nS/pF
G_{Ks}^{epi}, G_{Ks}^{endo}	Maximal epi- and endocardial I_{Ks} conductance	0.392 nS/pF
G_{Ks}^{mid}	Maximal midmyocardial I_{Ks} conductance	0.098 nS/pF
p_{KNa}	Relative I_{Ks} permeability to Na^+	0.03
G_{CaL}	Maximal I_{CaL} conductance	3.98×10^{-5} cm/(ms·μF)
k_{NaCa}	Maximal I_{NaCa}	1.000 pA/pF
γ	Voltage dependence parameter of I_{NaCa}	0.35
K_{mCa}	Ca_i half-saturation constant for I_{NaCa}	1.38 mM
K_{mNai}	Na_i half-saturation constant for I_{NaCa}	87.5 mM
k_{sat}	Saturation factor for I_{NaCa}	0.1
α	Factor enhancing nature of I_{NaCa}	2.5

Table 3.1 (continued).

P_{NaK}	Maximal I_{NaK}	2.724 pA/pF
K_{mK}	K_o half-saturation constant for I_{NaK}	1mM
K_{mNa}	Na_i half-saturation constant for I_{NaK}	40 mM
G_{pK}	Maximal I_{pK} conductance	0.0146 nS/pF
G_{pCa}	Maximal I_{pCa} conductance	0.1238 nS/pF
K_{pCa}	Half-saturation constant of I_{pCa}	0.0005 mM
G_{bNa}	Maximal I_{bNa} conductance	0.000290 nS/pF
G_{bCa}	Maximal I_{bCa} conductance	0.000592 nS/pF
G_{maxup}	Maximal I_{up} conductance	0.006375 mM/ms
K_{up}	Half-saturation constant of I_{up}	0.00025 mM
G_{rel}	Maximal I_{rel} conductance	40.8 mM/ms
k'_1	R to O and RI to I I_{rel} transition rate	0.15 $mM^{-2}\cdot ms^{-1}$
k'_2	O to I and R to RI I_{rel} transition rate	0.045 $mM^{-1}\cdot ms^{-1}$
k'_3	O to R and I to RI I_{rel} transition rate	0.060 ms^{-1}
k'_4	I to O and RI to I I_{rel} transition rate	0.000015 ms^{-1}
EC	Ca_{SR} half-saturation constant of k_{casr}	1.5 mM
max_{sr}	Maximum value of k_{casr}	2.5 (dimensionless)
min_{sr}	Minimum value of k_{casr}	1 (dimensionless)
G_{leak}	Maximal I_{leak} conductance	0.00036 mM/ms
G_{xfer}	Maximal I_{xfer} conductance	0.0038 mM/ms
Buf_c	Total cytoplasmic buffer concentration	0.2 mM
K_{bufc}	Ca_i half-saturation constant for cytoplasmic buffer	0.001 mM
Buf_{sr}	Total sarcoplasmic buffer concentration	10 mM
K_{bufsr}	Ca_{sr} half-saturation constant for sarcoplasmic buffer	0.3 mM
Buf_{ss}	Total subspace buffer concentration	0.4 mM
K_{bufss}	Ca_{ss} half-saturation constant for subspace buffer	0.00025 mM

Calculations of AP were performed with free software COR (Cellular Open Resource) [74]. COR is a Microsoft Windows environment for cellular modeling that

Table 3.2: Parameters for modified ion-channel model.

Parameter	Definition	Value
G_{NaL}	Maximal I_{NaL} conductance	0.0113 nS/pF
τ_{hL}	Inactivation time constant for I_{NaL}	600 ms
ν_{max}	Maximal flux of I_{NaCa}	8.8 pA/pF
γ	Voltage dependence parameter of I_{NaCa}	0.35
$K_{mCaiDis}$	Intracellular Ca dissociation constant for I_{NaCa}	0.0036 mmol/L
$K_{mNaiDis}$	Intracellular Na dissociation constant for I_{NaCa}	12.3 mmol/L
K_{mCaAct}	Half-maximal Ca induced activation of I_{NaCa}	1.50 x10^{-4} mmol/L
k_{sat}	Saturation factor for I_{NaCa} at negative potentials	0.27

utilizes an open standard language CellML [71], based on XML markup language. COR offers an access to a large database of single cell models coded in CellML.

3.3 The modified ion-channel model

The TP [70] model the electrical AP of human ventricular myocytes described in Section 3.2 above has some disadvantages. It does not include formulation for the late Na^+ (slowly inactivating) current I_{NaL} existing in human ventricle myocytes [75], that plays an important role in gender-dependent arrhythmia susceptibility [76], heart failure [77] and formulation for the sodium calcium exchanger current I_{NaCa} was taken from the guinea pig model [78]. To eliminate these drawbacks, we refine the total transmembrane ionic current I_{ion} in the original TP model by changing formulation of sodium-calcium exchanger current I_{NaCa} and adding late (slowly inactivating) sodium current I_{NaL}:

$$I_{ion} = I_{Na} + I_{K1} + I_{to} + I_{Kr} + I_{Ks} + I_{CaL} + \boldsymbol{I_{NaCa}} + I_{NaK} + I_{pCa} + I_{pK} + I_{bCa} + I_{bNa} + \boldsymbol{I_{NaL}}. \quad (3.4)$$

We used the allosteric formulation of Na^+/Ca^{2+} exchanger current I_{NaCa} introduced by Weber *et al.* [79] where I_{NaCa} was represented by an electrochemical (ΔE) and an allosteric (*Allo*) factors. We accepted the data for human ventricular cells from [80] (see Table 3.2 for parameters):

$$I_{NaCa} = Allo \cdot \Delta E; \tag{3.5}$$

$$Allo = \frac{1}{1+\left(\frac{K_{mCaAct}}{Ca_i}\right)^2}; \tag{3.6}$$

$$\Delta E = \frac{v_{\max}\left(Na_i^3 Ca_O \exp\left[\frac{\gamma VF}{RT}\right] - Na_O^3 Ca_i \exp\left[\frac{(\gamma-1)VF}{RT}\right]\right)}{\left(1+k_{sat}\exp\left[\frac{(\gamma-1)VF}{RT}\right]\right)\left(\begin{array}{l} K_{mCa}Na_i^3 + K_{mNai}^3 Ca_i + K_{mNaiDis}^3 Ca_O\left(1+\frac{Ca_i}{K_{mCaiDis}}\right) \\ +K_{mCaiDis}Na_O^3\left(1+\frac{Na_i^3}{K_{mNaiDis}^3}\right) + Na_i^3 Ca_O + Na_O^3 Ca_i \end{array}\right)}. \tag{3.7}$$

We fitted the parameters of ion-channel kinetics to available experimental data from human ventricular myocytes to let our model APD lie more in the midrange of experimental data [81, 82].

A slow inactivating and reactivating late Na^+ current (I_{NaL}) in human ventricular myocytes has been implicated in the action potential plateau [77]. For activation of I_{NaL} we use kinetics and steady-state voltage dependence of I_{NaL} from original TP model [70]:

$$I_{NaL} = G_{NaL} m_L^{\,3} h_L (V - E_{NaL}), \tag{3.8}$$

where m_L and h_L are activation and inactivation gates for I_{NaL}, respectively.

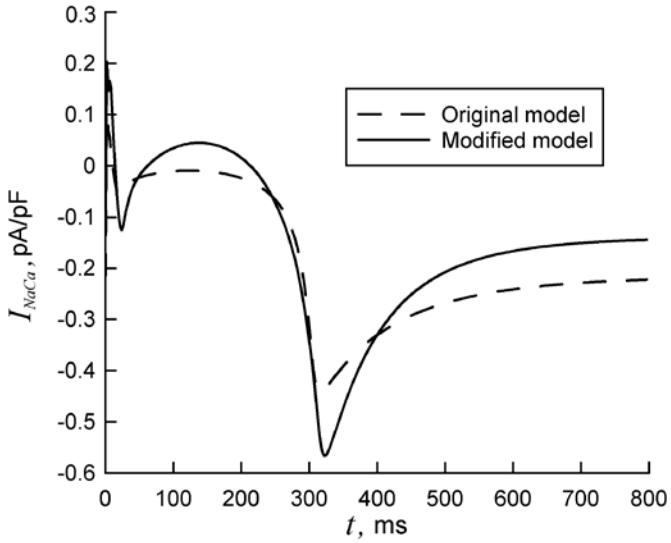

Figure 3.3: Calculated time dependencies of sodium-calcium exchanger current I_{NaCa} for original TP and modified models.

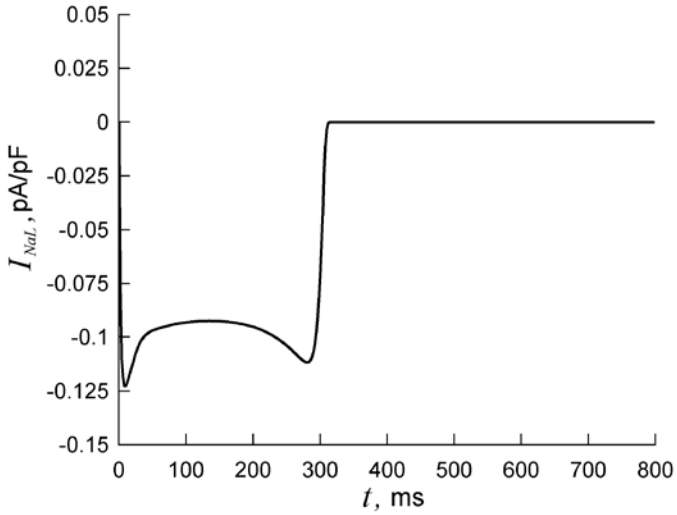

Figure 3.4: Calculated time dependencies of late sodium current I_{NaL} for modified model.

The voltage dependence and kinetics of inactivation are based on data from human ventricular myocytes [82, 83] (see Table 3.2 for parameters).The formulation of I_{NaL} inactivation was adapted from Hund and Rudy [84]. The equations for the activation m_L and inactivation h_L gates are as follows:

$$m_L^i = m_\infty - \left(m_\infty - m_L^{i-1}\right)\exp\left(-\frac{\Delta t}{\tau_m}\right); \tag{3.9}$$

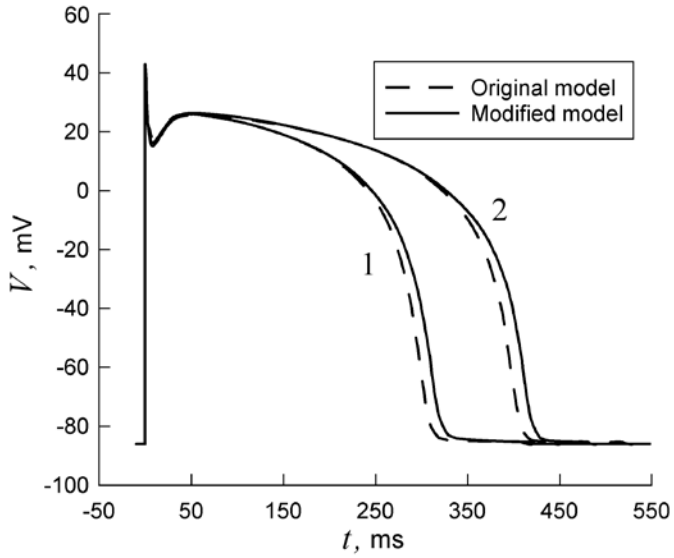

Figure 3.5: Comparison of action potential waveforms with minimal (curve 1) and maximal (curve 2) durations calculated with the original and modified ion-channel models.

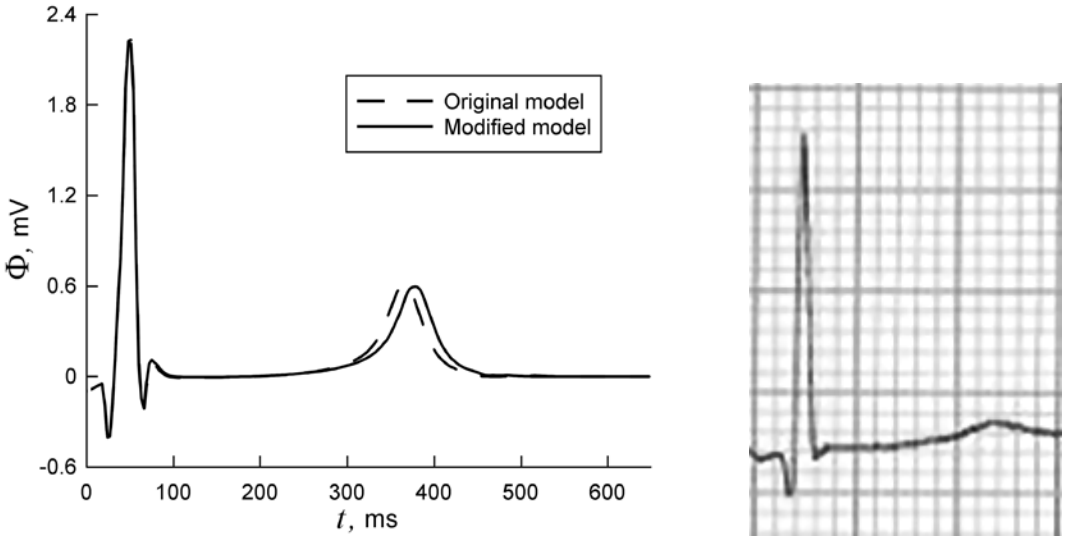

Figure 3.6: Comparison of lead V5 ECG waveforms calculated with the original and modified ion channel models (left) and clinical ECG [8] (right).

$$m_{\infty} = \frac{1}{\left(1+\exp\left(\frac{-56.86-V}{9.03}\right)\right)^2}; \qquad (3.10)$$

$$\tau_m = \frac{1}{1+\exp\left(\frac{-60-V}{5}\right)} \cdot \left\{ \frac{0.1}{1+\exp\left(\frac{V+35}{5}\right)} + \frac{0.1}{1+\exp\left(\frac{V-50}{200}\right)} \right\}; \quad (3.11)$$

$$h_L^i = h_{L\infty} - \left(h_{L\infty} - h_L^{i-1}\right)\exp\left(-\frac{\Delta t}{\tau_{hL}}\right); \quad (3.12)$$

$$h_{L\infty} = \frac{1}{1+\exp\left(\frac{V+94}{6.9}\right)}; \quad (3.13)$$

where Δt is time step, τ_m and τ_{hL} are activation and inactivation time constants for I_{NaL}, respectively, and i is the iteration index. Equations (3.9) and (3.12) represent the solution of gating equations [73] with Rush-Larsen method [85-86].

Figures 3.3 and 3.4 show the obtained time dependencies of I_{NaCa} for original and modified models and I_{NaL}, respectively. The calculated minimal (epicardial) and maximal (midmyocardial) AP and lead V5 ECG waveforms for the modified model and their comparison with the original TP model are demonstrated in the Figs. 3.5 and 3.6, respectively.

3.4 Simulation study of AP distribution and T wave morphology

3.4.1 Introduction

For long time, people could not explain why we see positive T waves in the body surface ECG. Because the depolarization of the ventricles spreads in the direction from endocardium to the epicardium, and the polarity of action potential is opposite for depolarization and repolarization, we should see negative T waves in main leads of the surface ECG. The theoretical model of T wave published by Harumi *et al.* [22] attributes positive T waves to the distribution of APD in the whole heart. The Harumi model says that there is a positive APD gradient along the epi-to-endocardial direction, as well as the base-to-apical direction, and this gradient is larger than the time difference of repolarization along these directions. Recently, however, the existence

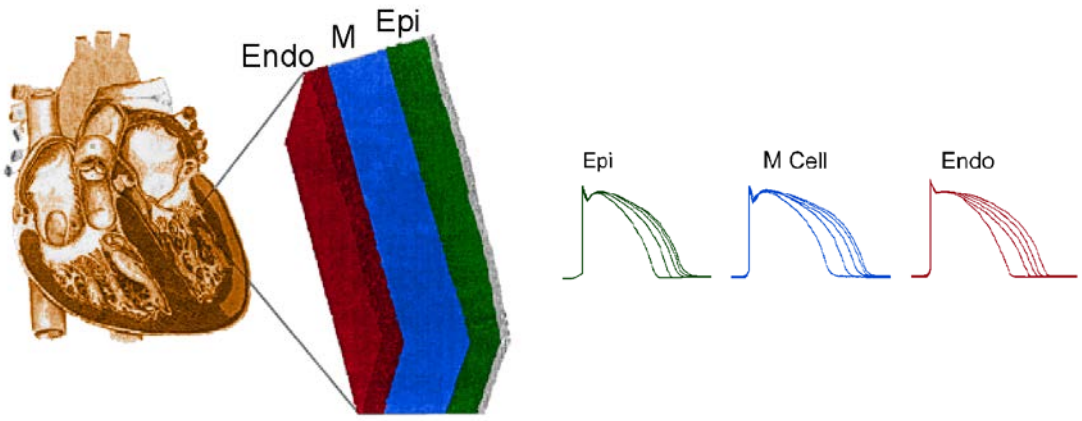

Figure 3.7: Three types of myocardial cells: epicardial, midmyocardial (M cell), and endocardial (left) and corresponding typical action potential waveforms (right), adopted from [88].

of midmyocardial cells (M cells) has been widely discussed, and it is said the M cell has longest APD in the myocardium. This hypothesis is a new challenge to Harumi T wave model, and it is time to verify the relation between the distribution of APD and T wave morphology taking into account the M cells concept. In this chapter, we investigate this relation by computer simulation based on a combined whole-heart and ion-channel model.

Transmural (across ventricular wall) heterogeneity of action potentials is considered to be an important factor for understanding electrophysiological proprieties of the heart and arrhythmic mechanisms. Experimental studies on isolated ventricular cells have demonstrated that three functionally different cell types exhibit distinct electrophysiological profile. These cell types include endocardial cells, epicardial cells, and a subpopulation of midmyocardial cells (M cells) (see Fig. 3.7) [89–91]. It was demonstrated by Antzilevich *et al.* (see, for example [90]) that M cells with action potential duration APD longer than those of endocardial and epicardial cells are located in midmyocardium of left ventricular anterior and lateral walls and septum. Although recently M cells became a debated issue [92], we assume the presence of M cells in the ventricular midwall and include them in this study. It has been shown that transmural voltage gradients during repolarization contribute importantly to the T wave and correlations have been found between cellular events and the surface signal.

Limited number of experimental works was performed on studies of AP transmural heterogeneity in human myocardium [93, 94]. The results provide only partial

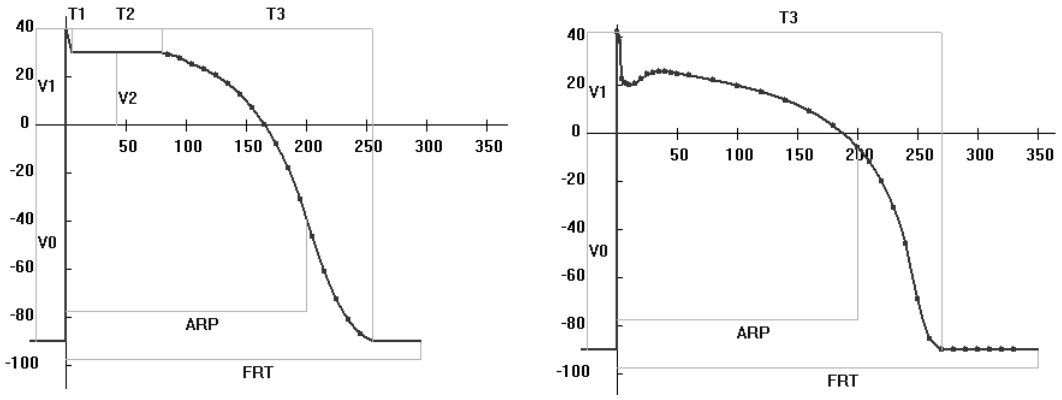

Figure 3.8: Original parametric (left) and calculated with ion-channel model (right) action potential waveforms.

information from isolated regions of the myocardial tissue and do not represent the entire heart. Still it remains unclear how exactly three types of ventricular cells (epi-, endo-, and midmyocardial) are distributed throughout the heart tissue. In computer simulation studies many researchers use 2D and 3D ventricular slab structures [95, 96] where these cells are located as discrete layers in different proportions based on studies of Drouine *et al.* [91]. One can assume that such layered structure should not be homogeneous with constant APD in each layer, because such arrangement leads to great differences in duration on the borders between the cell layers. In particular, this is related to the right ventricle free wall where the tissue layer is thinnest. The heterogeneous structure with smooth changes form short to long, and then from long to short APD across the myocardial walls can overcome the APD discontinuity.

Continuous variation of APD across the ventricular wall has been shown in the experimental works [89, 91, 92], which noted the reduction of the *in vitro* difference in APD between M cells and endocardial/epicardial cells to much smaller *in vivo* values due to the effect of electrotonic coupling. The hypothesis of continuous APD distribution found some confirmation in 3D biventricular computer simulations [95–97].

In this Section, we utilize the modified biventricular model incorporating updated realistic ion-channel model described in Sections 3.2 and 3.3 for calculating electrical AP of ventricular myocytes. We also propose and implement a method that allows obtaining smooth heterogeneous ventricular AP distribution depending on thickness variation of different myocardial walls. The distribution of AP durations and shapes is based on continuous assignment of slow delayed rectifier current values.

The purpose of this chapter is to analyze the validity of the proposed APD distribution of three myocardial cell types over the ventricular tissue, investigating the shape and amplitude of the T wave. Since the T wave is the result of spatial heterogeneity in the ventricular APD, we vary the minimal and maximal APD of epicardial and midmyocardial cells and study its influence on the T wave formation.

3.4.2 Combined three-dimensional human biventricular and ion-channel models

For simulations in this Chapter, we utilize biophysically based model comprising combination of the three-dimensional human biventricular and ion-channel models [30]. The general description of the 3D Wei-Harumi model was given in Chapter 2. Instead of using the parametrically described AP waveforms, we employ for calculation the ion-channel model by ten Tusscher and Panfilov [70] with our modifications for total transmembrane ionic current I_{ion} given by Eq. (3.4).

We fitted the parameters of ion-channel kinetics to available experimental data from human ventricular myocytes to let our model APDs lie more in the midrange of experimental data [81, 82]. Comparison of original parametric and calculated with ion-channel model AP waveforms is shown in Fig. 3.8. The AP were calculated and converted of into Cardiomaster [31] software format with specially developed MATLAB (The MathWorks, Natick, MA, USA) code.

3.4.3 Distribution of action potential duration

The original Wei-Harumi model implements continuous distribution assuming that the APD is a simple linear function of the distance from epicardial-to-endocardial and base-to-apex directions [see Fig. 2.2(b)]. Such distribution is not describing correctly ventricular wall structure according to modern knowledge [88–93].

The main idea of the method we propose is to distribute ventricle APDs without significant discontinuities and boundaries between three different ventricular cell types to obtain such APD distributions in the ventricles taking into account M cells which were missed in the original Wei-Harumi model. At initial step $s = 0$ all cells of the heart model have inactive state (0). At the step $s = 1$ we assign active state (1) to the CA cells on the outermost basal epicardial surface and allow the activation front to

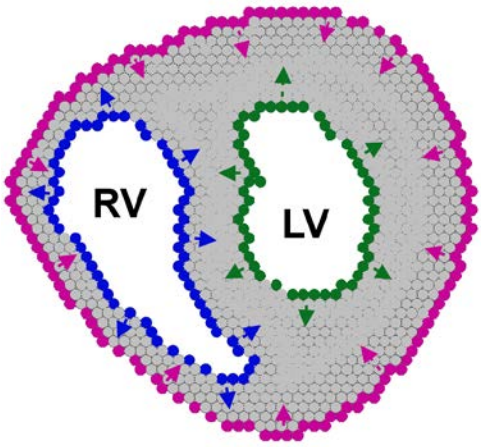

Figure 3.9: Method for setting up the APD distribution.

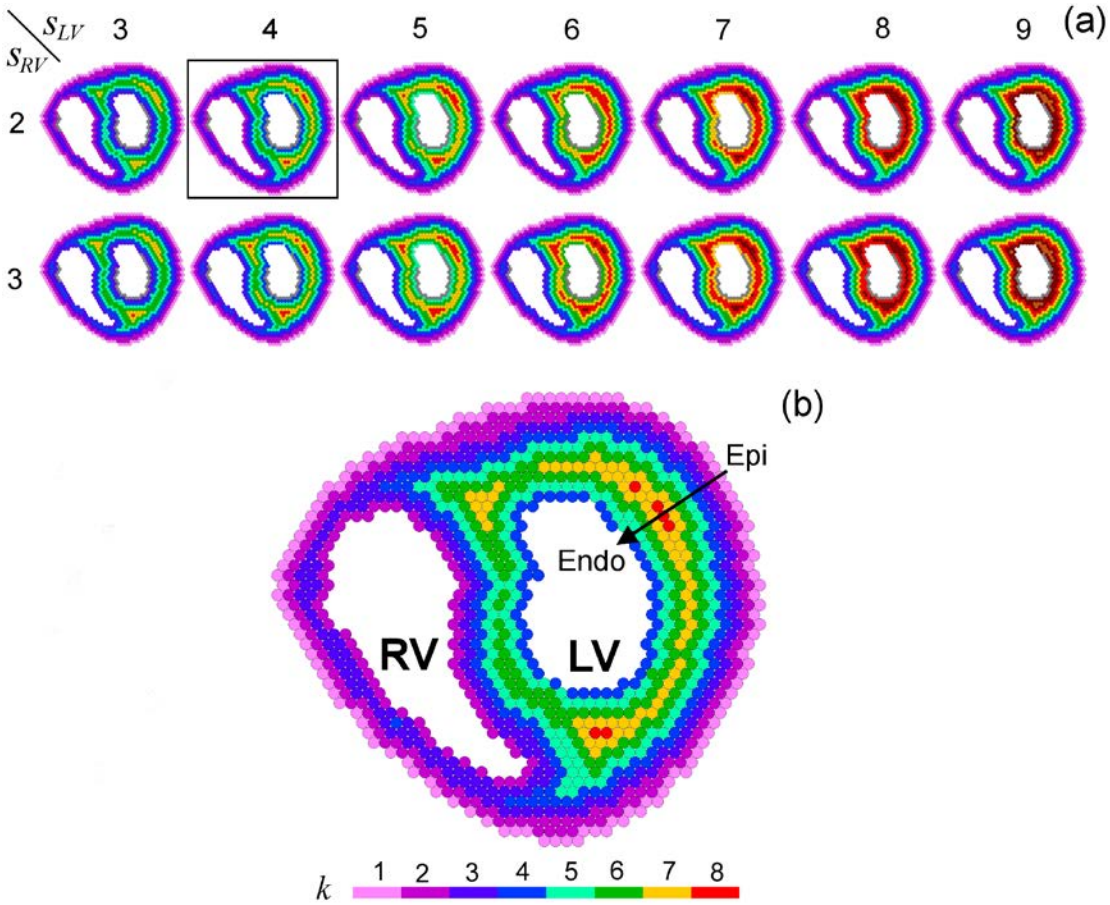

Figure 3.10: The horizontal cross-sections of the 3D heart structure with the layers of CA cells obtained for different steps s_{RV} and s_{LV} (a) and the pattern chosen for this study (b). RV and LV represent the right and left ventricles, respectively, and k is the index of model cell layer.

propagate on one neighboring CA cell at each step in epicardial-to-endocardial and base-to-apex directions (Fig. 3.9).

Meanwhile, we assign active state to the CA cells on the RV and LV basal endocardial (innermost) surfaces at steps s_{RV} and s_{LV}, respectively, causing the propagation of activation fronts in opposite (endocardial-to-epicardial and base-to-apex) directions with the same rate. Then the CA activation fronts meet in the depth of the myocardium and annihilate each other (see Fig. 3.9).

We mark CA cells activated on each step by the corresponding index k, which later is used for calculation of the AP parameters for each heart model cell. The obtained horizontal cross-sections of the 3D heart structure with the layers of CA cells for different steps s_{RV} and s_{LV} are shown in Fig. 3.10(a). Midmyocardial islands of cells appearing in the points where the activation fronts come into contact are considered as M cells (yellow and red colors). We chosen pattern obtained with s_{RV} = 2 and s_{LV} = 4 [Fig. 3.10(b)] as yielding the most realistic normal ECG waveforms.

The most important distinction between epicardial and midmyocardial cells APD is the difference in slow delayed rectifier current I_{Ks} value [98], and the APD is a function of maximal I_{Ks} conductance G_{Ks}. For calculation of AP waveform and APD_{90} value (determined as action potential duration at 90% repolarization), the dynamic restitution protocol proposed by Koller *et al*. [99] was used. A series of 100 stimuli was generated at fixed cycle length (800 ms) until a steady-state APD is reached. This procedure was repeated to calculate APD_{90} for each model cell with index k (k = 1…K) changing the value of G_{Ks} from epicardial value G_{Ks}^{epi} to midmyocardial value G_{Ks}^{mid} with six different dependences on k (linear and nonlinear):

$$G_{Ks}^{A}(k) = G_{Ks}^{epi} - \left(k/K\right)\cdot\left(G_{Ks}^{epi} - G_{Ks}^{mid}\right) \tag{3.14}$$

$$G_{Ks}^{B}(k) = G_{Ks}^{epi}\cdot\exp\left[\left(k/K\right)\cdot\log\left(G_{Ks}^{mid}/G_{Ks}^{epi}\right)\right], \tag{3.15}$$

$$G_{Ks}^{C}(k) = G_{Ks}^{epi}\cdot\exp\left[\left(k/K\right)^{2}\cdot\log\left(G_{Ks}^{mid}/G_{Ks}^{epi}\right)\right], \tag{3.16}$$

$$G_{Ks}^{D}(k) = G_{Ks}^{epi}\cdot\exp\left\{\left[1-\cos\left(\pi k/K\right)\right]/2\cdot\log\left(G_{Ks}^{mid}/G_{Ks}^{epi}\right)\right\}, \tag{3.17}$$

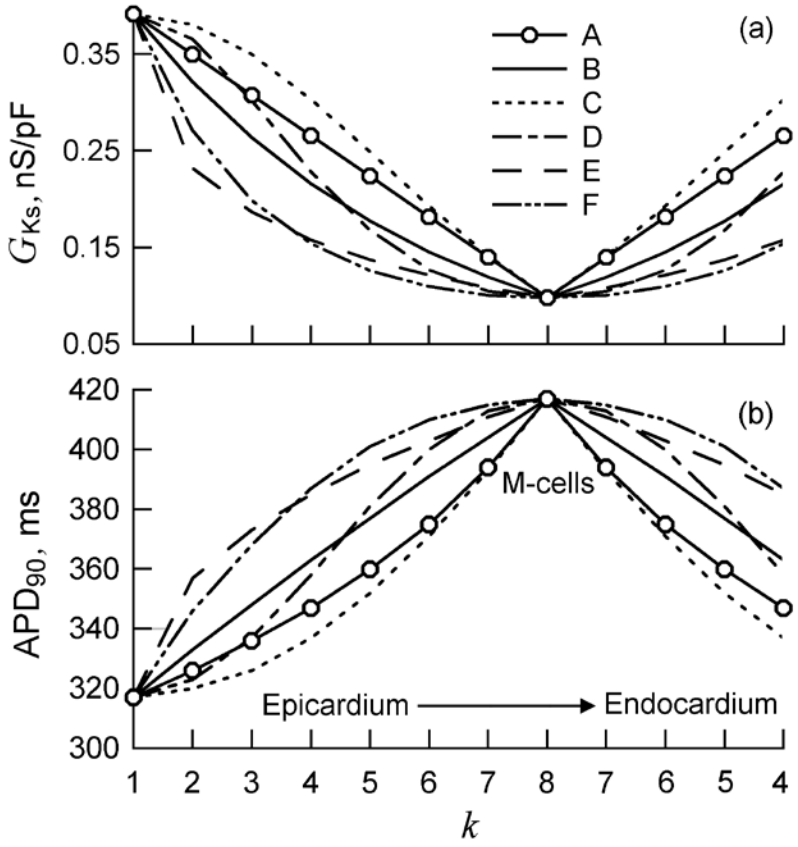

Figure 3.11: Distributions of maximal slow delayed rectifier current conductance G_{Ks} (a) and resulting calculated distributions of APD_{90} (b). The curves A–F correspond to the functions $G_{Ks}^{A}(k)$, $G_{Ks}^{B}(k)$,… $G_{Ks}^{F}(k)$ given by (3.14) – (3.19).The distributions correspond to the transverse cross-section of the left lateral ventricular wall marked by the black arrow in Fig. 3.10(b).

$$G_{Ks}^{E}(k) = G_{Ks}^{epi} \cdot \exp\left[\sqrt{k/K} \cdot \log\left(G_{Ks}^{mid} / G_{Ks}^{epi}\right)\right], \tag{3.18}$$

and

$$G_{Ks}^{F}(k) = G_{Ks}^{epi} \cdot \exp\left\{\left[1-\left(k/K\right)^{2}\right] \cdot \log\left(G_{Ks}^{mid} / G_{Ks}^{epi}\right)\right\}, \tag{3.19}$$

Here $K = 8$ is maximal layer number [see Fig. 3.10(b)]. Distribution of G_{Ks} value from midmyocardium to endocardium (mirrorly) dissymmetrically repeats the epicardial-midmyocardial one. Figure 3.11(a) shows the G_{Ks} dependence on the index of model cell layer k, and Fig. 3.11(b) demonstrates the resulting calculated APD_{90} distributions for the six dependences in question (3.14) – (3.19).

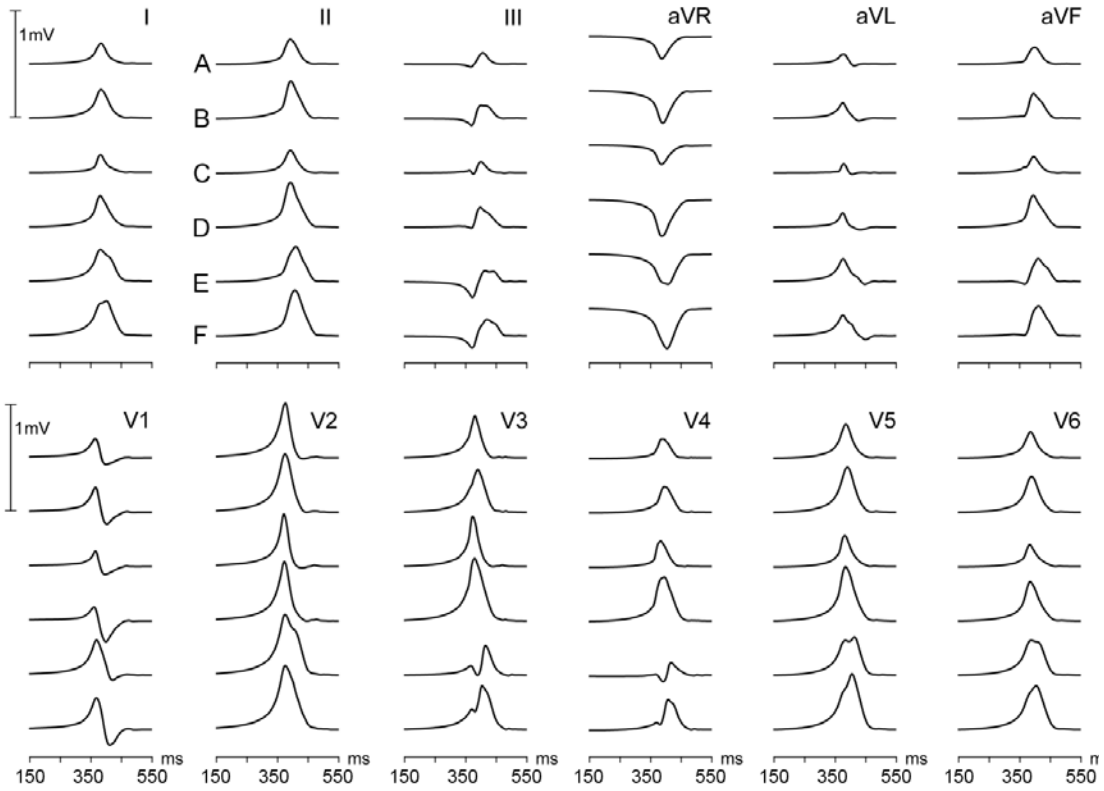

Figure 3.12: ECG waveforms with different T wave shapes for six different APD_{90} distributions calculated with functions $G_{Ks}^{A}(k)$, $G_{Ks}^{B}(k)$,… $G_{Ks}^{F}(k)$ given by equations (3.14) – (3.19). QRS complex is not shown. Horizontal axis shows time from the moment of stimulation of ventricles.

3.4.4 T wave morphology - simulation results

First, we investigated the influence of proposed distributions of G_{Ks} value, and thus obtained distributions of APD_{90} values on the ECG waveforms, in particular, T waves, performing single beat simulations with the cycle length of 800 ms.

Figure 3.12 demonstrates the ECG waveforms with different T wave shapes simulated for the APD_{90} distribution dependences calculated with the functions (3.14) – (3.19). The obtained waveforms were analyzed in order to find out the most appropriate shape corresponding to the normal ECG ranges.

For the distributions B (3.15), D (3.17), and F (3.19) first limb of T wave is moving faster than second limb which is abnormal for healthy human heart. The T waves in case C (3.16) are too weak and narrow. There are pronounced notches on T waves in distribution E (3.18). Accordingly, for further simulation study we chose

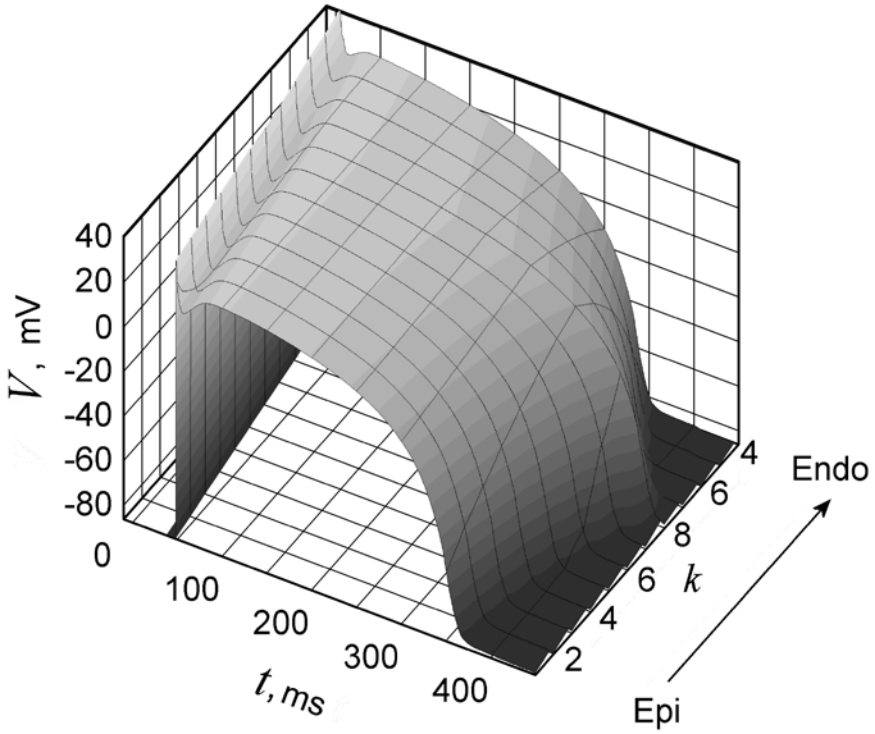

Figure 3.13: Action potential waveforms from the epicardium to endocardium for linear distribution of G_{Ks} (3.14).

linear distribution of G_{Ks} [function A (3. 14)] since it yields more realistic T wave shapes.

Figure 3.13 shows the calculated distribution of APD waveforms ranging from epicardial to endocardial surface for linear distribution of G_{Ks} (3.14).

Figure 3.14 shows APD, excitation, and repolarization distributions for six different horizontal cross-sections of the model heart from base to apex calculated with the modified model. In the demonstrated APD distribution, the cells with longest AP are located in the left ventricular wall and septum and the shortest one in right ventricle [Fig. 3.14(a)]. The obtained APD gradients between the model heart apex and base, and left and right ventricles are similar to those reported in the experimental works [99–101]. The excitation sequence [Fig. 3.14(b)] resembles that described by Durrer *et al.* in the human heart [33]. It is seen from Fig. 3.14(c) that the repolarization time is shortest in the epicardial and endocardial cells, while it is longest in the midmyocardial cells that follows from the summation of excitation sequence time and AP distribution.

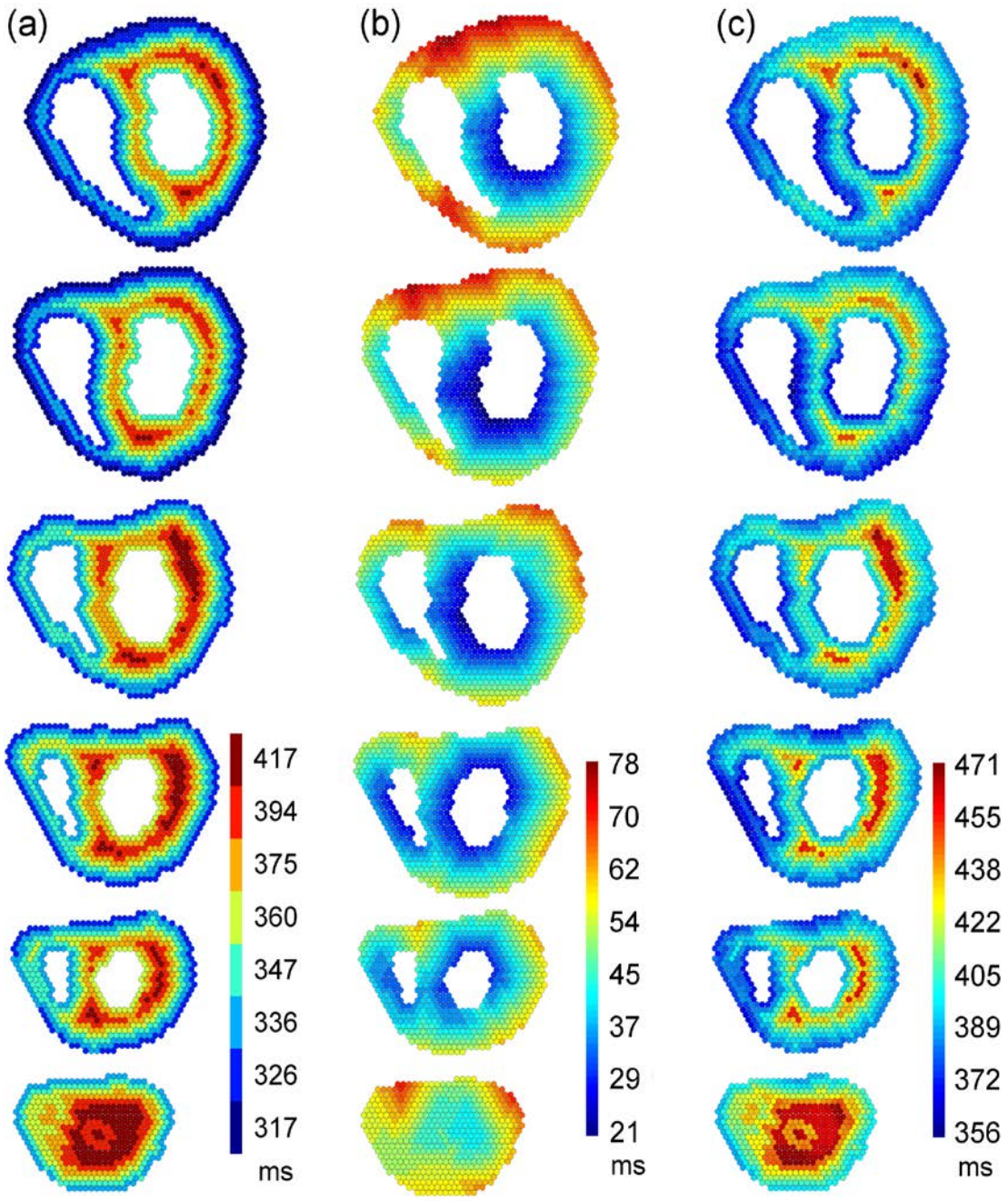

Figure 3.14: Action potential duration (a), excitation (b) and repolarization (c) distributions for six different horizontal cross-sections of model heart from base (top) to apex (bottom) for linear distribution of G_{Ks} (3.14). The time for the excitation and repolarization is shown from the moment of stimulation of ventricles.

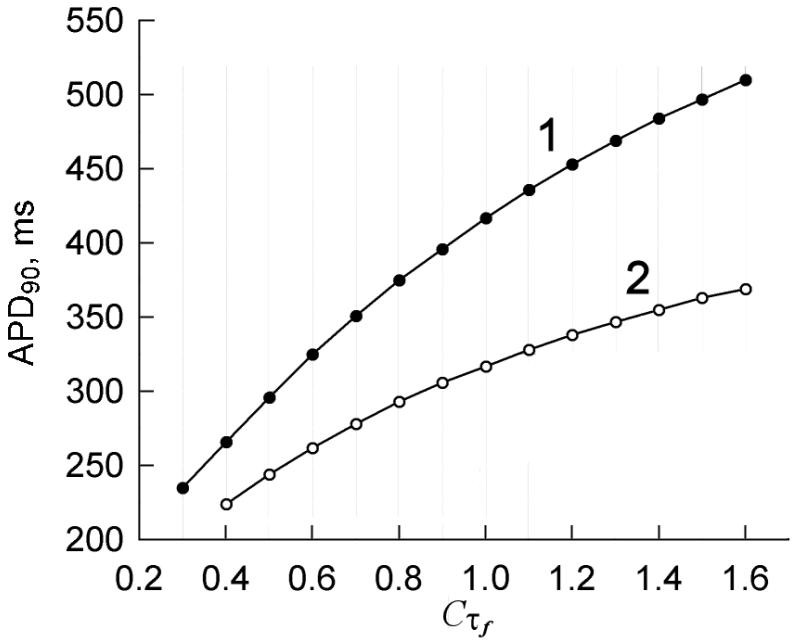

Figure 3.15: Dependences of the minimal (curve 1) and maximal (curve 2) APD_{90} on the multiplication factor $C\tau_f$.

Variation of the G_{Ks} value beyond the limits used in the original TP ion-channel model [70] resulted in the significant deformation of the AP waveforms in fast and slow repolarization phases (in the interval approximately from 50 to 300 ms in Fig. 3.13). Thus, to change the dispersion of APD along with G_{Ks} value we used the variation of inactivation time constant τ_f for the f gate [70], multiplying it on an additional parameter $C\tau_f$. The parameter $C\tau_f$ was altered only for the range $V > 0$, thus varying the inactivation but not recovery kinetics of L-type calcium current I_{CaL}. The resulting dependences of the maximal and minimal APD_{90} values on $C\tau_f$ are shown in Fig. 3.15.

The simulated ECG waveforms for leads II and V5 with variation of $C\tau_f$ are demonstrated in Fig. 3.16. The potential of lead II is calculated as a potential difference between right hand and left leg (points R and F on Fig. 2.5, respectively). The increase of $C\tau_f$, and, consequently, widening the positive voltage part of an AP simultaneously for both minimal (epicardial cells) and maximal (M cells) APD_{90} leads to rising of amplitude, width, and later end point of the T wave [see Fig. 3.16(a)]. It takes place due to increasing number of M cells with longest APs. The enlargement of $C\tau_f$ separately for the maximal and minimal APD_{90} results in increasing transmural

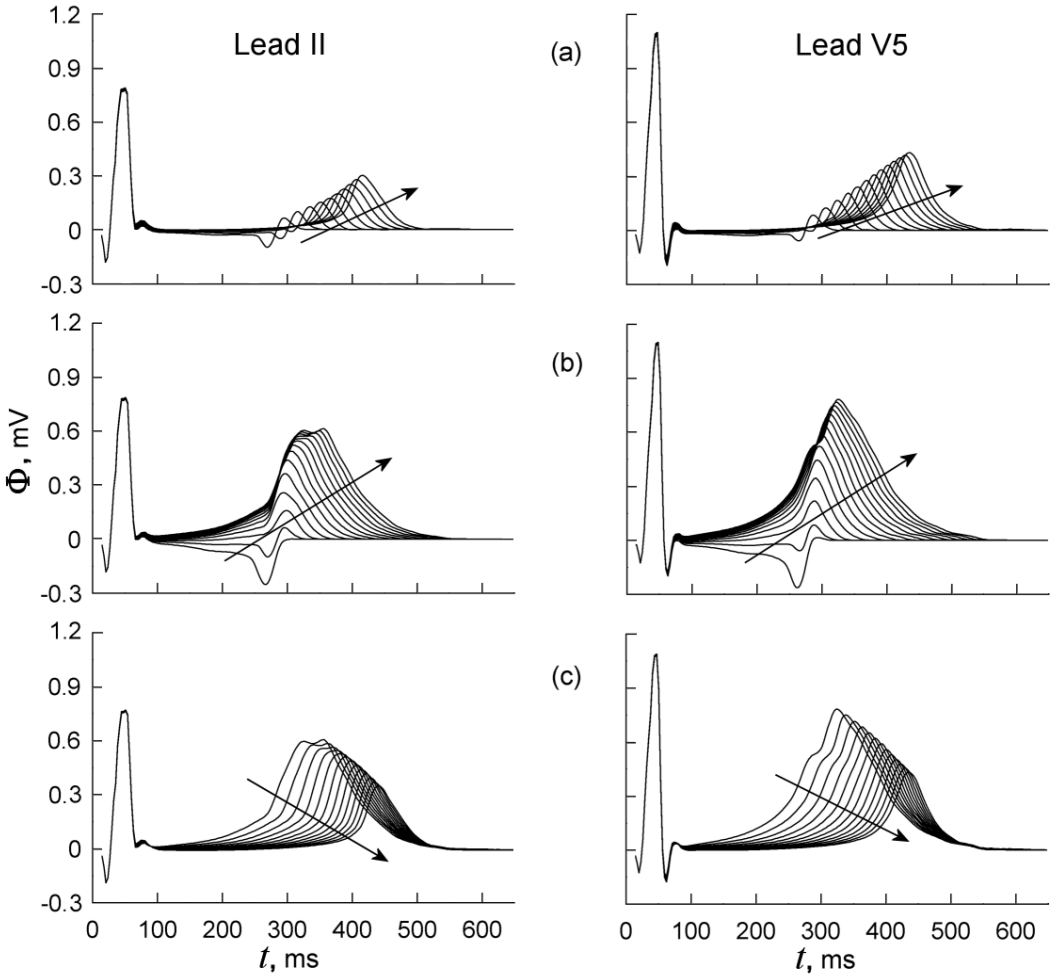

Figure 3.16: Calculated ECG waveforms (leads II and V5) for different values of the multiplication factor $C\tau_f$: (a) $C\tau_f$ increases from 0.4 to 1.3 along the arrow direction simultaneously for both minimal (epicardial) and maximal (midmyocardial) APD_{90}; (b) $C\tau_f$ is constant (0.4) for minimal APD_{90} while it increases from 0.3 to 1.6 for maximal APD_{90} along the arrow direction; (c) $C\tau_f$ is constant (1.6) for maximal APD_{90} while it increases from 0.4 to 1.3 for minimal APD_{90} along the arrow direction. $C\tau_f$ varies with 0.1 step for all figures here.

gradient of APD. In Fig. 3.16(b) longer maximal APD_{90} correlating with the repolarization of M cells significantly prolongs the QT interval, similar to reported in the works [102–104]. The increase of minimal APD_{90} associated with prolongation of epicardial repolarization and enlargement of transmural gradient manifests in a rise of the ST segment duration and diminishing of amplitude and width of the T waves [Fig. 3.16(c)].

3.4.5 Discussion and conclusion

In this chapter, we demonstrated computer simulations utilizing the developed combined 3D human biventricular and ion-channel model with new inhomogeneous continuous APD distribution. We supposed that the APD distribution is continuous from epicardium to midmyocardium and from midmyocardium to endocardium solely due to regional variations in densities of membrane ionic currents. We assumed that M-cells have the lowest density of I_{Ks} in the human ventricle [98], and thus longer APD than epicardial and endocardial cells, without any specific morphological features. In this regards our study is close to the work published by Trudel *et al*. [97]. These researchers obtained continuous APD distribution across the myocardium, with less APD deviation of three cell types in the thinner right ventricle.

Six different distribution functions of G_{Ks} on layer index were considered. The linear G_{Ks} and corresponding APD dependences were chosen for further ECG simulations as demonstrating most realistic T wave shapes.

The formation of T wave depends on the difference between the shortest and the longest APs. We supposed that AP in epicardial cells is always shorter in comparison to endo- and midmyocardial cells. The obtained midmyocardial zeniths are located as islands in the depth of thickest ventricular walls [105], which can explain technical difficulties in finding and locating of M cells experimentally. The controversy in M cell existence is reflected in recent works [90, 106, 107].

If the contraction rate is constant over the whole myocardium, the thick (left) ventricular wall shrinks and relaxes slower than the thin (right) wall, thus cells in thick wall should have longer APD, and so the thickness of M cells region could have a functional significance [108].

The amplitude and width of T wave increase with enlargement of the difference between minimal (epicardial) and maximal (midmyocardial) APDs. The decreasing of transmural heterogeneity leads to diminishing of T wave parameters and its absence results in negative T wave in most ECG leads, which is abnormal.

Our results support the existence of M cells as well as transmural heterogeneity in healthy human heart. However, the M cell definition in our case seems to be inexplicit because the maximal APD values are different in different parts of myocardium, for RV and LV, the base and apex, even for one horizontal cross-section of the heart.

Using our proposed transmural distribution of APD we obtained physiological ratios of the T wave amplitudes in different ECG leads (Fig. 3.12): in lead I the T wave is higher than in lead III, in lead V1 it is lower than in lead V6, and it is negative in lead aVR.

3.4.6 Limitations

In the present work we employed simplified approach for the modulation of APD using only variation of maximal slow delayed rectifier current conductance G_{Ks} and time constant $C\tau_f$ for f gate. We only focused on the study of influence of the APD on the T wave morphology, since the role of the AP shape is insignificant for the normal heart. Thus, we did not include into our ion-channel model any differences between midmyocardial and endocardial cells in values of transient outward current I_{to}, which is responsible for the distinction between AP shapes in phase 1. In addition, if new experimental data on other ionic currents underlying AP waveform variation throughout myocardial tissue become available, the utilization of this current may improve our model.

Although the biventricular model used in this study is rather simple and computationally efficient, the increase of model cells spatial resolution may improve precise tuning of M cells location in the midmyocardium and accuracy of APD distribution, which is especially important for the simulation of cardiac arrhythmias.

Nevertheless, our results are in line with experimental observations [107, 108], in particular, T wave amplitude closely correlates with transmural APD_{90} heterogeneity. Our simulations demonstrated the validity of the proposed continuous heterogeneous APD distribution with islands (zeniths) of M cells [105].

3.5 Chapter summary

In this Chapter, we proposed modified ten Tusscher-Panfilov ion-channel model, changing formulation for I_{NaCa} for human ventricular myocytes and adding the formulation for I_{NaL}, which plays an important role in susceptibility to gender-dependent arrhythmias and heart failure. Furthermore, we proposed and implemented an algorithm for continuous and inhomogeneous distribution of APDs as functions of G_{Ks} in the 3D biventricular heart model in order to incorporate M cells absent in the

Wei-Harumi model. For the simulations, we combined the heart model with the modified ion-channel model of ventricular myocytes in order to implement biophysically based AP waveforms instead of parametrical APs used in original Wei-Harumi model.

We investigated the role of M cells in genesis of T wave by verifying different spatial APD distributions. Different spatial AP distributions have been investigated using three-dimensional biventricular heart model combined with ion-channel model of ventricular myocyte. It has been shown that the proposed distributions which are functions of maximal conductance of slow delayed rectifier current (G_{Kslow}) depend on the thickness of the myocardium tissue. Cells with the longest AP duration values are located in the left ventricular wall and septum as islands. The obtained standard ECG waveforms show that the proposed model reasonably reproduces shapes of normal T waves.

The combination of the heart model and the ion-channel model links clinically comparable simulated results with cellular electrophysiology. In this way, our study shows a good method to validate different assumptions of the role of M cells in understanding the T wave formation.

Chapter 4

Computer simulation of cardiac conduction system with heterogeneous oscillator model

4.1 Introduction

For the simulation of the electrical processes in the heart, various modeling approaches with different levels of details have been proposed and utilized. The majority of the models describe functioning of the heart on the cellular level, obtaining propagation of action potentials among cardiomyocytes. Simulations on 2D or 3D tissue slabs produce pseudo electrograms [109, 110], while 3D biventricular, atrial or whole-heart models coupled with torso model can yield more realistic ECG signals. These models are based on either cellular automaton (as described in Chapter 2) or reaction–diffusion (see, for example, [111, 17] and references wherein) approaches for simulation of excitation waves propagation. The latter approach usually requires a lot of computational resources to solve huge number of differential equations for ionic currents in cell membranes with many parameters.

There is a different class of models, which describe of heartbeat dynamics in general with a set of ordinary differential equations. Some of the models generate synthetic ECG signals using a dynamical system on a circle [112-115] without taking into account structure of the cardiac conduction system. In other models, the heart is compartmentalized into separate elements such as natural cardiac pacemakers only [116-129] or pacemakers and muscles [130-132] using different modifications of the coupled Van der Pol (VDP) type nonlinear relaxation oscillators [133]. Utilization of the modified VDP oscillators allows adoption of their intrinsic frequencies to the driving signal without significantly changing the amplitude, which corresponds to the real interactions between natural cardiac pacemakers. Most of the above mentioned oscillator models are focused on the generation of transmembrane action potentials

Table 4.1: Comparison of nonlinear cardiac models. ODE, HRV, and NPE stand for odinary differential equation, heart rate variability and nerve pulse equation, respectively.

Models using dynamic system on a circle	P. McSharry, G. Clifford *et al.* (2003-2007)	3x 1st order ODE	ECG+ HRV
	W. Thanom *et al.* (2011)	3x 1st order ODE (Zeeman)	ECG
	M. Gidea *et al.* (2011)	3x 1st order ODE	ECG
Models of natural pacemakers	S. Sato *et al.* (1994)	1x Bonhoeffer-VDP	
	D. Di Bernardo *et al.* (1998)	2x VDP	
	M. Yoneyama *et al.* (2004)	Nx Bonhoeffer-VDP	
	A.M. Dos Santos *et al.* (2008)	2x VDP	
	B.Z. Kaplan *et al.* (2008)	2x Filtered VDP	ECG
	M. Suchorsky, R. Rand (2009)	3x 1st order ODE	
	S. Das *et al.* (2013)	Fractional order ODE, filtered VDP	ECG
	S. Gois, M. Savi *et al.* (2009)	3x Asymmetric VDP	
Models of natural pacemakers and muscles	O. Kongas *et al.* (1999)	2x Asymmetric VDP + 2x NPE	
	J.J. Zebrowski *et al.* (2004-2013)	2x Asymmetric VDP + 3D tissue	
	E. Ryzhii *et al.* (2014)	3x Asymmetric VDP + 4x FHN	ECG

and the study of their synchronization, bifurcation and chaos, but only a few are intended for calculation of realistic ECG (see Table 4.1). The model proposed by Gois *et al*. [126] allows generating electrical response of three main cardiac pacemakers and obtaining the ECG as a composition these signals. The disadvantage of the model is that in reality the pacemakers signals are rather weak in comparison with the cardiac muscle ones, and do not significantly contribute to the aggregated ECG signal. On the other hand, the responses of atrial and ventricular muscles, which actually produce the main input, were not included in this model. To eliminate this drawback, we incorporated into the system quiescent excitable FitzHugh–Nagumo-type (FHN) oscillators for accurate description on the cardiac muscle electrical responses [134] and their input to the net ECG signal with respect to physiology and for extension of overall functionality of the model.

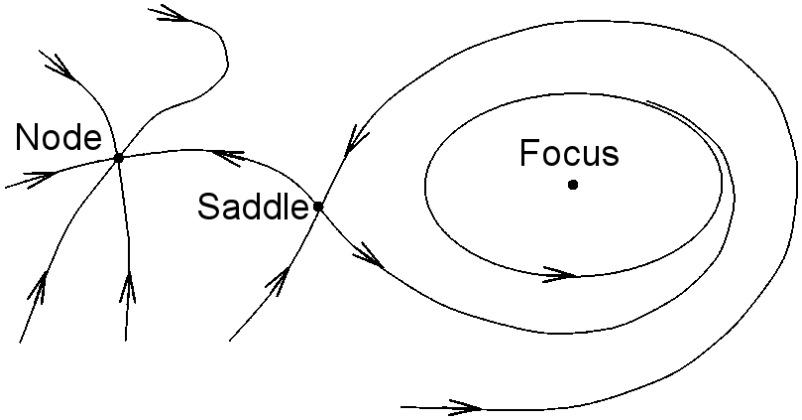

Figure 4.1: Typical phase response of neuronal oscillators [126].

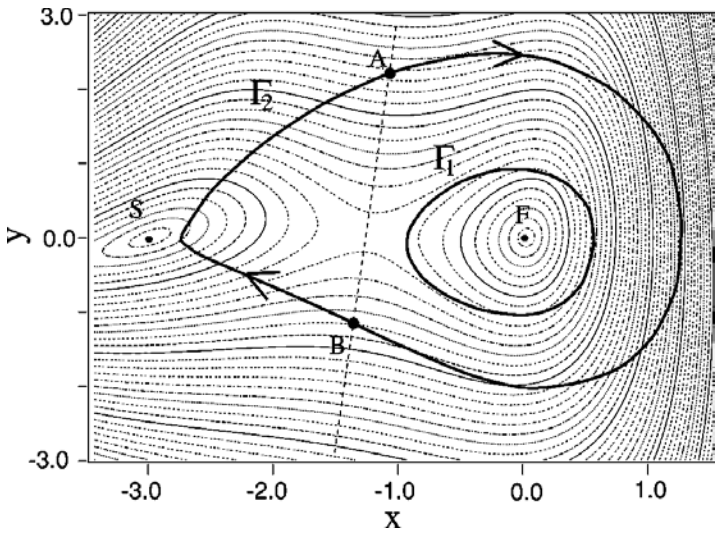

Figure 4.2: Limit cycles for the modified VDP model [136] drawn for u = 0.2 (Γ_1) and u = 1.0 (Γ_2).

4.2 Description of oscillator model

The VDP model [133] has been widely used in theoretical studies of the heart electrical activity. The standard VDP relaxation oscillator equation is given by the following Liénard planar system:

$$\begin{aligned} \dot{x} &= y \\ \dot{y} &= -F(x)y - G(x), \end{aligned} \tag{4.1}$$

where

$$F(x) = \alpha(x^2 - u), \quad G(x) = \omega^2 x, \tag{4.2}$$

$\alpha > 0$ and $u = 1$ are the factors representing nonlinear damping force, ω is the intrinsic natural frequency of the oscillator, and $x(t)$ corresponds to the amplitude of the heart electrical signal, which is related to the cardiac action potential.

Considering the features of neuronal oscillator models, such as Morris–Lecar model [135], Postnov *et al*. [136] proposed a simple oscillator model that is easily controllable and that still reproduces the behavior of the neuronal oscillators. Modifying the standard VDP equation, the authors replaced the linear harmonic force $G(x)$ to cubic Duffing nonlinear term $x(x+d)(x+2d)/d^2$ to maintain the features of the oscillator phase space similar to neuronal one, which includes three equilibrium points – the focus, the saddle, and the stable node (Fig. 4.1). Limit cycles for the modified VDP model [136] calculated with coefficients $u = 0.2$ (Γ_1) and $u = 1.0$ (Γ_2) are shown in Fig. 4.2.

The model was further improved by Grudzinski and Zebrowski [121], who investigated its adaptation for simulation of cardiac pacemaker behavior. To enhance the potential of the model, they changed the damping term $F(x)$ to asymmetric form with respect to the variable x and introduced independent parameters d and e in the force term $G(x)$ for the position control of hyperbolic saddle and stable node, respectively:

$$F(x) = \alpha(x - u_1)(x - u_2), \quad G(x) = \omega^2 x(x + d)(x + e), \tag{4.3}$$

where the product $u_1 u_2$ should be negative to keep the self-oscillatory property of the system.

One of the universal features describing the behavior of interacting oscillator systems is synchronization. It manifests as an adjustment of rhythms (phase-locking with non zero constant phase shift) due to an interaction between two or more oscillators, and does not necessarily require complete temporal coincidence of signals. To provide the interaction in the systems, proper coupling should be set up between the oscillators or pacemaker nodes. A diffusive coupling (nearest-neighbor local coupling) is the most common type of coupling present in physical and biological systems. In the diffusively coupled system, generally coupling terms should include both differences: $(x_i - x_{i-1})$ for position coupling and $(y_i - y_{i-1})$ for velocity coupling, which, in application to the heart system, correspond to the coupling by potential and

current, respectively. As a result, an element $i > 1$ in the unidirectionally coupled oscillator array may look as follows [126]:

$$\begin{aligned} \dot{x}_i &= y_i + K_i^x (x_i - x_{i-1}) \\ \dot{y}_i &= -F_i(x) y_i - G_i(x) + K_i^y (y_i - y_{i-1}), \end{aligned} \tag{4.4}$$

where K_i are the coupling coefficients. However, a number of diffusive coupling method variations can be found in the literature (see, for example, [120, 123, 124, 127, 137]). The asymmetric position-only coupling added to the first equation of (4.4) was used in the spatially dimensional SA–AV model [121], while in the work [126] this coupling term with time delays was added to the second equation.

The utilization of the system (4.4) allows modeling of general behavior of cardiac pacemakers and reproduction of some cardiac phenomena [121], including, to some extent, ECG signals [126]. As we mentioned above in the Introduction, in the model [126] the ECG is obtained as a composition of electrical responses of main cardiac pacemakers only, which are rather weak in comparison with the cardiac muscle ones and do not significantly contribute to the aggregated ECG signal. On the other hand, the responses of atrial and ventricular muscles, which actually produce the main input, were not included in this model.

For correct simulation of ECG signals some description of AT and VN muscles is necessary. In contrast to the properties of the pacemaker cells, cardiac muscle cells do not demonstrate self-oscillatory behavior. They have to be stimulated by an electrical signal from a pacemaker to produce a single response, i.e depolarization, which leads to their contraction. For simulation of atrial and ventricular muscles an equation for quiescent excitable element, such as modified FHN model or VDP model with positive product $u_1 u_2$ [138], is necessary to adequately describe electrical response. These models have a low-level stable oscillatory state for small values of applied stimulating current.

We proposed a modification of the cardiac conduction system model with the description of electrical responses of cardiac muscles on stimulation by pacemakers based on FHN class model [139, 140] for excitable media:

$$\begin{aligned} \dot{z} &= -cz(z - w_1)(z - w_2) - bv + I \\ \dot{v} &= h(z + j - gv). \end{aligned} \tag{4.5}$$

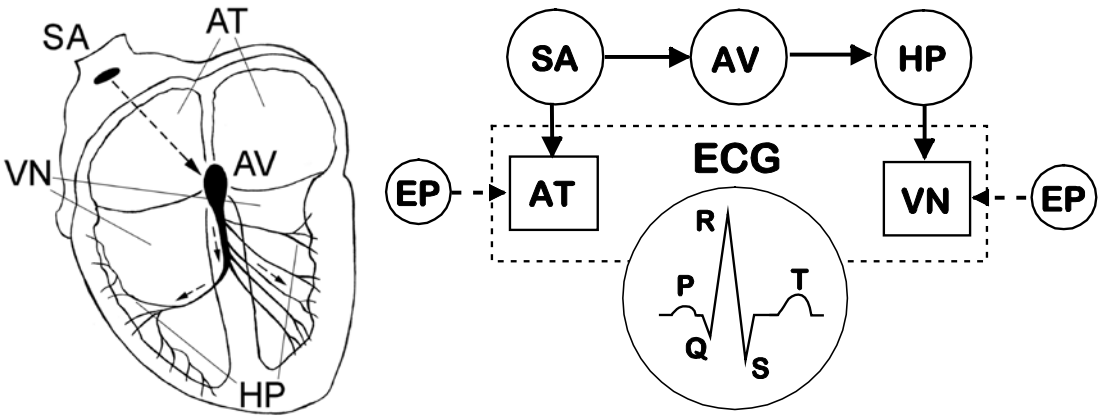

Figure 4.3: General scheme of the proposed cardiac conduction system model. EPs denote external ectopic beats.

Here z is the excitation variable corresponding to the net transmembrane potential of all cells of the muscle, and v is the recovery variable (quantity of refractoriness). The cubic term in the first equation controls the activation, parameter c defines the amplitude of the pulse, and parameters $w_1 \leq w_2$ represent excitation threshold and excited state, respectively. Parameters b, j and g change the rest state and dynamics, h represents excitability and controls the abruptness of activation and the duration of the action potential, and I is the magnitude of stimulation current. Different variations of these equations can be found in literature and sometimes called as Bonhoeffer–van der Pol model. The model is commonly used to describe different biological mechanisms and is able to reproduce many qualitative characteristics of excitable media such as excitation threshold, relative and absolute refractory periods.

Therefore, the proposed modified mathematical model represents a combined system of time-delayed differential equations of two types - modified asymmetric VDP equations for all pacemakers [121, 126] and quiescent excitable FHN equations for AT and VN muscles. General scheme of the proposed cardiac conduction system model is shown in Fig. 4.3. In the first version of the model, we used unidirectional position-only coupling with time delays, similar to the approach introduced in [121]. Thus, the sets of equations for the cardiac pacemakers and muscles look as follows [134]:

Table 4.2: Table of parameters used in equations (4.6) – (4.8) for normal sinus rhythm.

α_1	Damping coefficients for pacemakers	20
α_2		20
α_3		60
α_4 , α_5	Damping coefficient for EP	60
f_1	Parameters defining the amplitude of a pulse	9.0
f_2		9.0
f_3		10.0
d_1	Parameters changing the rest state and dynamics	3.0
d_2		3.0
d_3		3.0
e_1	Parameters controlling the hyperpolarization of the excitation variable	4.7
e_2		3.0
e_3		2.4
u_{11}	Parameters controling excitation threshold	0.83
u_{21}		0.83
u_{31}		0.4
u_{12}	Parameters controling excited state	-0.83
u_{22}		-0.83
u_{32}		-1.1
$K_{\text{SA-AV}}$	Coupling coefficient between SA and AV	400
$K_{\text{AV-HP}}$	Coupling coefficient between AV and HP	400
$\tau_{\text{SA-AV}}$	SA – AV time delay	0.07 s
$\tau_{\text{AV-HP}}$	AV – HP time delay	0.07 s

Table 4.3: Table of parameters used in equations (4.9) – (4.10) for normal sinus rhythm.

c_1, c_2	Parameters defining the amplitude of a pulse	100
b_1, b_2	Parameters changing the rest state and dynamics	2500
j_1, j_2		0.7
g_1, g_2		13
w_{11}, w_{21}	Parameters controling excitation threshold	-1.0
w_{12}, w_{22}	Parameters controling excited state	1.0
h_1, h_2	Parameter representing excitability and controling the abruptness of activation and the duration of the action potential	1.1
$K_{\text{SA-AT}}$	Coupling coefficient between SA and AT	50
$K_{\text{EP–AT}}$	Coupling coefficient between EP and AT	15
$K_{\text{HP-VN}}$	Coupling coefficient between HP and VN	30
$K_{\text{EP–VN}}$	Coupling coefficient between EP and VN	15
$\tau_{\text{SA-AT}}$	SA – AT time delay	0.05 s
$\tau_{\text{HP–VN}}$	HP – VN time delay	0.05 s

$$\text{SN}\begin{cases}\dot{x}_1 = y_1 \\ \dot{y}_1 = -\alpha_1 y_1 (x_1 - u_{11})(x_1 - u_{12}) - f_1 x_1 (x_1 + d_1)(x_1 + e_1)\,,\end{cases} \tag{4.6}$$

$$\text{AV}\begin{cases}\dot{x}_2 = y_2 \\ \dot{y}_2 = -\alpha_2 y_2 (x_2 - u_{21})(x_2 - u_{22}) - f_2 x_2 (x_2 + d_2)(x_2 + e_2) \\ \qquad + K_{\text{SA-AV}} (x_1^{\tau_{\text{SA-AV}}} - x_2)\,,\end{cases} \tag{4.7}$$

$$\text{HP}\begin{cases}\dot{x}_3 = y_3 \\ \dot{y}_3 = -\alpha_3 y_3 (x_3 - u_{31})(x_3 - u_{32}) - f_3 x_3 (x_3 + d_3)(x_3 + e_3) \\ \qquad + K_{\text{AV-HP}} (x_2^{\tau_{\text{AV-HP}}} - x_3)\,,\end{cases} \tag{4.8}$$

and

$$\text{AT}\begin{cases}\dot{z}_1 = -c_1 z_1 (z_1 - w_{11})(z_1 - w_{12}) - b_1 v_1 + K_{\text{SA-AT}} x_1^{\tau_{\text{SA-AT}}} + K_{\text{EP-AT}} x_4 \\ \dot{v}_1 = h_1 (z_1 + j_1 - g_1 v_1)\ ,\end{cases} \tag{4.9}$$

$$\text{VN}\begin{cases}\dot{z}_2 = -c_2 z_2 (z_2 - w_{21})(z_2 - w_{22}) - b_2 v_2 + K_{\text{HP-VN}} x_3^{\tau_{\text{HP-VN}}} + K_{\text{EP-VN}} x_5 \\ \dot{v}_2 = h_2 (z_2 + j_2 - g_2 v_2)\ .\end{cases} \tag{4.10}$$

Here indexes SA–AV, AV–HP, SA–AT, EP–AT, HP–VN, and EP–VN of the coupling coefficients K represent unidirectional coupling between the corresponding blocks - pacemakers, muscles, and ectopic (EP) beat sources, $x_i^{\tau_n} \equiv x_i(t - \tau_n)$ are the components of the time delayed signal, and τ_n are the corresponding time delays. The set of equations for the external ectopic beats [x_4 and x_5 in (4.9) and (4.10)] is similar to (4.6).

The parameters for (4.6) – (4.10) are given in Tables 4.2 and 4.3 and were selected to obtain natural oscillation periods of uncoupled oscillators of 60 bpm, 40 bpm, and 20 bpm for SA, AV, and HP, respectively, and with shapes close to experimental data on action potentials of real pacemakers.

Following the general idea of [126], we, however, calculate total synthetic ECG signal in a different way - as a composition of the AT and VN signals:

$$ECG = m_0 + m_{\text{AT}} z_1 + m_{\text{VN}} z_2\,. \tag{4.11}$$

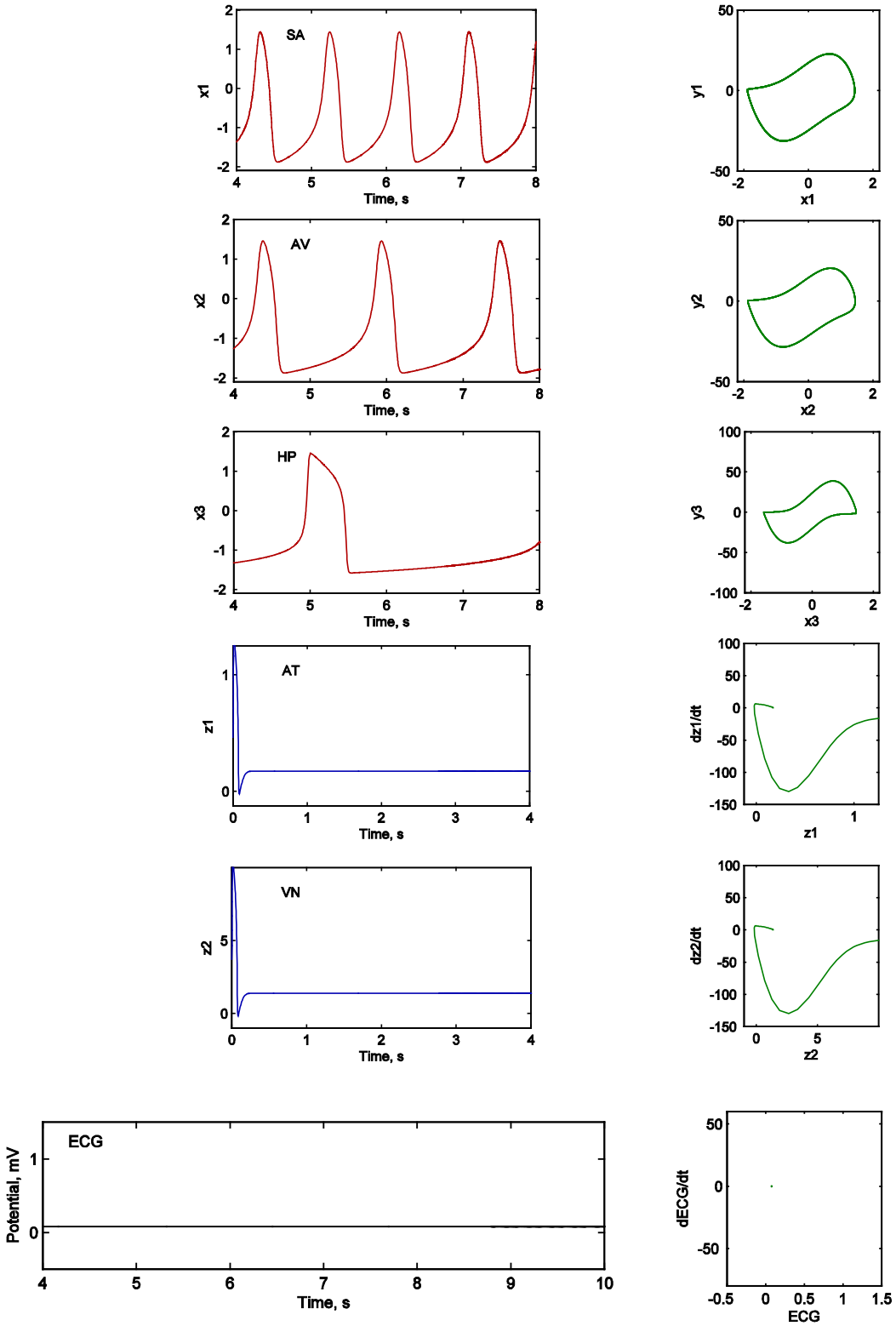

Figure 4.4: Calculated action potentials and obtained ECG (left), and their phase portraits (right) for uncoupled oscillators.

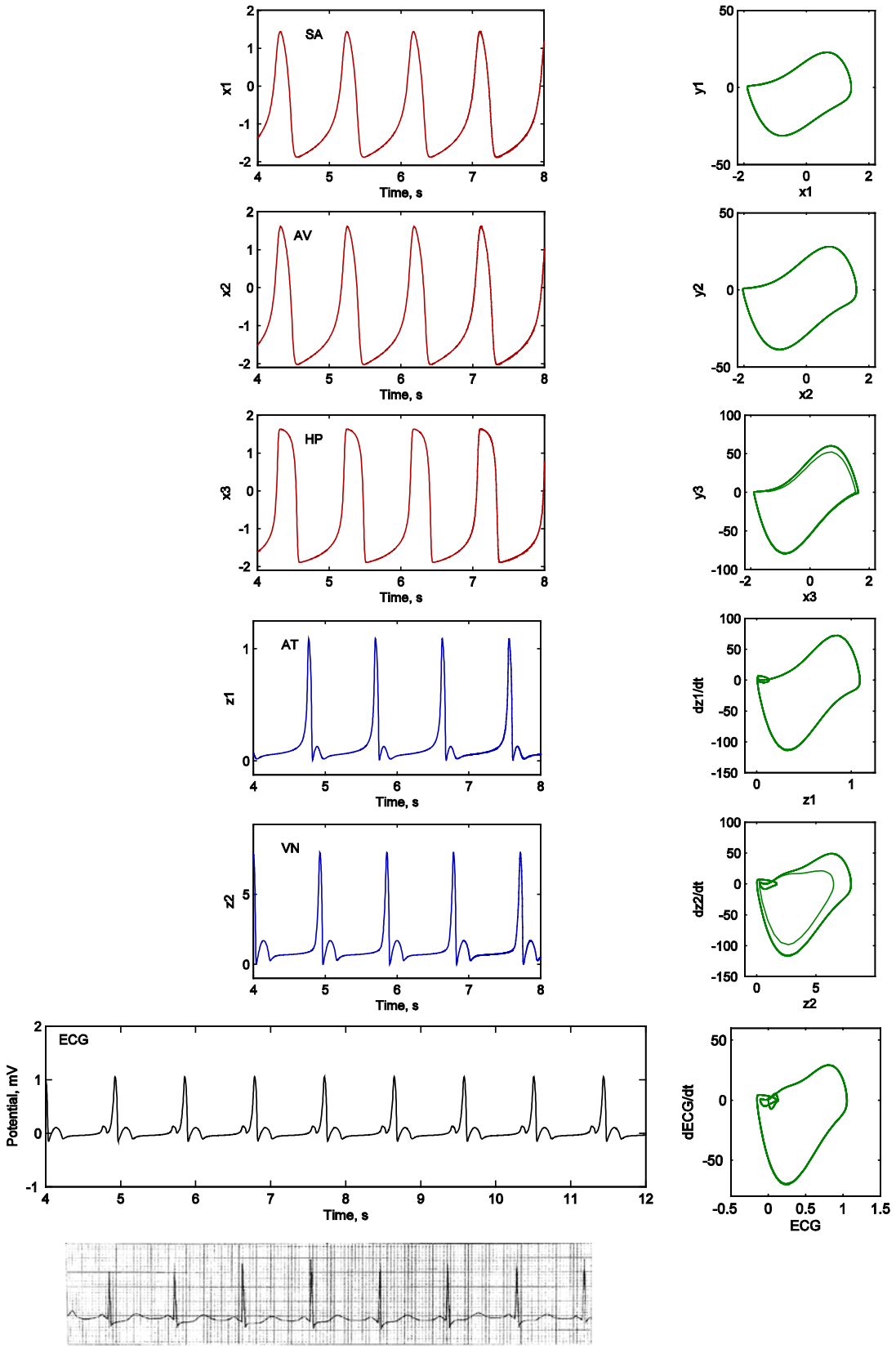

Figure 4.5: Calculated action potentials and obtained and real ECG (left), and their phase portraits (right) for for normal sinus rhythm.

.

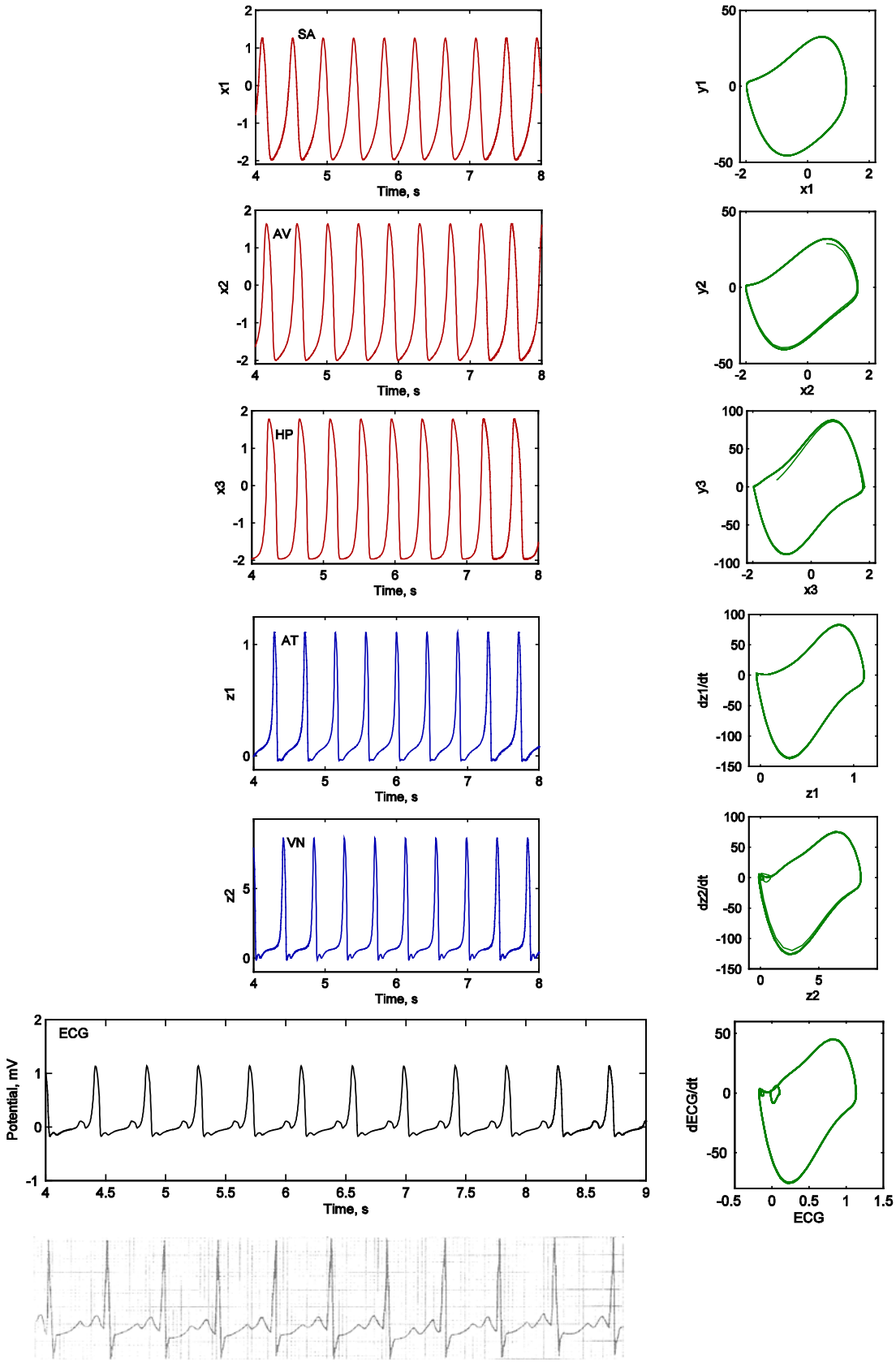

Figure 4.6: Calculated action potentials and obtained and real ECG (left), and their phase portraits (right) for sinus tachycardia 140 bpm.

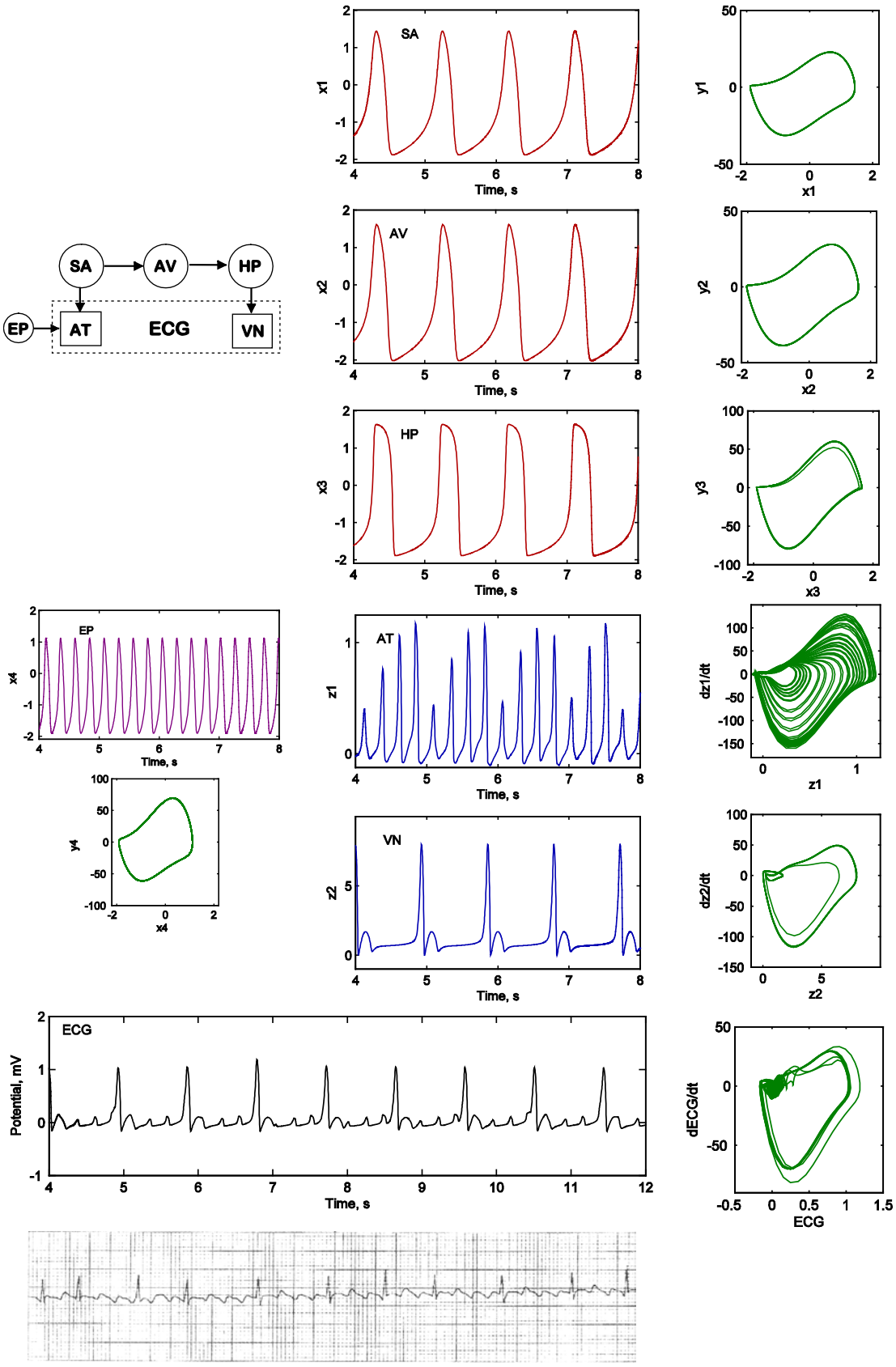

Figure 4.7: Atrial flutter. Heart model structure, calculated action potentials, synthetic ECG with EP applied to AT, real ECG, and the phase portraits.

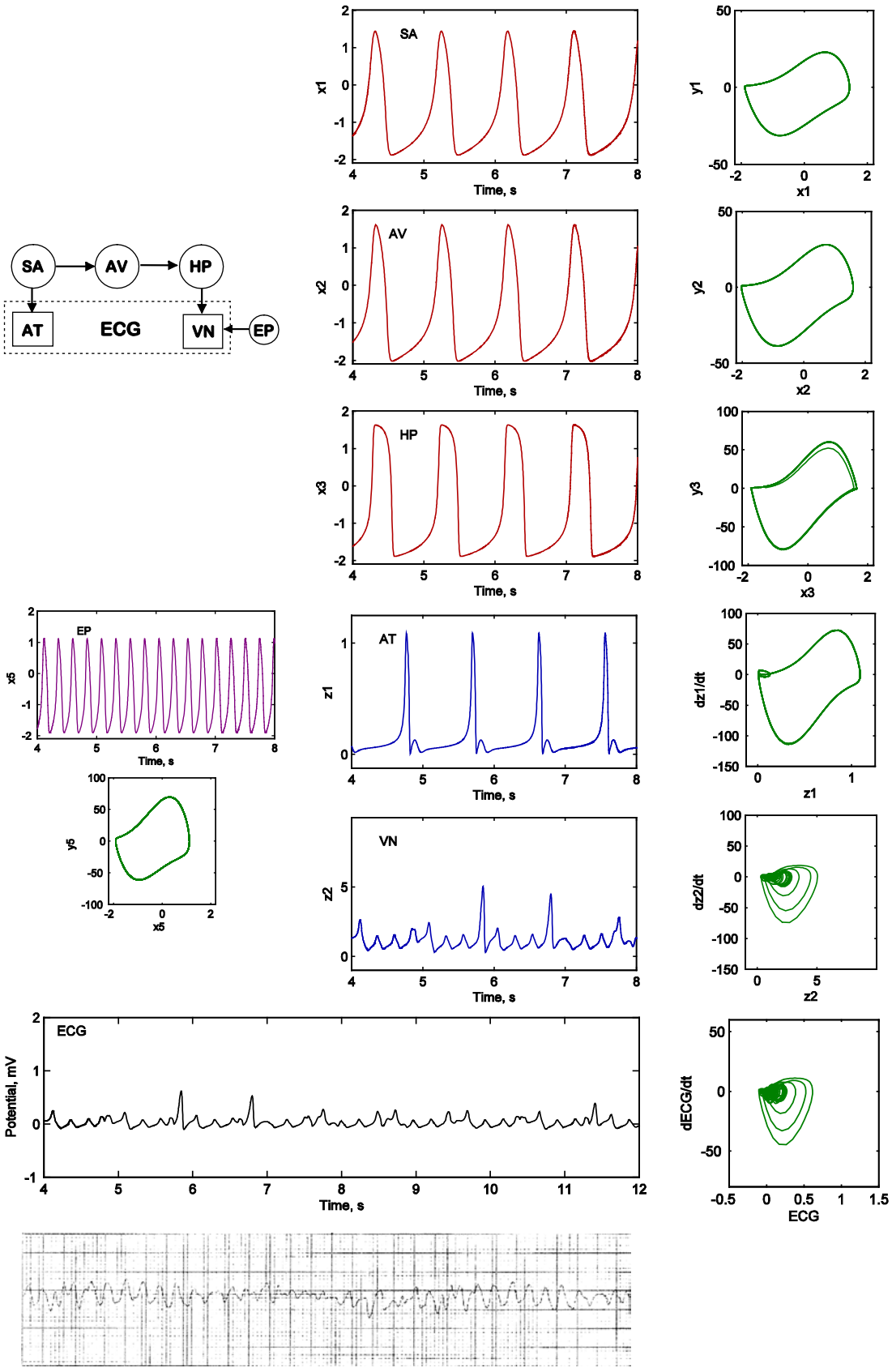

Figure 4.8: Ventricular fibrillation. Heart model structure, calculated action potentials, synthetic ECG with EP applied to VN, real ECG and the phase portraits.

Here, we adjusted the parameter m_0 to provide zero baseline of the synthetic ECG signal, and used the ratio $m_{VN}/m_{AT} = 8$ to represent realistic relation of P and QRS/T wave amplitudes.

Numerical simulations with the proposed model were performed in MATLAB environment employing DDE23 function [141, 142] for calculations of the delayed differential equations.

4.3 Simulation results

Figures 4.4 – 4.8 demonstrate calculated synthetic ECG waveforms and their comparison with real human ECG records [143] preceded by the block schemes of the oscillator system for each abnormal case.

Calculated normal synthetic ECG (Fig. 4.5) qualitatively reproduces the general characteristics of the real ECG, presenting regular sinus rhythm at 60 bpm and all main characteristic waveforms: P wave, QRS complex, and T wave.

Ventricular tachycardia in general can be described as regular (presented in this simulation) or irregular rapid rate of heartbeats higher than 100 bpm. Figure 4.6 demonstrates synthetic ECG with fast sinus rhythm at 140 bpm (tachycardia) calculated with appropriate parameters of SA oscillator and its comparison with real ECG. The system dynamics may be better understood observing phase portraits. The phase portraits of the normal ECG and sinus tachycardia are essentially periodic.

The ECG signals obtained after application of additional EP to AT and VN are shown in Figs. 4.7 and 4.8, respectively.

Re-entrant arrhythmias take place when an electrical signal (produced, for example, by EP) recurrently moves in a pathological circle within the heart, instead of conducting from one part of the heart to the other and then stopping for relaxation.

We simulated two such cardiac disorders - atrial flutter and ventricular fibrillation adding accessory oscillators (EP) with frequency (about 200 bpm in our simulation) higher than normal intrinsic frequency of SA (60 bpm).

During atrial flutter, AT depolarize in a fast circular movement caused by re-entry, and contract typically at around 300 bpm, resulting in a rapid sequence of small P waves on the ECG. For AV this rhythm is too fast to be able to conduct the signal to

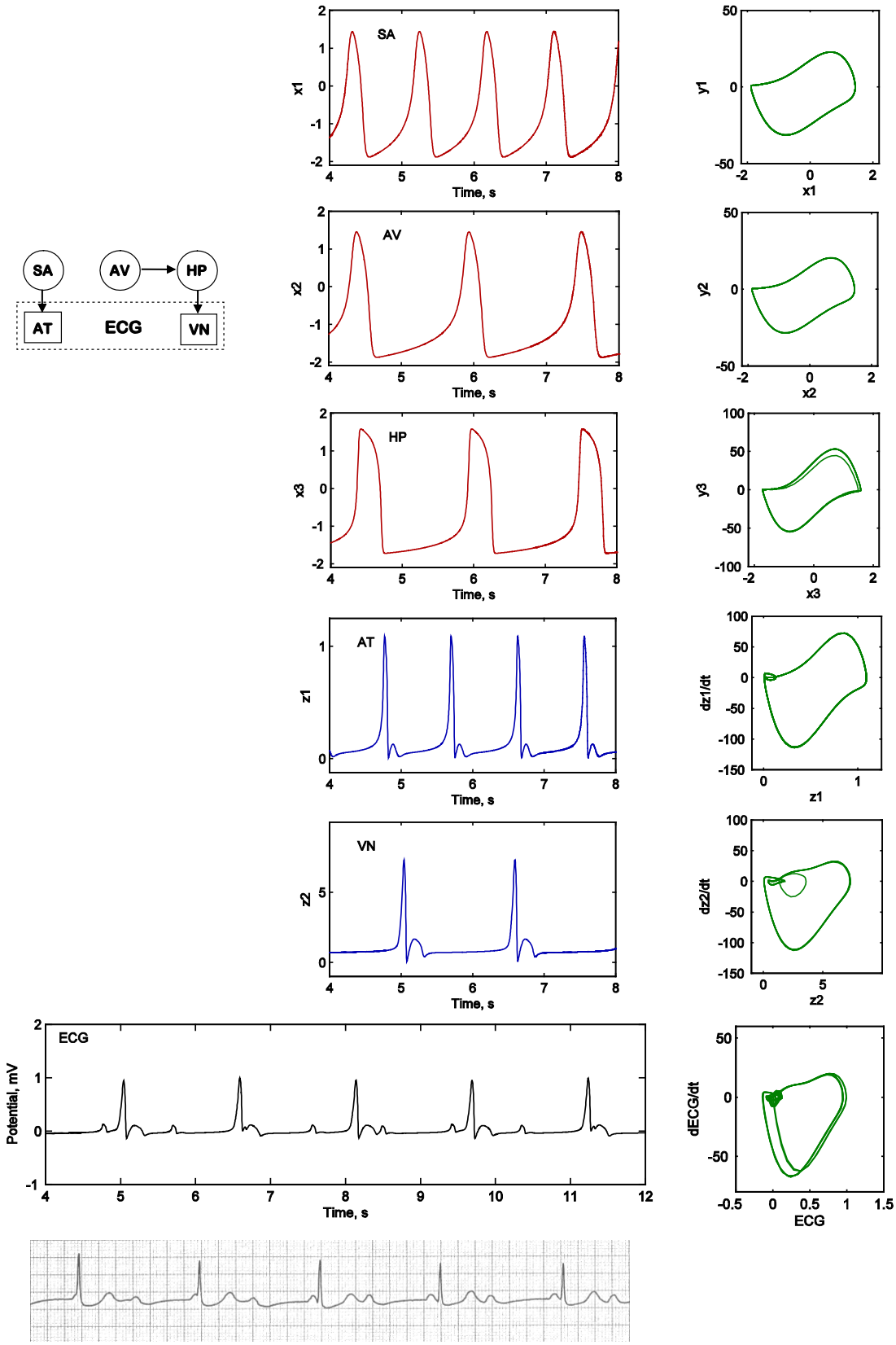

Figure 4.9: Block between SA and AV. Heart model structure, calculated action potentials, synthetic and real ECG and the phase portraits.

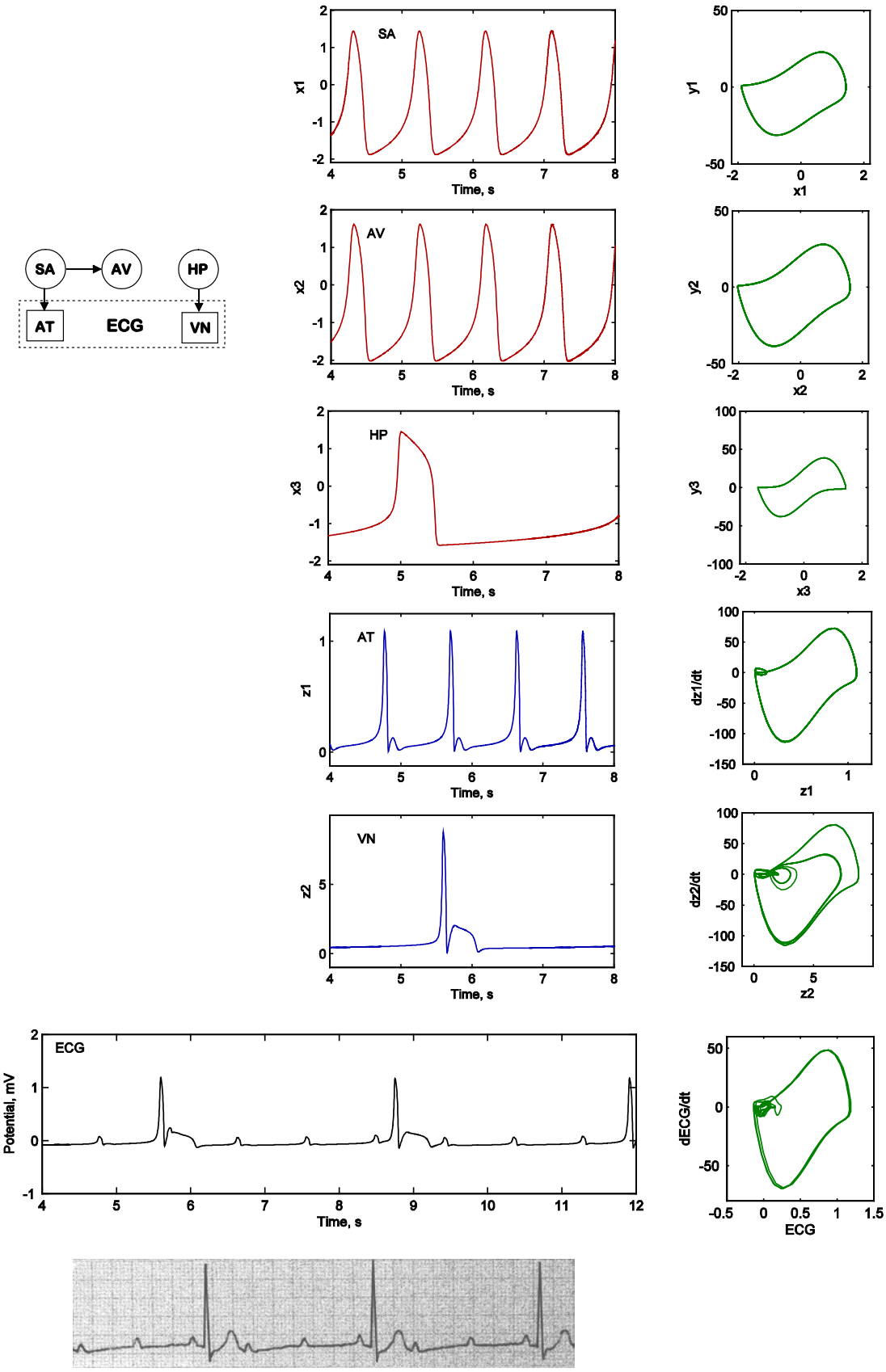

Figure 4.10: Block between AV and HP. Heart model structure, calculated action potentials, synthetic and real ECG, and the phase portraits.

VN, so typically there is a 2:1, 3:1 or 4:1 block, resulting in a ventricular frequency of 150, 100 or 75 bpm respectively. We obtained synthetic ECG with typical signs of atrial flutter with 3:1 AV block and small P waves as shown on Fig. 4.7. The presented phase portraits confirm its irregular characteristic.

Ventricular fibrillation is chaotic disorganized firing of impulses from VT. Figure 4.8 demonstrates ventricular fibrillation obtained applying EP signal with 200 bpm to VN. The irregular characteristic of this kind of behavior is noticeable since the response is not related to a closed curve on the phase portrait.

The irregularity of atrial flutter and ventricular fibrillation suggests a chaotic-like response that, however, should be assured by some system invariant as the Lyapunov exponent.

In order to simulate some other cardiac disorders, which can be identified on ECG, we considered different coupling blocks between the nodes of the oscillator model. The cases with broken connections between the SA-AV and AV-HP were simulated by blocking the coupling between corresponding oscillators. Under such conditions, VN oscillator was driven by the signal with a slower intrinsic frequencies corresponding to either AV 40 bpm (Fig. 4.9), or HP 20 bpm (Fig. 4.10), respectively, in comparison with the normal ECG rate. This disorder is called the complete block of the electrical conduction on the pathway from SA to VN, resulting in asynchronous AT and VN contraction. This kind of pathology has a regular behavior as can be observed in the phase portraits.

4.4 Limitations

In the mode described above both activation (depolarization) and recovery (repolarization) of cardiac muscles are presented by one FHN oscillator for atria and ventricles. However, in real heart, depolarization and repolarization take place separately and some normal and pathological conditions may affect on one of these processes solely.

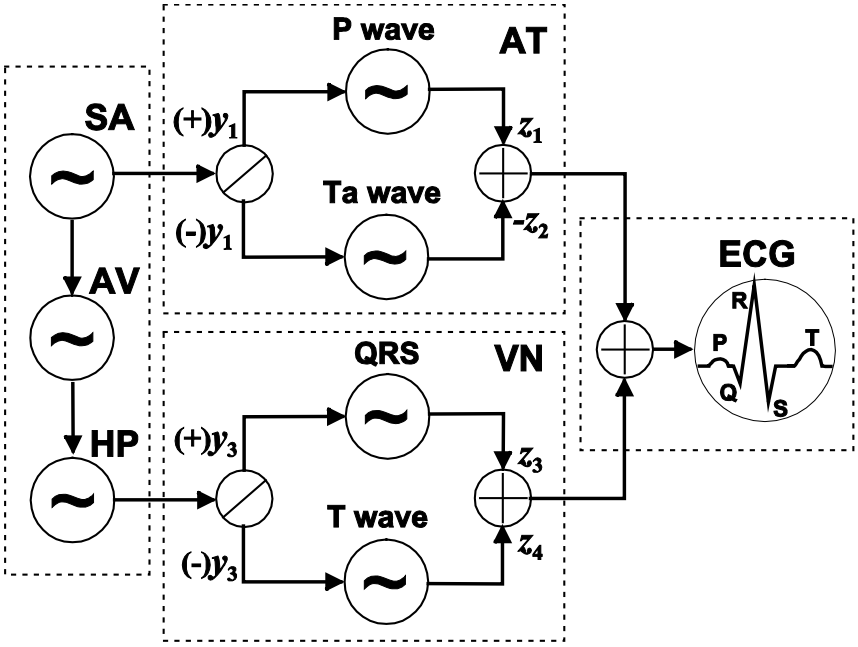

Figure 4.11: General scheme of the improved cardiac conduction system model.

4.5 Improvement of the oscillator model

To eliminate drawbacks mentioned above, we further developed our model with inclusion of a description for depolarization and repolarization waves in the atria and ventricles utilizing separate modified FHN systems for each of the processes, which allows generating physiologically correct ECG signals (Fig 4.11).

In the previous paragraph, all oscillators (4.6) − (4.10) were coupled with position-only coupling ($x_i - x_{i-1}$). Performing a number of simulations on a system with position-variable coupling added to the right-hand side of the second equation of (4.4) similar to the three cardiac oscillator system (SA–AV–HP) described in Ref. [126], we found that synchronization level is not enough in wide range of beat rates (30–200 bpm). In particular, the synchronization problem occurred at very high sinus rates (>140 bpm) in the HP oscillator node, which has the lowest intrinsic rate (35 bpm). The application of the velocity coupling to the right-hand side of the second equation significantly improved in-phase synchronization at such high rates [137]. Moreover, it is also known that the synchronization level depends on the coupling coefficients K as well [122].

Table 4.4: Table of parameters used in equations (4.12) – (4.14) for normal sinus rhythm.

α_1	Damping coefficients for pacemakers	40
α_2		50
α_3		50
f_1	Parameters defining the amplitude of a pulse	22.0
f_2		8.4
f_3		1.5
d_1	Parameters changing the rest state and dynamics	3.0
d_2		3.0
d_3		3.0
e_1	Parameters controlling the hyperpolarization of the excitation variable	3.5
e_2		5.0
e_3		12.0
u_{11}	Parameters controling excitation threshold	0.83
u_{21}		0.83
u_{31}		0.83
u_{12}	Parameters controling excited state	-0.83
u_{22}		-0.83
u_{32}		-0.83

Taking into account the above-mentioned considerations, in our proposed mathematical model we describe all three natural pacemakers by a system of modified asymmetric VDP equations with unidirectional time-delay velocity coupling only:

$$\text{SN}\begin{cases}\dot{x}_1 = y_1 \\ \dot{y}_1 = -\alpha_1 y_1 (x_1 - u_{11})(x_1 - u_{12}) - f_1 x_1 (x_1 + d_1)(x_1 + e_1)\,,\end{cases} \tag{4.12}$$

$$\text{AV}\begin{cases}\dot{x}_2 = y_2 \\ \dot{y}_2 = -\alpha_2 y_2 (x_2 - u_{21})(x_2 - u_{22}) - f_2 x_2 (x_2 + d_2)(x_2 + e_2) \\ \qquad + K_{\text{SA-AV}} (y_1^{\tau_{\text{SA-AV}}} - y_2)\,,\end{cases} \tag{4.13}$$

$$\text{HP}\begin{cases}\dot{x}_3 = y_3 \\ \dot{y}_3 = -\alpha_3 y_3 (x_3 - u_{31})(x_3 - u_{32}) - f_3 x_3 (x_3 + d_3)(x_3 + e_3) \\ \qquad + K_{\text{AV-HP}} (y_2^{\tau_{\text{AV-HP}}} - y_3)\,.\end{cases} \tag{4.14}$$

Here $y_i^{\tau_n} \equiv y_i(t - \tau_n)$ are the velocity coupling components of the time delayed signal, and τ_n are the corresponding time delays. The parameters α_i, d_i, e_i, f_i, and u_i for

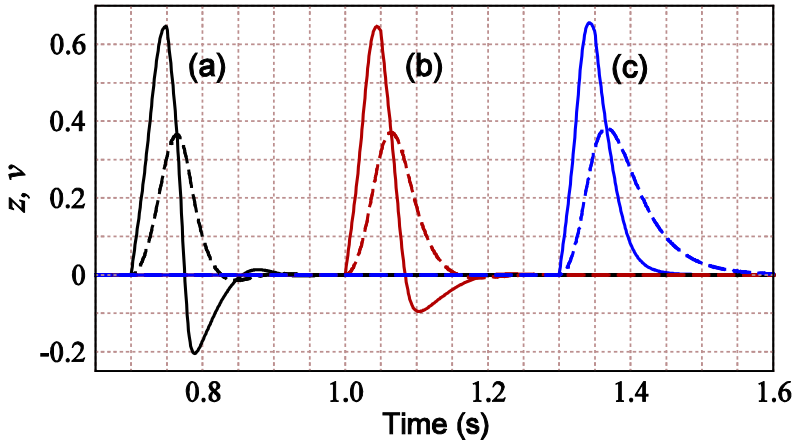

Figure 4.12: Response of the unmodified (a) and modified (b and c) FitzHugh–Nagumo systems on instantaneous stimulating current pulse. Solid and dashed curves correspond to the potential z and the recovery variable v, respectively.

(4.12) – (4.14) were selected to obtain intrinsic oscillation rates of 70 bpm, 50 bpm, and 35 bpm for uncoupled SA, AV, and HP oscillators, respectively, and with shapes close to experimental data on action potentials of real pacemakers [144-146] and are given in Table 4.4. We found that to maintain stable synchronization between the oscillators with change of the SA rate, the coupling coefficients should be proportional to $\omega_1^2 \sim f_1$, thus for simplicity we set $K_{\text{SA–AV}} = K_{\text{AV–HP}} = f_1$.

The standard FHN system (4.5) produces hyperpolarization of z – its value becomes negative at the beginning of the refractory period [see Fig. 4.12(a)], which is undesirable for many applications of the model. Rogers *et al*. [147] proposed to eliminate the hyperpolarization by replacing the term bv in the first equation to bvz (thus, adding the nullcline $z = 0$ to the phase plane) as shown in Fig. 4.12(c). However, in our case the undershoot of z can be useful for representation of the S wave in the QRS complex. To control the negative excursion of z we use both original and modified terms in the right side of the first equation of (4.5):

$$\begin{aligned} \dot{z} &= -cz(z - w_1)(z - w_2) - bv - dvz + I \\ \dot{v} &= h(z - gv). \end{aligned} \tag{4.12}$$

The examples of the resulting waveforms for three sets of parameters are shown in Fig. 4.12. Curve (a) corresponds to unmodified FHN system – $b = 174$, $d = 0$, curve (b) – to the modified system with $b = 105$, $d = 45$, and curve (c) – to the modified

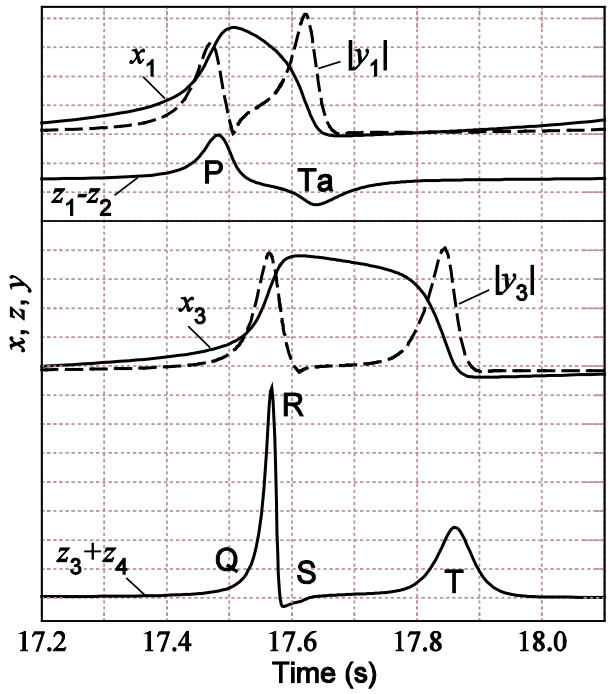

Figure 4.13: Coupling between pacemakers and muscles. Calculated action potentials (x_i), absolute value of their derivatives (y_i), and muscle response (z_i) for sinoatrial pacemaker and atrium muscle (top panel), and His–Purkinje pacemaker and ventricular muscle (bottom panel).

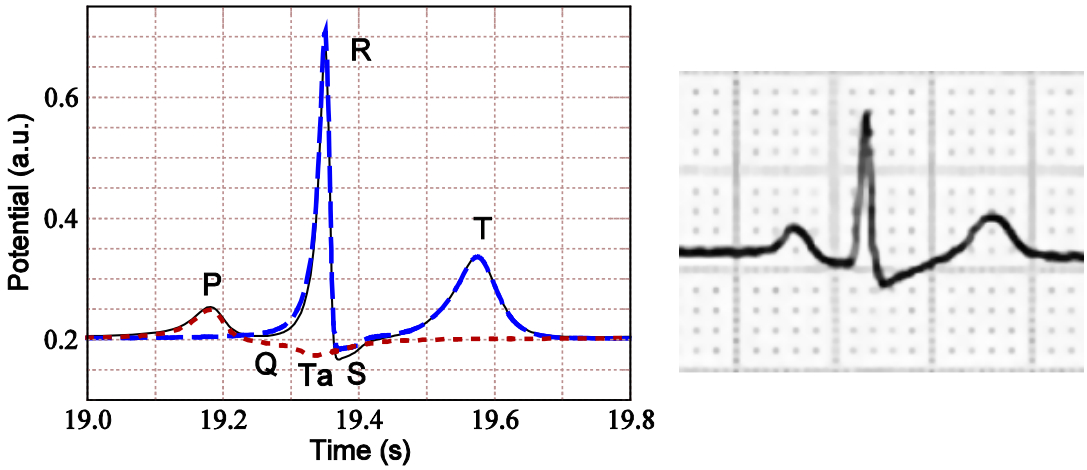

Figure 4.14: Calculated atrial (dotted line), ventricular (dashed line), and net ECG (solid line) waveforms for normal case (left) and clinical ECG lead II [148] (right).

system with $b = 0$ and $d = 105$. The latter corresponds to the modification proposed in [147]. Other parameters for Fig. 4.12 are as follows: $c = 300$, $w_1 = 0.12$, $w_2 = 0.8$, $h = 24$, $g = 1$, and the amplitude of the instantaneous current pulse $I(t) = I_0\delta(t)$ was $I_0 = 15$.

Table 4.5: Table of parameters used in equations (4.13) – (4.20) for normal sinus rhythm.

k_1	Scaling coefficients	$2x10^3$
k_2		$4x10^2$
k_3		10^4
k_4		$2x10^3$
c_1	Parameters defining the amplitude of a pulse	0.26
c_2		0.26
c_3		0.12
c_4		0.1
b_1	Parameters changing the rest state and dynamics	0.0
b_2		0.0
b_3		0.015
b_4		0.0
d_1	Parameters controlling the hyperpolarization of the excitation variable	0.4
d_2		0.4
d_3		0.09
d_4		0.1
h_1	Parameter representing excitability and controling the abruptness of activation and the duration of the action potential	0.004
h_2		0.004
h_3		0.008
h_4		0.008
g_1	Parameters changing the rest state and dynamics	1.0
g_2		1.0
g_3		1.0
g_4		1.0
w_{11}	Parameters controling excitation threshold	0.13
w_{21}		0.19
w_{31}		0.12
w_{41}		0.22
w_{12}	Parameters controling excited state	1.0
w_{22}		1.0
w_{32}		1.1
w_{42}		0.8
$K_{AT_{DE}}$	Coupling coefficient for P wave	$4x10^{-5}$
$K_{AT_{RE}}$	Coupling coefficient for Ta wave	$4x10^{-5}$
$K_{VN_{DE}}$	Coupling coefficient for QRS complex	$9x10^{-5}$
$K_{VN_{RE}}$	Coupling coefficient for T wave	$6x10^{-5}$

Using the proposed quiescent excitable FHN model (4.12) we describe the depolarization and repolarization processes in cardiac muscles as a system of four sets of ordinary differential equations:

$$\text{P wave}\begin{cases}\dot{z}_1 = k_1(-c_1 z_1(z_1 - w_{11})(z_1 - w_{12}) - b_1 v_1 - d_1 v_1 z_1 + I_{\mathrm{AT_{DE}}}) \\ \dot{v}_1 = k_1 h_1(z_1 - g_1 v_1), \end{cases} \tag{4.13}$$

$$\text{Ta wave}\begin{cases}\dot{z}_2 = k_2(-c_2 z_2(z_2 - w_{21})(z_2 - w_{22}) - b_2 v_2 - d_2 v_2 z_2 + I_{\mathrm{AT}_{RE}}) \\ \dot{v}_2 = k_2 h_2(z_2 - g_2 v_2), \end{cases} \tag{4.14}$$

for AT muscles and

$$\text{QRS}\begin{cases}\dot{z}_3 = k_3(-c_3 z_3(z_3 - w_{31})(z_3 - w_{32}) - b_3 v_3 - d_3 v_3 z_3 + I_{\mathrm{VN}_{DE}}) \\ \dot{v}_3 = k_3 h_3(z_3 - g_3 v_3), \end{cases} \tag{4.15}$$

$$\text{T wave}\begin{cases}\dot{z}_4 = k_4(-c_4 z_4(z_4 - w_{41})(z_4 - w_{42}) - b_4 v_4 - d_4 v_4 z_4 + I_{\mathrm{VN}_{RE}}) \\ \dot{v}_4 = k_4 h_4(z_4 - g_4 v_4), \end{cases} \tag{4.16}$$

for VN muscles, respectively. The values of the parameters for Eqs. (4.13) – (4.16) are given in Table 4.5. We selected the parameter values in such a way to obtain pronounced difference between relatively fast depolarization (high and narrow P and R waves) and slow repolarization (low and wide Ta and T waves) processes.

The stimulation impulses of the transmembrane ionic currents *I* represent the couplings between the SA and HP pacemakers and AT and VN muscles, respectively, provided by corresponding current pulses (Fig. 4.11). For the latter we use absolute values of y_1 and y_3 (see Fig. 4.13), and calculate amplitudes of the stimulation current pulses as follows:

$$\mathrm{I}_{\mathrm{AT_{DE}}}\begin{cases}0, & \text{for } y_1 \le 0 \\ K_{\mathrm{AT_{DE}}} y_1, & \text{for } y_1 > 0 \end{cases} \tag{4.17}$$

$$\mathrm{I}_{\mathrm{AT_{RE}}}\begin{cases}-K_{\mathrm{AT_{RE}}} y_1, & \text{for } y_1 \le 0 \\ 0, & \text{for } y_1 > 0 \end{cases} \tag{4.18}$$

$$\mathrm{I}_{\mathrm{VN_{DE}}}\begin{cases}0, & \text{for } y_3 \le 0 \\ K_{\mathrm{VN_{DE}}} y_3, & \text{for } y_3 > 0 \end{cases} \tag{4.19}$$

$$\mathrm{I}_{\mathrm{VN_{RE}}} \begin{cases} -K_{\mathrm{VN_{RE}}} y_3, & \text{for } y_3 \le 0 \\ 0, & \text{for } y_3 > 0 \ . \end{cases} \tag{4.20}$$

The total synthetic ECG waveform is calculated as a composition of the signals from AT and VN muscles (see Figs. 4.13 and 4.14):

$$ECG = z_0 + z_1 - z_2 + z_3 + z_4 \, . \tag{4.21}$$

Here, we adjusted the parameter $z_0 = 0.2$ to provide zero baseline of the ECG signal. The value of z_2, which corresponds to atrial Ta wave, is added with negative sign due to the fact that it is known to be opposite to P wave [149]. Numerical simulations with the proposed model were performed in MATLAB environment employing DDE23 function [141, 142] for calculation of the delay differential equations. The DDE23 solver makes the solution of wide range of delay differential equations as easy as possible in many research areas, for example, in computational pharmacokinetics [150].

Since standard DDE23 function does not allow direct utilization of time-delay derivatives, we obtain them for Eqs. (4.13) and (4.14) in the following way:

$$y^{\tau} = \frac{x^{\tau_a} - x^{\tau_b}}{\tau_b - \tau_a} = \frac{x(t-\tau_a) - x(t-\tau_b)}{\tau_b - \tau_a}, \tag{4.22}$$

where $\tau =$ is the desirable delay and $\tau_b - \tau_a = 0.05\,\mathrm{s}$.

We approximated the dependence of the total delay between coupled SA and HP nodes on the parameter f_1 as

$$\tau_{\mathrm{SA\text{-}HP}} = \tau_{\mathrm{SA\text{-}AV}} + \tau_{\mathrm{AV\text{-}HP}} = 2.29 / f_1 + 0.08. \tag{4.23}$$

Such dependence allows keeping the ratio of P–R and R–T intervals in physiologically correct range [149]. For simplicity, in all simulations performed in this paragraph we set up equal delays of $\tau_{\mathrm{SA-HP}} / 2$ in both SA–AV and AV–HP conduction pathways without any effect to the resulting ECG. Thus, for normal rhythm of 70 bpm we have $\tau_{\mathrm{SA-AV}} = \tau_{\mathrm{AV-HP}} = 0.092\,\mathrm{s}$.

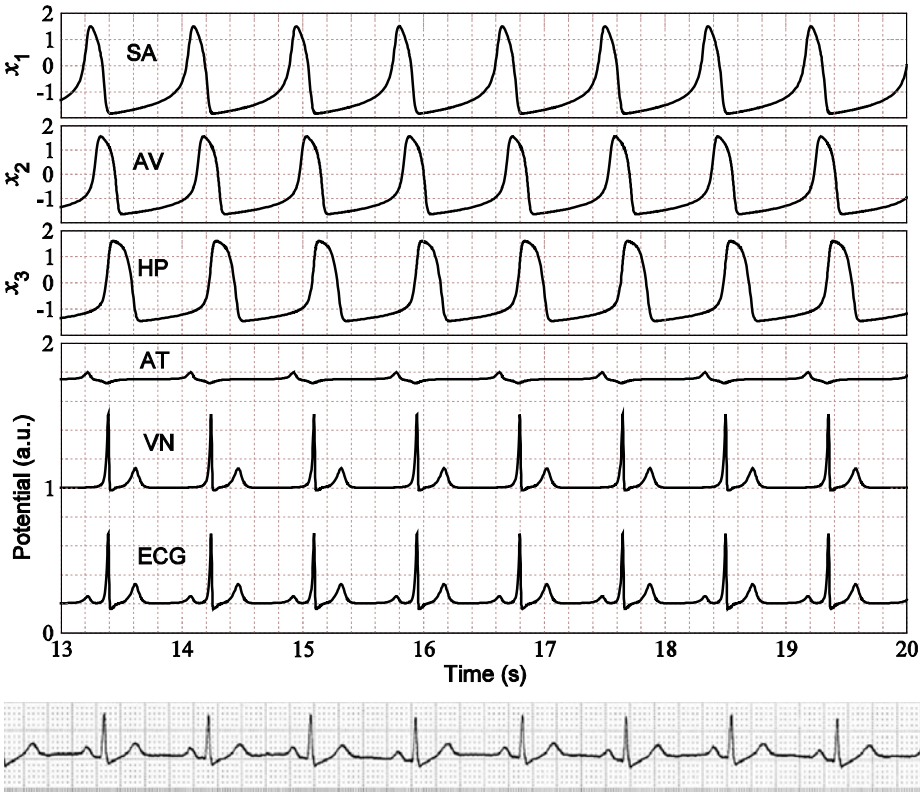

Figure 4.15: Calculated action potentials, muscle response and ECG at 70 bpm (normal case) and real patient's ECG [148].

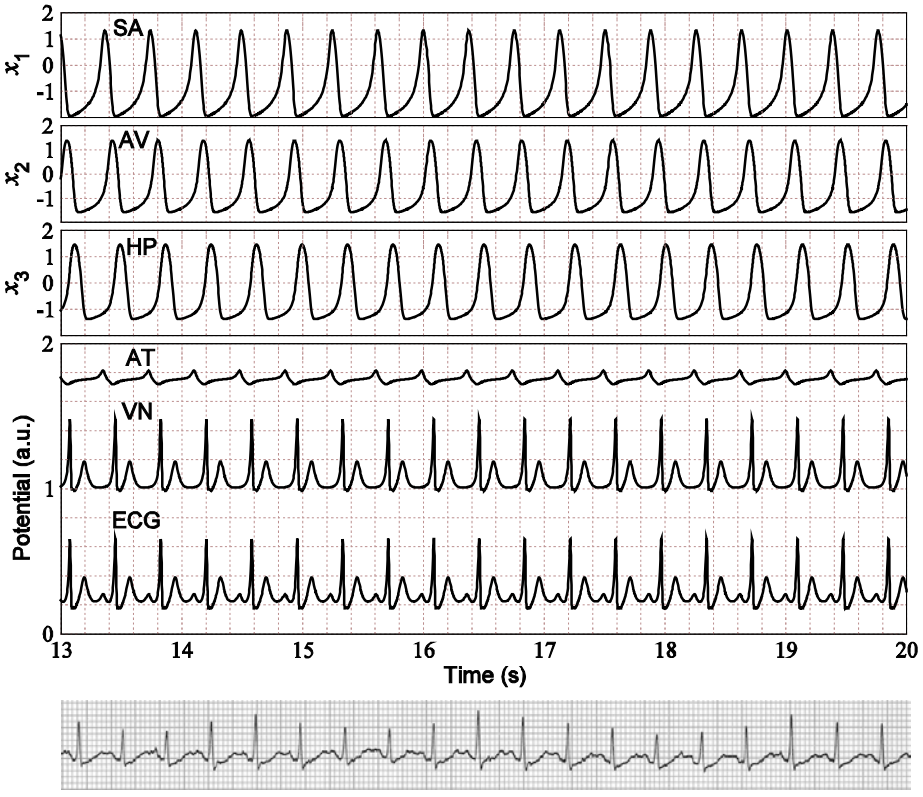

Figure 4.16: Calculated action potentials, muscle response and ECG at 160 bpm (tachycardia) and real patient's ECG [8].

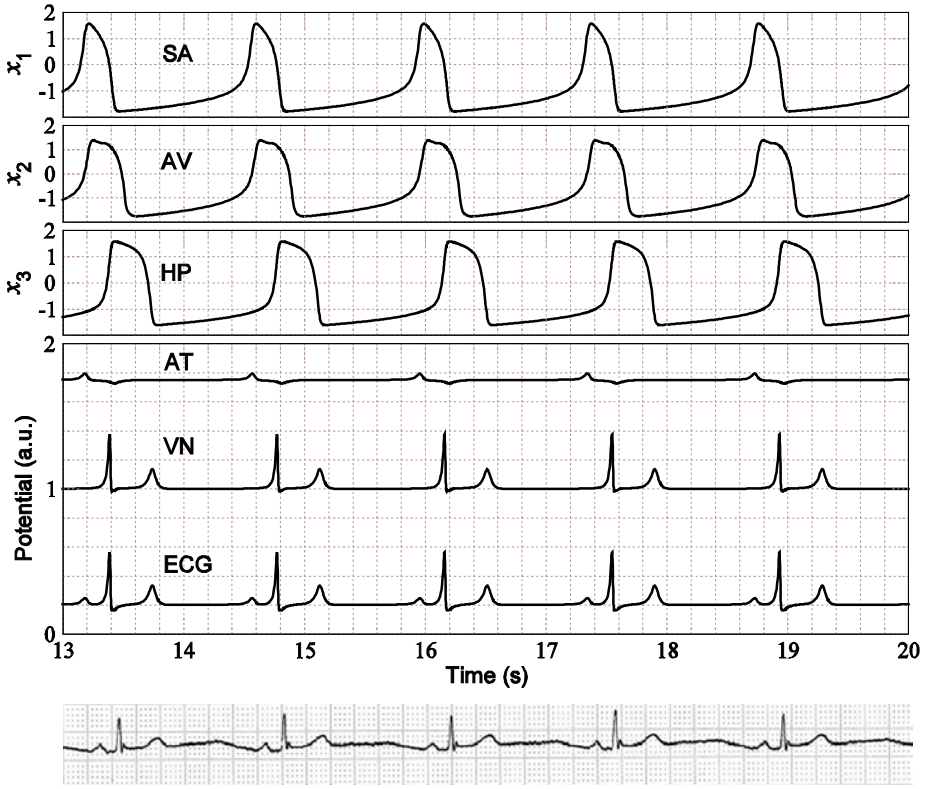

Figure 4.17: Calculated action potentials, muscle response and ECG at 43 bpm (bradycardia) and real patient's ECG [148].

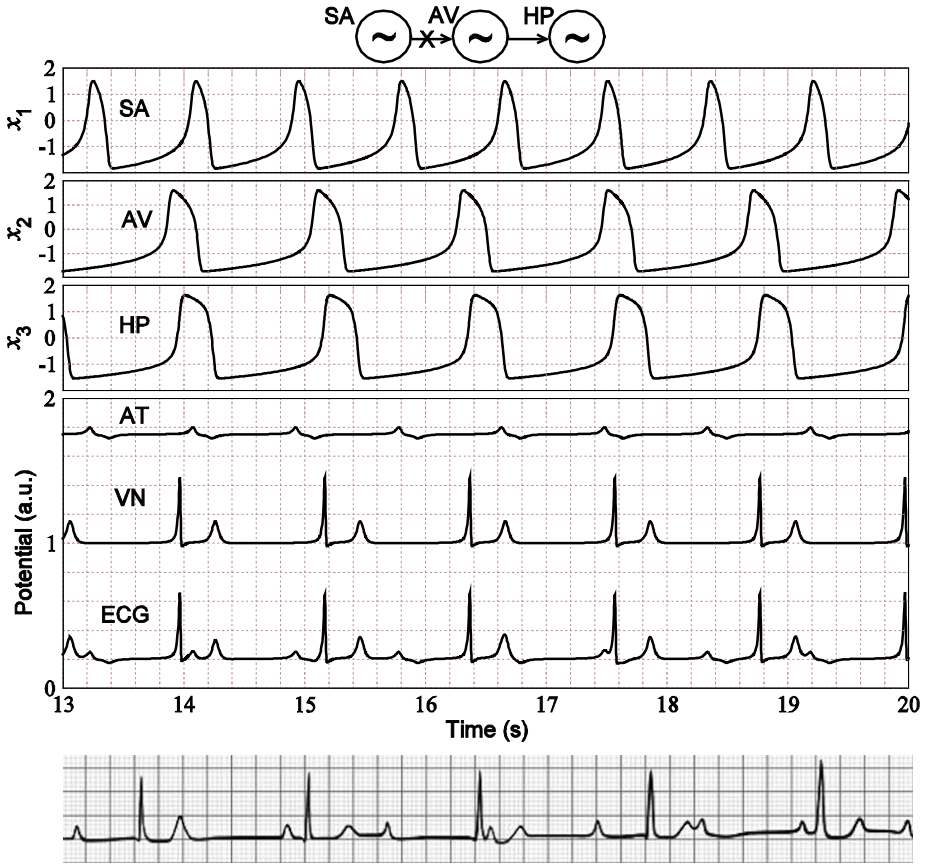

Figure 4.18: Calculated action potentials, muscle response and ECG at complete SA–AV block and real patient's ECG [8].

4.6 Simulation results with the improved model

To validate the proposed model, we performed a number of numerical simulations with different normal and pathological rhythms, shown in Figs. 4.15 – 4.17. The figures demonstrate calculated action potentials of SA, AV, and HP pacemakers, corresponding responses from AT and VN muscles, and resulting total ECG waveforms. The latter are presented in comparison with real patient's ECG (standard Einthoven lead II) [8, 148]. For the normal case (see Fig. 4.15), all pacemakers are dominated by SA node and follow its rhythm of 70 bpm ($f_1 = 22$). The atrial and ventricular muscles are operating consequentially, so the positive P wave precedes the QRS complex, followed by the positive T wave, while the Ta wave is merged with the QRS complex. After getting normal ECG as a reference, we tested our model by reproducing several well-known rhythm disorders. We started with sinus tachycardia, the fast rhythm when SA node generates impulses greater than 100 bpm (in our case 160 bpm with $f_1 = 87$) with other pacemakers synchronously following this rate (Fig. 4.16). The rhythm is regular, but action potentials of all pacemakers became shorter with the rate increase, and correspondingly P–Ta and R–T intervals became shorter as well. At such very fast rates the distance between the T and P waves of subsequent beats gets smaller, and these waves may even merge with each other. Many factors may cause the sinus tachycardia, it occurs most often as a physiological response to physical exercises, stress, fever, or may also result from congestive heart failure. Sinus bradycardia is slow sinus rhythm less than 60 bpm, and occurs naturally during sleep. It is normal in children and athletes or may be a consequence of increased parasympathetic or vagal tone. Figure 4.17 demonstrates the simulation results obtained at 43 bpm ($f_1 = 13$). The regular rhythms also translated with same shape and rate from SA to AV and HP. It is seen on the obtained ECG that the P–Ta and R–T intervals are increased. However, with decreasing rate pacemaker's action potential duration increases, the ratio between it and diastolic interval becomes smaller, as it seen from Figs. 4.15 – 4.17. In the next computer experiments, we studied interactions among different parts of the heart, completely broken coupling between pacemakers.

Figure 4.18 presents the result of simulation of complete SA–AV block at SA regular rhythm of 70 bpm. The SA action potential shapes and durations are normal,

Figure 4.19: Calculated action potentials, muscle response and ECG at complete AV–HP block and real patient's ECG [8].

and P and Ta waves are normal accordingly. The AV node fires at its own rate of 50 bpm and the HP node synchronously follows the AV action potentials. In this case, atrial muscle operates at the rate of 70 bpm, while ventricles beat at slower rate of 50 bpm. The obtained ECG reflects this disturbance as atrial P and Ta waves and QRS complexes and T waves are unrelated in time. Complete block between AV and HP pacemakers (Fig. 4.19) leads to independent operation of HP node at its own rate of 30 bpm with expanded action potentials, while normally coupled SA and AV nodes are beating at 70 bpm and their action potentials correspond to the normal case. Thus, we get independent normal action of atria and slow rate of ventricles. In Figs. 4.18 and 4.19 one can observe the asynchrony of atrial and ventricular depolarization/repolarization processes represented by independent appearance of P and unmasked Ta waves on the one hand, and QRS complex and T wave on the other hand [149]. In all cases demonstrated in Figs. 4.15 – 4.19 we observe good conformity of simulated synthetic ECG with the presented clinical data. Figure 4.20 shows dependence of the obtained major ECG intervals on parameter f_1, which

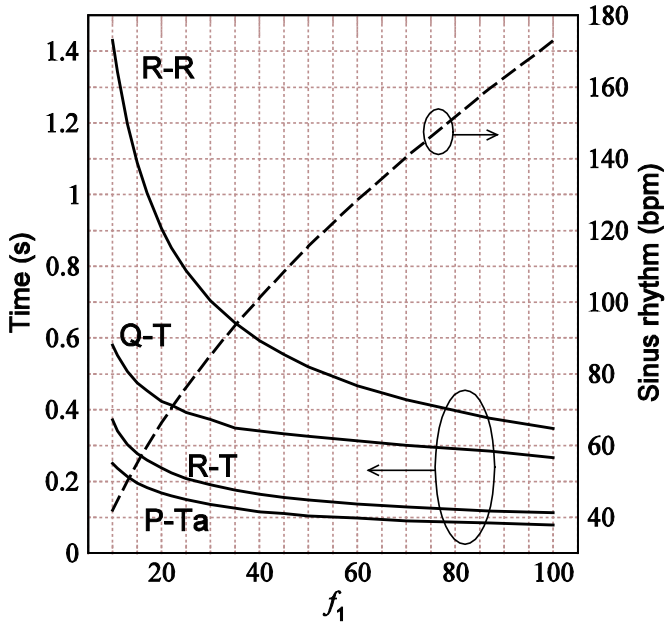

Figure 4.20: Dependences of R–R, Q–T, R–T, and P–Ta intervals (solid lines) and sinus rhythm (dashed line) on the parameter f_1.

controls intrinsic frequency of the main oscillator. The R–R interval is the time between peaks of the neighboring R waves and related to heart rate. The Q–T interval is measured from the beginning of QRS complex to the end of T wave and represents the total duration of ventricular depolarization. For the rate of 70 bpm (f_1 = 22) we obtained the value of 0.41 s, which lays in the normal physiological range (0.3–0.45 s). Both the R–R and the Q–T intervals are usually used in clinical practice to analyze patient's ECG.

Two additional intervals R–T and P–Ta shown in Fig. 4.20 were measured between corresponding peaks on the calculated ECG and represent the correlation between the depolarization and repolarization processes in atria and ventricles at different heart rates. All the calculated intervals are inversely proportional to the parameter f_1 in accordance with experimental findings. The calculated nonlinear dependence of sinus rhythm on f_1 is added for easy calculation of the former. We mentioned in the introduction that there are a limited number of similar models generating artificial ECG signals with sets of ordinary differential equations [113, 114, 126, 128]. In contrast to these models, we took into account macroscopic structure of cardiac conduction system and atrial and ventricular muscles. This allowed us to observe the interaction of the system elements such as different conduction blocks on the ECG (see Figs. 4.18 and 4.19). Using the proposed model with separate FHN systems for the description of depolarization and repolarization processes one can

study appearance of the Ta wave and its input to the net ECG signal in different situations. Implementation of the signal voltage derivative (transmembrane current) coupling between the SA and HP pacemakers and AT and VN muscles described by FHN type equations, respectively, allowed obtaining of realistic P–Ta and R–T intervals in the wide range of sinus rhythms (Fig. 4.20). Inclusion of additional factors affecting the regular sinus rhythm, such as heart rate variability phenomena (respiratory arrhythmia) and low-frequency oscillations associated with Mayer waves, similar to the work by McSharry *et al.* [112] can further improve feasibility of our model.

4.7 Effect of coupling on the pacemaker synchronization in coupled oscillator ECG model

4.7.1 Introduction

In the previous Sections (4.4 and 4.5), we considered only full synchronization regime of the oscillators operation with current coupling between pacemakers. Moreover, synchronization behavior at different mode-lock regimes in the oscillator model of cardiac conduction system still remains unclear, in particular, effect of employment of different coupling types and their combinations. The aim of the work in this Section is to investigate the effect of different configurations of diffusive voltage and current couplings between the natural pacemakers on their synchronization behavior and the appearance of incomplete heart blocks.

Synchronization in the interacting oscillator system determines its global behavior, and manifests as an adjustment of frequencies, which is not necessary, require complete temporal alignment of individual oscillator signals. Coupling between the oscillators plays very important role in providing proper synchronization behavior of pacemakers in wide range of heart rhythms. For description of biological systems, a diffusive coupling is the most commonly employed type. In general, for such systems the coupling term would consist of both “position” or “voltage” ($x_{i-1} - x_i$) and “velocity” or “current” ($y_{i-1} - y_i$) differences [136], while in many simpler cases only single variable coupling is frequently used [124, 126]. In the most of the nonlinear heart dynamics models a position coupling term is added to the

second equations for driven pacemakers (AV node and HP system), and in some cases to the first one [131]. We did not find in the literature cases with current coupling applied to the first equation of the system.

4.7.2 Simulation details

To study various heart blocks, for example, incomplete AV blocks with different P:QRS ratios, proper choice of the coupling form might be crucial. Thus, we find it important to investigate the influence of different coupling types and coupling strength on synchronization behavior of the three-oscillator cardiac conduction model. In this Section we consider the following cases:

a. Voltage coupling term in the first equation only ($K_{V2} = K_C = 0$),
b. Voltage coupling term in the second equation only ($K_{V1} = K_C = 0$),
c. Current coupling term in the second equation only ($K_{V1} = K_{V2} = 0$),
d. Voltage term in the first equation with current term in the second equation ($K_{V2} = 0$),
e. Both voltage and current coupling terms in the second equation ($K_{V1} = 0$).

In all these cases the coupling terms were symmetrical and coupling was unidirectional, i.e. from SA node to AV node and then to HP system. In the simulations for the cases with combined coupling terms (**d**) and (**e**), current coupling coefficient was changed proportionally to the voltage one - that is, $K_C = 10 \cdot K_{V1}$, and $K_C = 0.1 \cdot K_{V2}$ for (**d**) and (**e**) cases, respectively. Here, the proportionality coefficients were chosen taking into account approximate ranges of coupling coefficients based on simulation results in the cases (**a**), (**b**), and (**c**), when full frequency synchronization was not achieved yet.

Pure voltage coupling effortlessly produce fairly correct intervals between SA and HP pacemakers, and thereby, produce virtually correct P–R intervals. In such a case, the system of differential equations may be solved without time delays implemented in the equations (4.13) and (4.14). On the other hand, utilization of the current coupling in the model requires addition of time delays to the coupling terms in the above-mentioned equations to obtain correct P–R intervals [151].

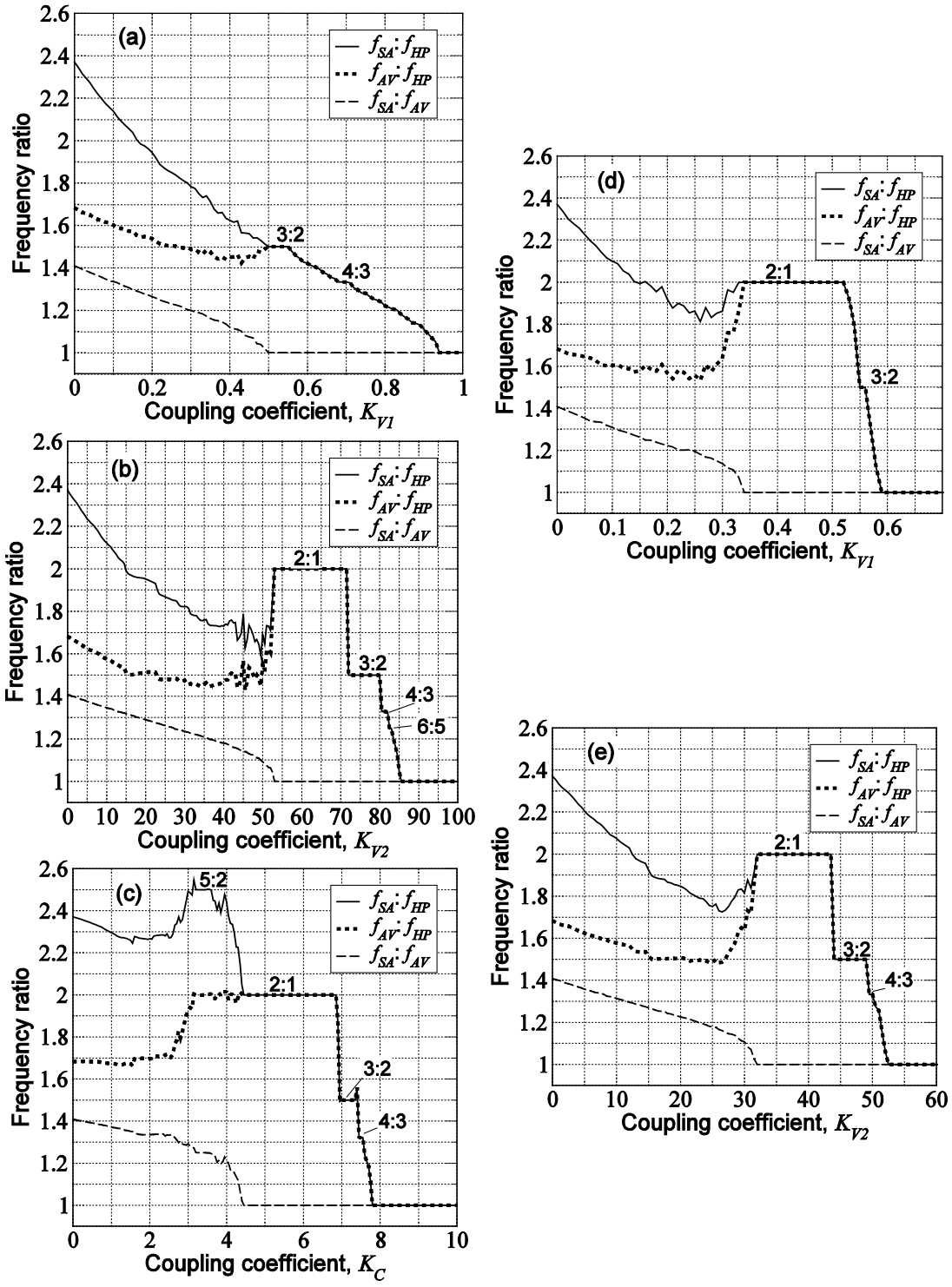

Figure 4.21: Dependences of frequencies ratios on coupling coefficients for single coupling cases (**a**) – (**c**), and combined coupling cases (**d**) and (**e**) at 70 bpm sinus rate.

4.7.3 Results

Figure 4.21 demonstrates calculated dependence of frequency ratios between SA (f_{SA}), AV (f_{AV}), and HP (f_{HP}) pacemakers on a coupling coefficient corresponding to the above described cases with single (**a**) – (**c**) and combined (**d**) and (**e**) couplings for the sinus rate of 70 bpm. As coupling strength increases, different synchronization regimes can be seen. As a general trend in all cases, $f_{SA} : f_{AV}$ ratio (first and second oscillators) gradually decreases until frequency synchronization is reached. In contrast, $f_{AV} : f_{HP}$ ratio exhibits instability. This distinction in behavior can be attributed to smaller relative difference of native intrinsic firing rates in SA–AV pair of oscillators (70:50 bpm) than AV–HP one (50:30 bpm) at normal sinus rate 70 bpm.

For understanding of incomplete heart blocks, $f_{SA} : f_{HP}$ ratio is the most demonstrative, because only this characteristic is reflected on real ECG waveforms as the relation of P wave and QRS complex (P:QRS ratio).

As seen in Fig. 4.21, upon reaching the frequency synchronization in the SA–AV pair, the first mode-locked ratio (2:1) appears. Transitions to the next mode-locked ratios (3:2, 4:3, 6:5) take place due to interaction in AV–HP pair only until complete synchronization (between all three oscillators) is reached. The observed mode-locked regions correspond to different types of incomplete AV blocks occurring at regular sinus rhythms with fixed ratios between numbers of P waves and QRS complexes per cycle and observed in clinical practice [1]. Sizes of these regions correlate with the probability of the observation of specific ratio. Accordingly, often seen 2:1 P:QRS ratio is represented by wider regions, while rarer cases of 3:2, 4:3, and 6:5 have narrower stable zones. Complete heart blocks, when atria (P waves) and ventricles (QRS complexes) are beating independently, are seen in Fig. 4.21 in the areas from $K = 0$ till the first moment when any slower oscillator mode locks to the faster one.

Among all five cases, on the dependence for the case (**a)** [Fig. 4.21(a)] the most frequently observed in clinical practice mode 2:1 is totally missing. In the case (**c**) [Fig. 4.21(c)] rather rare ratio 5:2 is seen, which appears due to early synchronization in AV–HP pair while SA–AV pair is not synchronized yet.

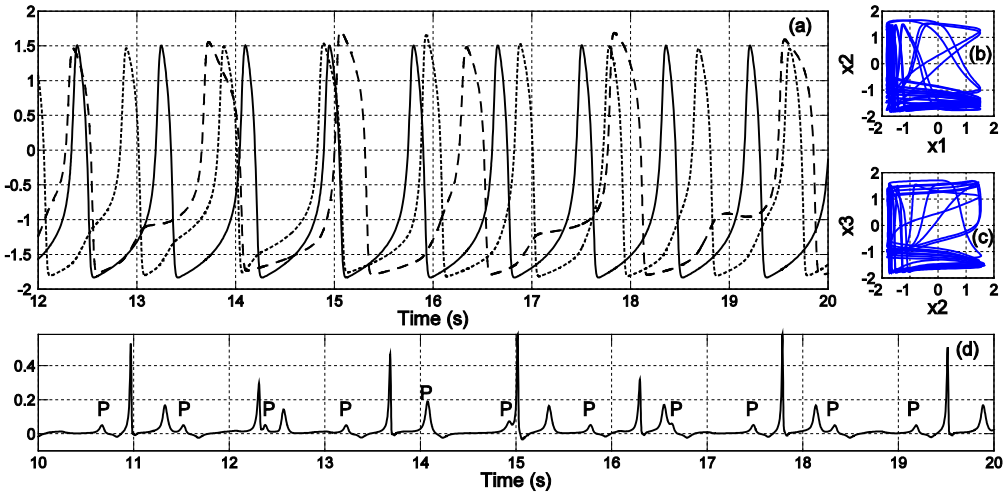

Figure 4.22: Calculated action potentials (a) for SA (solid line), AV (dotted line) and HP (dashed line), projection of the phase space (b)–(c), and ECG waveform (d) for case **b** at 70 bpm sinus rate and K_{V2} = 47. Chaotic behavior.

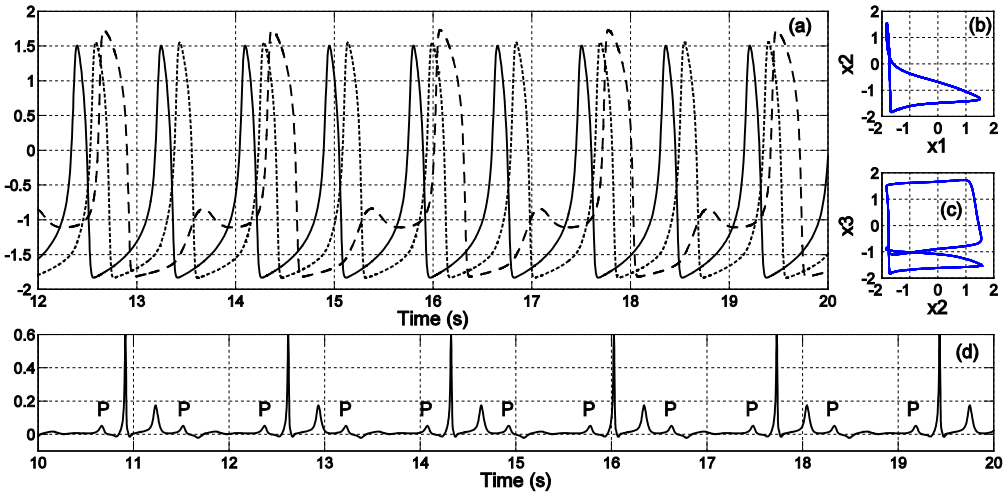

Figure 4.23: Same as in Fig. 4.22, but for K_{V2} = 65. Incomplete 2:1 block.

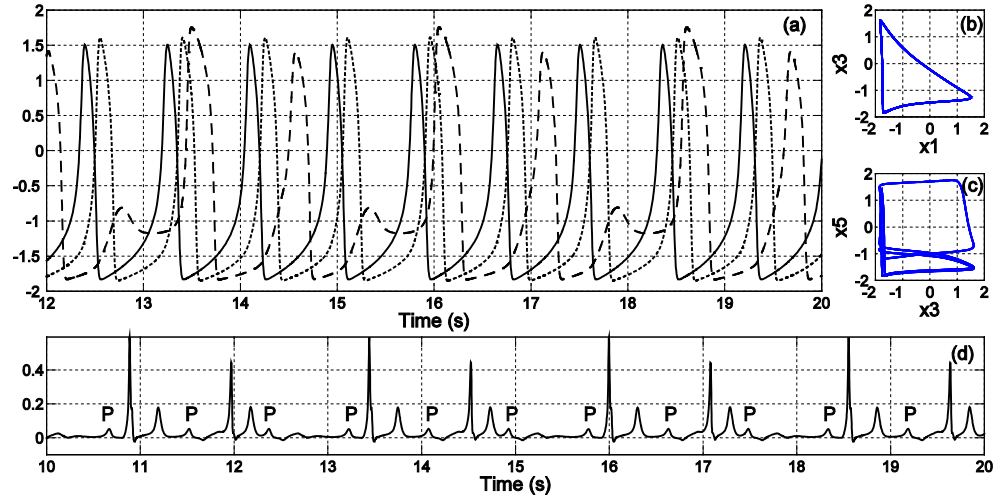

Figure 4.24: Same as in Fig. 4.22, but for K_{V2} = 76. Incomplete 3:2 block.

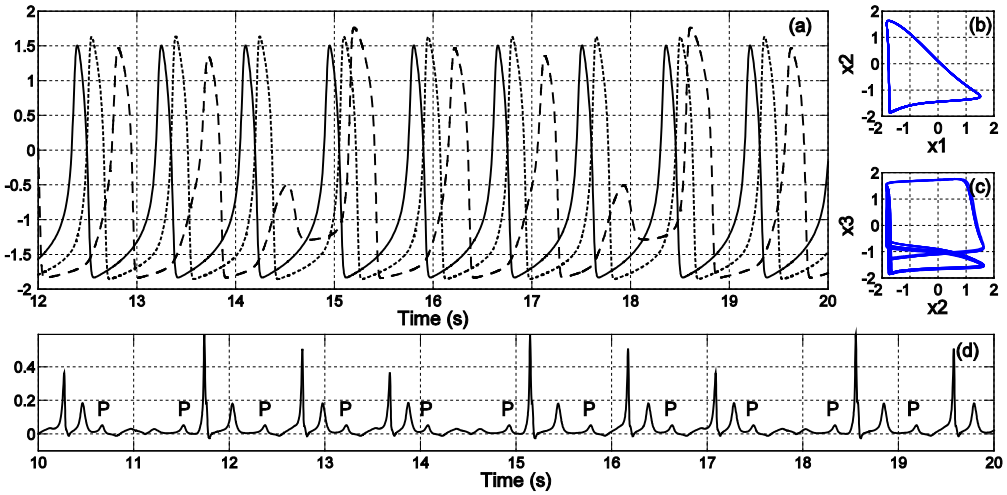

Figure 4.25: Same as in Fig. 4.22, but for K_{V2} = 82. Incomplete 4:3 block.

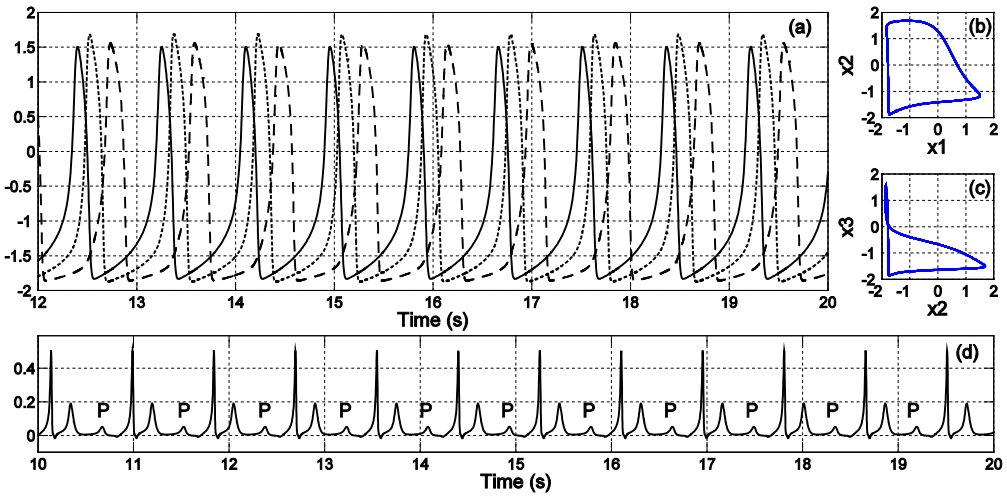

Figure 4.26: Same as in Fig. 4.22, but for K_{V2} = 100. Almost normal rhythm.

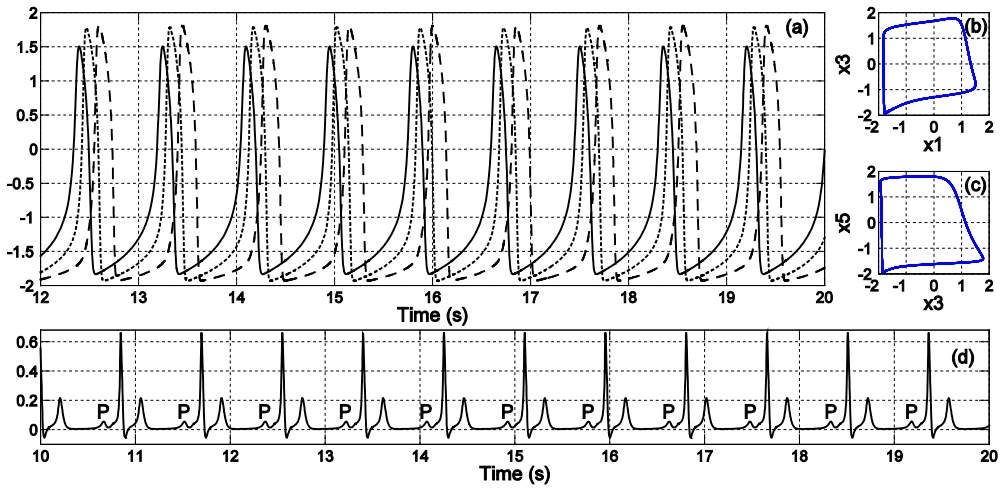

Figure 4.27: Same as in Fig. 4.22, but for K_{V2} = 170. Normal rhythm.

Figures 4.22 – 4.27 demonstrate the action potentials, projection of the phase space, and ECG waveforms calculated at 70 bpm sinus rate for different values of coupling coefficient K_{V2} [case (**b**)]. Here the case (**b)** was chosen as it yields many mode-locked modes, and the values of K_{V2} were selected for the most demonstrative synchronization situations.

In Figs. 4.22 – 4.25 (parts a) not all HP action potentials (some of them are under threshold) follow SA and AV action potentials. Thus, respective number of QRS complexes does not correspond to the number of P waves as it seen on ECG waveforms on Figs. 4.22 – 4.27 (parts d). Figures 4.22 – 4.27 (parts b and c) show projection of the phase space for x_1–x_2 (SA–AV) and x_2–x_3 (AV–HP) oscillator pairs, respectively, and clearly demonstrate the difference between chaotic and mode-locked synchronization regimes. The transitions between different synchronization states are accompanied by unstable (chaotic) behavior as it seen in Fig. 4.21 [and particular example in Figs. 4.22(b) and 4.22(c)]. Rather high chaotic amplitudes can be explained by difficulty of precise automatic frequency calculation of pacemaker time series.

The numerical simulations using the oscillator model with and without time delay couplings were performed in MATLAB environment employing DDE23 function [141]. Calculations of the frequency rations (Fig. 4.21) on Dell Precision T1700 workstation with Xeon E3-1245 processor took a few days.

4.7.4 Conclusion

We can finally conclude that the case a with single voltage coupling in the first equation of the sets (4.13) and (4.14) is not suitable for the study of full variety of incomplete AV blocks, and even the addition of current coupling in the second equation in (4.13) and (4.14) [case (**d**)] does not improve the situation with revealing of heart blocks. In the cases **b** and **c** we obtained a number of mode-locked states (modes) with different ratios. Thus, the case (**e**) [combination of voltage and current couplings in (4.13) and (4.14)] seems to be the most suitable for these kinds of studies. However, taking into account notable interest to atrial tachyarrhythmias [152], further investigation is required for accurate selection of proper coefficient ratios between K_{V2} and K_C, in particular, at high sinus rates.

4.8 Chapter summary

In this chapter, we proposed a model of cardiac conduction system including main pacemakers and heart muscles. SA node, AV node and HP were represented by modified van der Pol-type oscillators connected with time-delay velocity coupling. For description of atrial and ventricular muscles, where depolarization and repolarization processes are considered as separate waves, we used modified FitzHugh–Nagumo model. With the developed model, we obtained synthetic ECG as a combined signal of atrial and ventricular muscles and reproduced several normal and pathological rhythms. Inclusion of cardiac muscle response allowed to investigate interactions between pacemakers and resulting global heartbeat dynamics by means of clinically comparable realistic ECG signals. This feature distinguishes our model from existing cardiac oscillator models.

Further, we considered different coupling configurations between modified van der Pol oscillations for calculation of ECG signals in the heart model. We calculated frequency ratios for different coupling situations and obtained several fixed mode-locked states (modes) corresponding to different well known from clinical practice incomplete AV heart blocks. We can conclude that combined current-voltage coupling between oscillators (representing natural pacemakers) seems to be more suitable to reflect the physiological behavior of the cardiac electrical conduction system.

Chapter 5

Summary and future work

5.1 Thesis summary

The aim of this work was the application of different computer models to investigate basic mechanisms involved in cardiac arrhythmias and to obtain clinically comparable synthetic ECG signals.

We modeled normal and pathological cardiac activity by different approaches. At microscopic level, we studied mechanisms taking place in cardiac myocytes and their influence on whole-heart electrical response (ECG) (Chapters 2 and 3). At macroscopic level, we modeled interactions between different nodes of the heart-natural pacemakers and muscles (Chapter 4). Very important point is that the main output of both models is ECG waveforms, easily comparable with clinical data.

In the Chapter 2, we proposed a computer model for cardiac electrical behavior in atypical Brugada syndrome adjusting action potential parameters of pathological model cells in unusual specific locations in the original three-dimensional whole-heart Wei-Harumi heart model. We performed computer simulations of the disease using the Cardiomaster software, and demonstrated that action potential changes in case of atypical Brugada syndrome form lead to the same inducibility of ventricular fibrillation and increased risk of sudden cardiac death as in the typical one. The obtained results confirmed similar electrophysiological basis for both typical and atypical Brugada syndrome forms. We concluded that the disease might appear not only in the right precordial leads but also in the inferior and lateral leads as well (Refs. [J1] , [C1] and [C2]).

In the Chapter 3, we extended the original Wei-Harumi model in two aspects (Refs. [J2], [C3], and [C4]):

a) We modified a mathematical ion-channel model of human ventricular cells to fit their electrical action potential characteristics to the recent experimental data, and incorporated the proposed model into the biventricular Wei-Harumi heart model to

obtain more accurate investigation of the relationship between electro-chemical processes taking place in the cardiac cells and body surface ECG.

b) We proposed an algorithm for continuous spatial distribution of ventricular action potentials based on linearly distributed cellular ionic currents in order to implement modern knowledge of the ventricular wall 3-layer structure (epi-, endo-, and midmyocardial cells) in the Wei-Harumi model. We utilized the proposed algorithm in computer simulations of normal and pathological cardiac electrical functions.

In the Chapter 4 we considered the heart as a system of coupled nonlinear oscillators:

a) We developed a novel model of electrical cardiac conduction system, which controls normal heart rhythm consisting of main natural pacemakers (sinoatrial node, atrioventricular node and His-Purkinje system) and heart muscles. In the model, we represented pacemakers by modified van der Pol type oscillators connected with time-delayed velocity coupling. For description of atrial and ventricular muscles, where depolarization and repolarization processes are considered as separate electrical waves, we used modified FitzHugh-Nagumo model. Performing simulations with MATLAB software, we obtained synthetic ECG as a combined signal of atrial and ventricular muscles and reproduced several normal and pathological rhythms. Our model allows to study interactions between pacemakers and resulting global heartbeat dynamics by means of clinically comparable realistic ECG signals (Refs. [J3], [C5], and [C6]).

b) We investigated the effect of diffusive voltage and current couplings between natural pacemaker oscillators in the heterogeneous coupled oscillator model of ECG signals. We studied the synchronization of the oscillator system for normal and fast cardiac sinus rhythms and reproduced different mode-locked cases, which represent some incomplete heart blocks. The obtained results allow to demonstrate more realistic global behavior of interacting coupled natural pacemakers in the cardiac nonlinear oscillator model for studying heart rhythm dynamics (Ref. [C7]).

5.2 Future work

We believe this work will be helpful for further study and analysis of the mechanisms underlying cardiac arrhythmias. Still there are many problems and much remains to be done. Some of the possible future directions of the research are summarized below:

- As discussed in Chapter 3, the study of ventricular midmyocardial cells allocation in normal and abnormal conditions is necessary. For this purpose, we are planning to use the Cardiac CHASTE open source software for investigating the excitation sequence propagation in inhomogeneous tissue media based on reaction-diffusion method.
- Further inprovement and extention of the heterogeneous oscillator model of cardiac conduction system to study global cardiac electrical behavior.
    a) It is interesting to consider a contribution of intrinsic oscillation properties of cardiac natural pacemakers in the AV heart blocks formation introduced is Chapter 4.
    b) More intensive investigation of the mechanisms of initiation and termination of atrial and ventricular fibrillations with nonlinear dynamics approach using the developed oscillator model would provide mechanistic insights into life-threatening arrhythmias.
    c) Influence of external electromagnetic signals on cardiac electrical activity might reveal new directions for research.

Appendix

Membrane currents for of Ten Tusscher 2006 mathematical model

Equilibrium potentials E_X for equations below were calculated in accordance with the Nernst equation:

$$E_X = \frac{RT}{F}\ln\left(\frac{X_{ex}}{X_{in}}\right) \text{ for } X = \mathrm{Na}^+, \mathrm{K}^+, \mathrm{Ca}^{2+}, \tag{A1}$$

$$E_{Ks} = \frac{RT}{F}\ln\left(\frac{K_{ex} + p_{KNa}Na_{ex}}{K_{in} + p_{KNa}Na_{in}}\right). \tag{A2}$$

For gate variables the following general formula was used:

$$x^i = x_\infty - \left(x_\infty - x^{i-1}\right)\exp\left(-\frac{\Delta t}{\tau_x}\right), \text{ where } x = m,\ h,\ j, d,\ f,\ f_2,\ f_{cass}. \tag{A3}$$

1. Fast Na^+ current: I_{Na}

The three gates formulation of I_{Na} first introduced by Beeler and Reuter [153] are generally used:

$$I_{Na} = G_{Na}m^3hj(V - E_{Na}), \tag{A4}$$

where m is an activation gate, h is a fast inactivation gate, and j is a slow inactivation gate. Each of these gates is governed by Hodgkin-Huxley-type equations [72] for gating variables and characterized by a steady-state value and a time constant for reaching this steady-state value, both of which are functions of membrane potential.

$$m_\infty = \frac{1}{\left[1+\exp\left(\frac{-56.86 - V}{9.03}\right)\right]^2}; \tag{A5}$$

$$\alpha_m = \frac{1}{1+\exp\left(\frac{-60 - V}{5}\right)}; \tag{A6}$$

$$\beta_m = \frac{0.1}{1+\exp\left(\frac{V+35}{5}\right)} + \frac{0.1}{1+\exp\left(\frac{V-50}{200}\right)}; \quad \text{(A7)}$$

$$\tau_m = \alpha_m \beta_m; \quad \text{(A8)}$$

$$h_\infty = \frac{1}{\left[1+\exp\left(\frac{V+71.55}{7.43}\right)\right]^2}; \quad \text{(A9)}$$

$$\begin{cases} \alpha_h = 0, & V \geq -40 \text{ mV} \\ \alpha_h = 0.057\exp\left(\frac{-(V+80)}{6.8}\right), & V < -40 \text{ mV} \end{cases}; \quad \text{(A10)}$$

$$\begin{cases} \beta_h = \frac{0.77}{0.13\left[1+\exp\left(\frac{-(V+10.66)}{11.1}\right)\right]}, & V \geq -40 \text{ mV} \\ \beta_h = 2.7\exp(0.079V) + 3.1\cdot 10^5 \exp(0.3486V), & V < -40 \text{ mV} \end{cases}; \quad \text{(A11)}$$

$$\tau_h = \frac{1}{\alpha_h + \beta_h}; \quad \text{(A12)}$$

$$j_\infty = \frac{1}{\left[1+\exp\left(\frac{V+71.55}{7.43}\right)\right]^2}; \quad \text{(A13)}$$

$$\begin{cases} \alpha_j = 0, & V \geq -40 \text{ mV} \\ \alpha_j = \frac{\left[-2.5428\cdot 10^4 \exp(0.2444V) - 6.948\cdot 10^{-6}\exp(-0.04391V)\right](V+37.78)}{1+\exp\left[0.311(V+79.23)\right]}, & V < -40 \text{ mV} \end{cases}; \quad \text{(A14)}$$

$$\begin{cases} \beta_j = \frac{0.6\exp(0.057V)}{1+\exp(-0.1(V+32))}, & V \geq -40 \text{ mV} \\ \beta_j = \frac{0.02424\exp(-0.01052V)}{1+\exp(-0.1378(V+40.14))}, & V < -40 \text{ mV} \end{cases}; \quad \text{(A15)}$$

$$\tau_j = \frac{1}{\alpha_j + \beta_j}. \tag{A16}$$

2. Transient outward current I_{to}

For I_{to} the following formulation is used:

$$I_{to} = G_{to} rs(V - E_K), \tag{A17}$$

where r is a voltage-dependent activation gate and s is a voltage dependent inactivation gate. The steady-state activation curve (r_∞) is fitted to data on steady-state activation of I_{to} current in human ventricular myocytes of epicardial and endocardial origin at 35°C (308 K) from Nabauer *et al.* [154]. Because no significant difference between activation in epicardial and endocardial cells was found, a single formulation was used. G_{to} is fitted to experimental data on current density from Wettweret *et al.* [155] and Nabauer *et al.* [154]. Both show large differences in I_{to} size between epicardial and endocardial cells. G_{to} = 0.294 nS/pF for epicardial and G_{to} = 0.073 nS/pF for endocardial cells (25% of the value for epicardial cells) are used.

$$r_\infty = \frac{1}{1 + \exp\left(\frac{20 - V}{6}\right)}; \tag{A18}$$

$$\tau_r = 9.5 \exp\left(-\frac{(V + 40)^2}{1800}\right) + 0.8. \tag{A19}$$

For epicardial and M cells

$$s_\infty = \frac{1}{1 + \exp\left(\frac{V + 20}{5}\right)}; \tag{A20}$$

$$\tau_s = 1000 \exp\left(-\frac{(V + 67)^2}{1000}\right) + 8. \tag{A21}$$

3. Slow delayed rectifier current: I_{Ks}

For the slow delayed rectifier current the following formulation is used

$$I_{Ks} = G_{Ks} x_s^2 (V - E_{Ks}), \tag{A22}$$

where x_s is an activation gate and E_{Ks} is a reversal potential determined by a large permeability to potassium and a small permeability to sodium ions. Fitting G_{Ks} to experimentally obtained current densities would result in small I_{Ks} that have little effect on APD: simulating M cells by a 75% reduction in I_{Ks} density (the principal difference with epicardial cells) [98].

$$x_{s\infty} = \frac{1}{1+\exp\left(\frac{-5-V}{14}\right)}; \tag{A23}$$

$$\alpha_{xs} = \frac{1400}{\sqrt{1+\exp\left(\frac{5-V}{6}\right)}}; \tag{A24}$$

$$\beta_{xs} = \frac{1}{1+\exp\left(\frac{V-35}{15}\right)}; \tag{A25}$$

$$\tau_{xs} = \alpha_{xs}\beta_{xs} + 80. \tag{A26}$$

4. Rapid delayed rectifier current: I_{Kr}

The rapid delayed rectifier current is described by the following equation

$$I_{Kr} = G_{Kr}\sqrt{\frac{K_0}{5.4}}x_{r1}x_{r2}(V - E_K), \tag{A27}$$

where x_{r1} is an activation gate and x_{r2} is an inactivation gate. $\sqrt{K_0/5.4}$ represents the K_o dependence of the current.

$$x_{r1\infty} = \frac{1}{1+\exp\left(\frac{-26-V}{7}\right)}; \tag{A28}$$

$$\alpha_{xr1} = \frac{450}{1+\exp\left(\frac{-45-V}{10}\right)}; \tag{A29}$$

$$\beta_{xr1} = \frac{6}{1+\exp\left(\frac{V+30}{11.5}\right)}; \tag{A30}$$

$$\tau_{xr1} = \alpha_{xr1}\beta_{xr1}; \tag{A31}$$

$$x_{r2\infty} = \frac{1}{1+\exp\left(\frac{V+88}{24}\right)}; \tag{A32}$$

$$\alpha_{xr2} = \frac{3}{1+\exp\left(\frac{-60-V}{20}\right)}; \tag{A33}$$

$$\beta_{xr2} = \frac{1.12}{1+\exp\left(\frac{V-60}{20}\right)}; \tag{A34}$$

$$\tau_{xr2} = \alpha_{xr2}\beta_{xr2}. \tag{A35}$$

5. Inward rectifier K^+ current: I_{K1}

For I_{K1} the following formulation is used

$$I_{K1} = G_{K1}\sqrt{\frac{K_0}{5.4}}x_{K1}(V - E_K), \tag{A36}$$

where $x_{K1\infty}$ is a time-independent inward rectification factor that is a function of voltage. $\sqrt{K_0/5.4}$ again represents the K_0 dependence of the current.

$$\alpha_{K1} = \frac{0.1}{1+\exp\left(0.06(V - E_K - 200)\right)}; \tag{A37}$$

$$\beta_{K1} = \frac{3\exp\left(0.0002(V - E_K + 100)\right) + \exp\left(0.1(V - E_K - 10)\right)}{1+\exp\left(-0.5(V - E_K)\right)}; \tag{A38}$$

$$x_{K1\infty} = \frac{\alpha_{K1}}{\alpha_{K1} + \beta_{K1}}. \tag{A39}$$

6. Na^+/ Ca^{2+} exchanger current I_{NaCa}

For I_{NaCa} the following equation is used:

$$I_{NaCa} = k_{NaCa} \frac{\exp\left[\gamma \frac{VF}{RT}\right] Na_i^3 Ca_O - \exp\left[(\gamma - 1)\frac{VF}{RT}\right] Na_O^3 Ca_i \alpha}{\left(K_{mNa_i}^3 + Na_O^3\right)\left(K_{mCa} + Ca_O\right)\left(1 + k_{sat} \exp\left[(\gamma - 1)\frac{VF}{RT}\right]\right)}. \quad \text{(A40)}$$

This formulation is similar to the equation used in the LR model, except for the extra factor α = 2.5 that accounts for the higher concentration of calcium in the subspace close to the sarcolemmal membrane where the Na^+/Ca^{2+}exchanger is actually operating.

7. Na^+/ K^+ pump current I_{NaK}

$$I_{NaK} = R_{NaK} \frac{K_O Na_i}{\left(K_O + K_{mK}\right)\left(Na_i + K_{mNa}\right)\left(1 + 0.1245 \exp\left[-0.1\frac{VF}{RT}\right] + 0.0353 \exp\left[-\frac{VF}{RT}\right]\right)}. \quad \text{(A41)}$$

This formulation is similar to the formulations used in the LR, PB, and Courtemanche, Ramirez, and Nattel [156] models.

8. Plateau and background currents

For I_{pCa} the following commonly applied equation is used:

$$I_{pCa} = G_{pCa} \frac{Ca_i}{K_{pCa} + Ca_i}. \quad \text{(A42)}$$

For I_{pK} the following equation is used:

$$I_{pK} = G_{pK} \frac{V - E_K}{1 + \exp\left(\frac{25 - V}{5.98}\right)}. \quad \text{(A43)}$$

The background sodium I_{bNa} and calcium leakage I_{bCa} currents are given by the following equations:

$$I_{bNa} = G_{bNa}(V - E_{Na}); \quad \text{(A44)}$$

$$I_{bNa} = G_{bNa}(V - E_{Na}). \quad \text{(A45)}$$

9. L-type calcium current I_{CaL}

L-type calcium current injects calcium into the subspace and in turn is inactivated by the Ca_{ss} via the inactivation gate f_{cass}. Both a slow voltage inactivation gate f and a fast voltage inactivation gate f_2 are incorporated.

$$I_{CaL} = G_{CaL} d\ f\ f_2\ f_{cass} 4\frac{(V-15)F^2}{RT}\frac{0.25Ca_{ss}\exp\left(2\frac{(V-15)F}{RT}\right)-Ca_0}{\exp\left(2\frac{(V-15)F}{RT}\right)-1}; \quad \text{(A46)}$$

$$d_\infty = \frac{1}{1+\exp\left(\frac{-8-V}{7.5}\right)}; \quad \text{(A47)}$$

$$\alpha_d = \frac{1.4}{1+\exp\left(\frac{-35-V}{13}\right)}+0.25; \quad \text{(A48)}$$

$$\beta_d = \frac{1.4}{1+\exp\left(\frac{V+5}{5}\right)}; \quad \text{(A49)}$$

$$\gamma_d = \frac{1}{1+\exp\left(\frac{50-V}{20}\right)}; \quad \text{(A50)}$$

$$\tau_d = \alpha_d\beta_d + \gamma_d; \quad \text{(A51)}$$

$$f_\infty = \frac{1}{1+\exp\left(\frac{V+20}{7}\right)}; \quad \text{(A52)}$$

$$\alpha_f = 1102.5\exp\left(-\left(\frac{V+27}{15}\right)^2\right); \quad \text{(A53)}$$

$$\beta_f = \frac{200}{1+\exp\left(\frac{13-V}{10}\right)}; \quad \text{(A54)}$$

$$\gamma_f = \frac{180}{1+\exp\left(\frac{V+30}{10}\right)}+20; \quad \text{(A55)}$$

$$\tau_f = \alpha_f + \beta_f + \gamma_f ; \tag{A56}$$

$$f_{2\infty} = \frac{0.67}{1+\exp\left(\frac{V+35}{7}\right)} + 0.33 ; \tag{A57}$$

$$\alpha_{f2} = 600\exp\left(-\frac{(V+25)^2}{170}\right); \tag{A58}$$

$$\beta_{f2} = \frac{31}{1+\exp\left(\frac{25-V}{10}\right)}; \tag{A59}$$

$$\gamma_{f2} = \frac{16}{1+\exp\left(\frac{V+30}{10}\right)}; \tag{A60}$$

$$\tau_{f2} = \alpha_{f2} + \beta_{f2} + \gamma_{f2} ; \tag{A61}$$

$$f_{cass\infty} = \frac{0.6}{1+\left(\frac{Ca_{ss}}{0.05}\right)^2} + 0.4 ; \tag{A62}$$

$$\tau_{fcass} = \frac{80}{1+\left(\frac{Ca_{ss}}{0.05}\right)^2} + 2 . \tag{A63}$$

10. Calcium dynamics

In the following equations, Ca_{itotal} is total (free+buffered) cytoplasmic Ca^{2+} concentration; $Ca_{srtotal}$ is total SR Ca^{2+}concentration; $Ca_{sstotal}$ is total dyadic subspace Ca^{2+}concentration; Ca_i is free cytoplasmic Ca^{2+}concentration; Ca_{sr} is free SR Ca^{2+} concentration; Ca_{ss} is free dyadic subspace Ca^{2+} concentration; I_{rel} is Ca^{2+}-induced Ca^{2+}-release current; I_{up} is SR Ca^{2+} pump current; I_{leak} is SR Ca^{2+} leak current; I_{xfer} is diffusive Ca^{2+} current between dyadic Ca^{2+} subspace and bulk cytoplasm; O is proportion of open I_{rel} channels; and R_{ch} is proportion of closed I_{rel} channels.

$$I_{leak} = G_{leak}(Ca_{sr} - Ca_i) ; \tag{A64}$$

$$I_{up} = \frac{G_{\max up}}{1 + K_{up}^2 / Ca_i^2}; \tag{A65}$$

$$I_{rel} = G_{rel} O(Ca_{sr} - Ca_{ss}); \tag{A66}$$

$$I_{xfer} = G_{xfer} O(Ca_{ss} - Ca_i); \tag{A67}$$

$$O = \frac{k_1 Ca_{ss}^2 R_{ch}}{k_3 + k_1 Ca_{ss}^2}; \tag{A68}$$

$$\frac{d\overline{R}}{dt} = -k_2 Ca_{ss} R_{ch} + k_4 (1 - R_{ch}); \tag{A69}$$

$$k_1 = \frac{k_1^{'}}{k_{casr}}; \tag{A70}$$

$$k_2 = k_2^{'} k_{casr}; \tag{A71}$$

$$k_{casr} = \max_{sr} - \frac{\max_{sr} - \min_{sr}}{1 + (EC / Ca_{sr})^2}; \tag{A72}$$

$$Ca_{ibufc} = \frac{Ca_i \cdot Buf_c}{Ca_i + K_{bufc}}; \tag{A73}$$

$$\frac{dCa_{itotal}}{dt} = -\frac{I_{bCa} + I_{pCa} + 2I_{NaCa}}{2\Gamma_c F} + \frac{\Gamma_{sr}}{\Gamma_c}(I_{leak} - I_{up}) + I_{xfer}; \tag{A74}$$

$$Ca_{srbufsr} = \frac{Ca_{sr} \cdot Buf_{sr}}{Ca_{sr} + K_{bufsr}}; \tag{A75}$$

$$\frac{dCa_{srtotal}}{dt} = (I_{up} - I_{leak} - I_{rel}); \tag{A76}$$

$$Ca_{ssbufss} = \frac{Ca_{ss} \cdot Buf_{ss}}{Ca_{ss} + K_{bufss}}; \tag{A77}$$

$$\frac{dCa_{sstotal}}{dt} = -\frac{I_{CaL}}{2\Gamma_{ss} F} + \frac{\Gamma_{sr}}{\Gamma_{ss}} I_{rel} - \frac{\Gamma_c}{\Gamma_{ss}} I_{xfer}. \tag{A78}$$

Bibliography

[1] Handbook of cardiac arrhythmia, P. J. Podid and P.R. Kowey, Eds., Williams & Wilkins, 1996.

[2] S. S. Ryan, Atrial fibrillation: Resources for Patients, http://a-fib.com, 2014.

[3] Handbook of cardiac electrophysiology, A. Natale and O. Wazni, Eds., Informa, UK, 2007.

[4] http://biochemaliensunite.wordpress.com, 2015.

[5] R. E. Klabunde, Cardiovascular physiology concepts, http://www.CVphysiology.com, 2009.

[6] Cardiac electrophysiology: From cell to bedside, D. P. Zipes and J. Jalife, Eds., Elsevier Sounders, USA, 2004.

[7] M.S. Thaler, The only ECG book you'll ever need, Lippincott, Williams & Wilkins, USA, 2012.

[8] ECG Library, http://lifeinthefastlane.com/ecg-library, 2015.

[9] Electrocardiology laboratory, http://www.indiana.edu/~p409/labecg.html, 2015.

[10] H.M. Den Ruijter, G. Berecki, T. Opthof, A.O. Verkerk, P.L. Zock, and R. Coronel. Pro- and antiarrhythmic properties of a diet rich in fish oil. *Cardiovasc. Res.*, 73:316–325, 2007.

[11] M. Lorange, R. M. Gulrajani, J. de Guise, and P. Fortier. A whole-heart model incorporating myocardial anisotropy. *IEEE Proc. Annu. Int. Conf.* IEEE IEMBS, 1:195, 1988.

[12] M. Potse, B. Dube, J. Richer, A.Vinet, and R. M. Gulrajani. A comparison of monodomain and bidomain reaction-diffusion models for action potential propagation in the human heart. *IEEE Trans. Biomed. Eng.*, 53(12): 2425-2435, 2006.

[13] G.R. Mirams, C.J. Arthurs, M.O. Bernabeu, R. Bordas, J. Cooper, A. Corrias, Y. Davit, S.J. Dunn, A.G. Fletcher, D.G. Harvey, M.E. Marsh, J.M. Osborne,

P. Pathmanathan, J. Pitt-Francis, J. Southern, N. Zemzemi, and D. J. Gavaghan. Chaste: An open source C++ library for computational physiology and biology. PLoS Comput. Biol., 9(3): e1002970, 2013.

[14] M. E. Belik, T.P. Usyk, and A.D. McCulloch. Computational methods for cardiac electrophysiology. *Computational Models for the Human Body, Special Volume of Handbook of Numerical Analysis*, N. Ayache, Ed. Philadelphia, USA: Elsevier, XII: 129-188, 2004.

[15] P. Hunter and P. Nielsen. A strategy for integrative computational physiology. *Physiology*, 20: 316–325, 2005.

[16] D. Noble and Y. Rudy. Models of cardiac ventricular action potentials: iterative interaction between experiment and simulation. *Philos. Trans. R. Soc. Lond. A*, 359: 1127–1142, 2001.

[17] G. Plank, L. Zhou, J. L. Greenstein, S. Cortassa, R. L. Winslow, B. O'Rourke, and N. Trayanova. From mitochondrial ion channels to arrhythmias in the heart: computational techniques to bridge the spatio-temporal scales. *Phil. Trans. R. Soc. A*, 366, 3381–3409, 2008.

[18] N.A. Trayanova. Whole-heart modeling: applications to cardiac electrophysiology and electromechanics. *Circ. Res.*, 108:113-128, 2011.

[19] D.U.J. Keller, O. Jarrousse, T. Fritz, S. Ley, O. Dossel, and G. Seemann. Impact of physiological ventricular deformation on the morphology of the T-wave: a hybrid, static-dynamic approach. *IEEE Trans. Biomed. Eng*., 58(7): 2109-2119, 2011.

[20] T. Washio, J.Okada, and T. Hisada. A parallel multilevel technique for solving the bidomain equation on a human heart with Purkinje fibers and a torso model. *SIAM Rev*., 52(4):717–743, 2010.

[21] M. Aoki, Y. Okamoto, T. Musha, and K. Harumi. Three-dimensional simulation of the ventricular depolarization and repolarization processes and body surface potentials: normal heart and bundle branch block. *IEEE Trans. Biomed. Eng.*, 34(6):454–462, 1987.

[22] K. Harumi, M. Burgress, and J. Abildskov. A theoretical model of the T wave. *Circulation*, 34:657–668, 1966.

[23] D. Wei, G. Yamada, T. Musha, H. Tsunakawa, T. Tsutsumi, and K. Harumi. Computer simulation of supraventricular tachycardia with the Wolff-

Parkinson-White syndrome using three-dimensional heart models. *J. Electrocardiol.*, 23(3):261–173, 1990.

[24] D. Wei, O. Okazaki, K. Harumi, E. Harasawa, and H. Hosaka. Comparative simulation of excitation and body surface electrocardiogram with isotropic and anisotropic computer heart models. *IEEE Trans. Biomed. Eng.*, 42(4):343–357, 1995.

[25] D. Wei. Whole-heart modeling: progress, principles and applications. *Prog. Biophys. Mol. Biol.*, 67(1):17–66, 1997.

[26] D. Wei. Whole-heart modeling and simulation. *Modeling and imaging of bioelectrical activity: principles and applications*, B. He, Ed. Norwell, USA: Kluwer Academic, 2004.

[27] X. Zhu and D. Wei. Computer simulation of intracardiac potential with whole-heart model. *Int. J. Bioinformatics Research and Applications*, 3(1):100–122, 2007.

[28] X. Zhu, D. Wei, and O. Okazaki. Computer simulation of clinical electrophysiological study. *PACE*, 35(6):718-729, 2012.

[29] E. Ryzhii and D. Wei. Computer simulation of atypical Brugada syndrome. *J. Electrocardiol.*, 42:319–327, 2009.

[30] E. Ryzhii. Investigation of spatial action potential distributions in myocardium using three-dimensional biventricular heart model. *J. Comm. Tech. Electron.*, 57(1):82–90, 2012.

[31] D. Wei. Analysis of electric phenomena of the heart: the development of Cardiomaster of Windows edition. Proceedings of the*14th Autumn Conference of the Japan Society of Medical and Electronics and Biological Engineering*, 70, Japan Society of Medical Electronics and Biological Engineering, October 2000.

[32] K. Harumi, T. Tsutsumi, T. Sato, and S. Sekiya. Classification of antiarrhythmic drugs based on ventricular fibrillation threshold. *Am. J. Cardiol.*, 64(20):10J–14J, 1989.

[33] D. Durrer, R. T. van Dam, G. E. Freud, M. J. Janse, F. L. Meijler, and R. C. Arzbaecher. The total excitation of the isolated human heart, *Circulation*, 41:899–912, 1970.

[34] S. Spaggiari, S. Baruffi, G. Arisi, E. Macchi, and B. Taccardi. Effect of intramural fiber orientation on epicardial isochrone and potential maps. *Circulation*, 76(s):241, 1987.

[35] W. T. Miller and D. B. Geselowitz. Simulation studies of the electrocardiogram: I. The normal heart. *Circ. Res.*, 43:301–315, 1978.

[36] W. T. Miller and D. B. Geselowitz. Simulation studies of the electrocardiogram: II, Ischemia and infarction. *Circ. Res.*, 43:315–323, 1978.

[37] D. B. Geselowitz. Theory and simulation of the electrocardiogram, in *Comprehensive electrocardiology*, P. W. MacFarlane, and T. D. V. Lawrie, Eds., Pergamon, New York, 181, 1989.

[38] L. Clerc. Directional differences of impulse spread in trabecular muscle from mammalian heart. *J. Physiol.*, 255:335–345, 1976.

[39] D. E. Roberts, L. T. Hersh, and A. M. Scher. Influence of cardiac fiber orientation on wavefront voltage, conduction velocity, and tissue resistivity. *Circ. Res.*, 44:701–712, 1979.

[40] R. M. Gulrajani, F. A. Roberg, and G. E. Mailloux. The forward problem of electrocardiography, in *Comprehensive Electrocardiology*, P.W. MacFarlane and T. D. V. Lawrie, Eds., Pergamon, New York, p. 197, 1998.

[41] S. V. Shahidi and P. Savad. Forward problem of electrocardiography: construction of human torso models and field calculation using finite element models. *Med. Biol. Eng. Comp.*, 32:S25, 1994.

[42] K. Harumi, H. Tsunakawa, G. Nishiyama, D. Wei, G. Yamada, Y. Okamoto, and T. Musha. Clinical application of electrocardiographic computer model. *J. Electrocardiol.*, 22(s):54–63, 1989.

[43] P. Brugada and J. Brugada. Right bundle branch block, persistent ST segment elevation and sudden cardiac death: a distinct clinical and electrocardiographic syndrome. A multicenter report. *J. Am. Coll. Cardiol.*, 20:1391–1396, 1992.

[44] M. Sahara, K. Sagara, T. Yamashita, T. Abe, H. Kirigaya, M. Nakada, H. Iinuma, L.T. Fu, and H. Watanabe. J wave and ST segment elevation in the inferior leads. A latent type of variant Brugada syndrome? *Jpn. Heart*, 43(1):55–60, 2002.

[45] T. Ueyama, A. Shimizu, M. Esato, M. Kanemoto, R. Kametani, A. Sawa, S. Suzuki, and M. Matsuzaki. A case of a concealed type of Brugada syndrome with a J wave and mild ST-elevation in the inferolateral leads. *J. Electrocardiol.*, 40:39–42, 2007.

[46] H. Kalla, G. X. Yan, and R. Marinchak. Ventricular fibrillation in a patient with prominent J (Osborn) waves and ST segment elevation in the inferior electrocardiographic leads: a Brugada syndrome variant? *J. Cardiovasc. Electrophysiol.*, 11(1):95–98, 2000.

[47] M. Takagi, N. Aihara, H. Takaki, A. Taguchi, W. Shimizu, T. Kurita, K. Suyama, and S. Kamakura. Clinical characteristics of patients with spontaneous or inducible ventricular fibrillation without apparent heart disease presenting with J wave and ST segment elevation in inferior leads. *J. Cardiovasc. Electrophysiol.*, 11:844–848, 2000.

[48] M. Ogawa, K. Kumagai, Y. Yamanouchi, and K. Saku. Spontaneous onset of ventricular fibrillation in Brugada syndrome with J wave and ST-segment elevation in the inferior leads. *Heart Rhythm*, 2(1):97–99, 2005.

[49] A. Perez Riera, C. Ferreira, E. Schapachnik, P. Sanches, and P. Moffa. Brugada syndrome with atypical ECG: downsloping ST-segment elevation in inferior leads. *J. Electrocardiol.*, 37(2):101–104, 2004.

[50] K. Ohkubo, I. Watanabe, Y. Takagi, Y.Okumura, S. Ashino, M. Kofune, K. Kawauchi, T. Yamada, T. Kofune, K. Hashimoto, A. Shido, H. Sugimura, T. Nakai, S. Saito, and A. Hirayama. Electrocardiographic and electrophysiologic characteristics in patients with Brugada type electrocardiogram and inducible ventricular fibrillation: single center experience. *Circulation J.*, 71(9):1437–1441, 2007.

[51] L. P. Van Den Berg and A. C. P. Wiesfeld. Brugada syndrome with ST segment elevation in the lateral leads. *J. Cardiovasc. Electrophysiol.*, 7:1035, 2006.

[52] H. Bonakdar, M. Haghjoo, and M.A. Sadr-Ameli. Brugada syndrome manifested by the typical electrocardiographic pattern both in the right precordial and the high lateral leads. *Indian Pacing Electrophysiol. J.*, 8(2):137–140, 2008.

[53] F. Potet, P. Mabo, G. Le Coq, V. Probst, J. J. Schott, F. Airaud, G. Guihard, J. C. Daubert, D. Escande, and H. Le Marec. Novel Brugada SCN5A mutation leading to ST segment elevation in inferior or the right precordial leads. *J. Cardiovasc. Electrophysiol.*, 14(2):200–203, 2003.

[54] C. Antzelevitch. The Brugada syndrome: ionic basis and arrhythmia mechanisms. *J. Cardiovasc. Electrophysiol.*, 12(2):268–272, 2001.

[55] T. Kurita, W. Shimizu, M. Inagaki, K. Suyama, A. Taguchi, K. Satomi, N. Aihara, S. Kamakura, J. Kobayashi, and Y. Kosakai. The electrophysiologic mechanism of ST-segment elevation in Brugada syndrome. *J. Am. Coll. Cardiol.*, 40(2):330–334, 2002.

[56] R. H. Clayton and A. V. Holden. Effect of regional differences in cardiac cellular electrophysiology in the stability of ventricular arrhythmias: A computational study. *Phys. Med. Biol.*, 48:95–111, 2003.

[57] C. H. Luo and Y. Rudy. A dynamic model of the cardiac ventricular action potential: I. Simulations of ionic currents and concentration changes. *Circ. Res.*, 74:1071–1096, 1994.

[58] P. J. Hunter, A. J. Pullan, and B. H. Smaill. Modeling total heart function. *Annu. Rev. Biomed. Eng.*, 5:147–177, 2003.

[59] L. Xia, Y. Zhang, H. Zhang, Q. Wei, F. Liu, and S. Crozier. Simulation of Brugada syndrome using cellular and three-dimensional whole-heart modeling approaches. *Physiol. Meas.*, 27(11):1125–1142, 2006.

[60] O. Okazaki, Y. Yamauchi, M. Kashida, K. Izumo, N. Akatsuka, S. Ohnishi, M. Shoda, T. Nirei, H. Kasanuki, M. Ebato, S. Mashima, K. Harumi, and D. Wei. Possible mechanism of ECG features in patients with idiopathic ventricular fibrillation studied by heart model and computer simulation. *J. Electrocardiol.*, 30(s):98–104, 1998.

[61] Y. Mizusawa, A. A. M. Wilde. Brugada syndrome. *Circ. Arrhythm. Electrophysiol.*, 5:606–616, 2012.

[62] K. Hisamatsu, K. F. Kusano, H. Morita, S. Takenaka, S. Nagase, K. Nakamura, T. Emori, H. Matsubara, and T. Ohe. Usefulness of body surface mapping to differentiate patients with Brugada syndrome from patients with asymptomatic Brugada syndrome. *Acta Med. Okayama*, 58(1):29–35, 2004.

[63] L. Yamaki, I. Kubota, and H. Tomoike. Simulation of late potentials and arrhythmias by use of a three-dimensional heart model: causality of peri-infarctional slow conduction in ventricular fibrillation. *J. Electrocardiol.*, 32(2):115–121, 1999.

[64] D. W. Wang, P. C. Viswanathan, J. R. Balser, A. L. George Jr, and D. W. Benson. Clinical, genetic, and biophysical characterization of SCN5A mutations associated with atrioventricular conduction block. *Circulation*, 105(3):341–346, 2002.

[65] S. Nagase, K. F. Kusano, H. Morita, N. Nishii, K. Banba, A. Watanabe, S. Hiramatsu, K. Nakamura, S. Sakuragi, and T. Ohe. Longer repolarization in the epicardium at the right ventricular outflow tract causes type 1 electrocardiogram in patients with Brugada syndrome. *J. Am. Coll. Cardiol.*, 51(12):1154–1161, 2008.

[66] L. Priebe and D. J. Beuckelmann. Simulation study of cellular electric properties in heart failure. *Circ. Res.*, 82:1206–1223, 1998.

[67] O. Bernus, R. Wilders, C. W. Zemlin, H. Verschelde, and A. V. Panfilov. A computationally efficient electrophysiological model of human ventricular cells. *Am. J. Physiol. Heart Circ. Physiol.*, 282:H2296–H2308, 2002.

[68] K. H. W. J. ten Tusscher, D. Noble, P. J. Noble, and A. V. Panfilov. A model for human ventricular tissue. *Am. J. Physiol. Heart Circ. Physiol.*, 286:H1573–H1589, 2004.

[69] V. Iyer, R. Mazhari, and R. Winslow. A computational model of the human left-ventricular epicardial myocyte. *Biophys. J.*, 87:1507–1525, 2004.

[70] K. H. W. J. ten Tusscher and A. V. Panfilov. Alternans and spiral breakup in a human ventricular tissue model. *Am. J. Physiol. Heart Circ. Physiol.*, 291(3):H1088–H1100, 2006.

[71] The CellML project, *http://www.cellml.org/*.

[72] A. L. Hodgkin and A. F. Huxley. A quantitative description of membrane current and its application to conduction and excitation in nerve. *J. Physiol.*, 117:500–544, 1952.

[73] H. P. Langtangen. *Computational partial differential equations: numerical methods and Diffpack programming*. Springer, p. 633, 2003.

[74] A. Garny, P. Kohl, and D. Noble. Cellular Open Resource (COR): a public CellML based environment for modelling biological function. *Int. J. Bif. Chaos*, 13(12):3579–3590, 2003.

[75] V. A. Maltsev, H. N. Sabbah, R. S. D. Higgins, N. Silverman, M. Lesch, and A. I. Undrovinas. Novel, ultraslow inactivating sodium current in human ventricular cardiomyocytes. *Circulation*, 98:2545–2552, 1998.

[76] C. Antzelevitch and L. Belardinelli. The role of sodium channel current in modulating transmural dispersion of repolarization and arrhythmogenesis. *J. Cardiovasc. Electrophysiol*., 17(s1):S79–S85, 2006.

[77] V. A. Maltsev, H. N. Sabbah, and A. I. Undrovinas. Late sodium current is a novel target for amiodarone: Studies in failing human myocardium. *J. Mol. Cell. Cardiol*., 33:923–932, 2001.

[78] D. Noble, A. Varghese, P. Kohl, and P. Noble. Improved guinea-pig ventricular cell model incorporating a diadic space, I_{Kr} and I_{Ks}, and length and tension-dependent processes. *Can. J. Cardiol.*, 14:123–134, 1998.

[79] C. R. Weber, K. S. Ginsburg, K. D. Philipson, T. R. Shannon, and D. M. Bers. Allosteric regulation of Na^{+}–Ca^{2+} exchange current by cytosolic Ca in intact cardiac myocytes. *J. Gen. Physiol.*, 117:119–131, 2001.

[80] C. R. Weber, V. Piacentino 3rd, S.R. Houser, and D. M. Bers. Dynamic regulation of sodium/calcium exchange function in human heart fealure. *Circulation*, 108(18):2224–2229, 2003.

[81] G. R. Li, C. Lau, T. Leung, and S. Nattel. Ionic current abnormalities associated with prolonged action potentials in cardiomyocytes from diseased human right ventricles. *Heart Rhythm*, 4:460–468, 2004.

[82] R. F. Gilmour, J. J. Heger, E. N. Prystowsky, and D. Z. Zipes. Cellular electrophysiologic abnormalities of diseased human ventricular myocardium. *Am. J. Cardiol.*, 51:137–144, 1983.

[83] E. Wetter, G. J. Amos, H. Posival, and U. Ravens. Transient outward current in human ventricular myocytes of subepicardial and subendocardial origin. *Circ. Res.* , 75:473–482, 1994.

[84] T. J. Hund and Y. Rudy, Rate dependence and regulation of action potential and calcium transient in a canine cardiac ventricular cell model. *Circulation*, 110:3168–3174, 2004.

[85] S. Rush and H. Larsen. A practical algorithm for solving dynamic membrane equations. *IEEE Trans. Biomed. Eng.*, 25(4):389–392, 1978.

[86] M.E Marsh, S.T. Ziaratgahi, and R.J. Spiteri. The secrets to the success of the Rush-Larsen method and its generalizations. *IEEE Trans. Biomed. Eng*., 59(9): 2506–2515, 2012.

[87] G. - X. Yan, W. Shimizu, and C. Antzelevitch. Characteristics and distribution of M cells in arterially perfused canine left ventricular wedge preparations. *Circulation*, 98:1921–1927, 1998.

[88] C. Antzelevitch. Heterogeneity of cellular repolarization in LQTS: the role of M cells. *Eur. Heart J.*, 3:K2–K16, 2001.

[89] E. P. Anyuhovsky, E. A. Sosunov, and M. R. Rosen. Regional differences in electrophysiological properties of epicardium, midmyocardium, and endocardium. *In vitro* and *in vivo* correlations, *Circulation*, 94:1981–1988, 1996.

[90] E. P. Anyuhovsky, E. A. Sosunov, R. Z. Gainullin, and M. R. Rosen. The controversial M cell. *Circulation*, 10(2):244–260, 1999.

[91] E. Drouin, F. Charpentier, C. Gauthier, K. Laurent, and H. Le Marec. Electrophysiological characteristics of cells spanning the left ventricular wall of human heart: evidence for presence of M cells. *J. Am. Coll. Cardiol.*, 26:185–192, 1995.

[92] G. - R. Li, J. Feng, L. Yue, and M. Carrier. Transmural heterogeneity of action potentials and $I_{to}1$ in myocytes isolated from the human right ventricle. *Am. J. Physiol. Heart Circ. Physiol.*, 275:369–377, 1998.

[93] P. Colli Franzone, L. F. Pavarino, S. Scacchi, and B. Taccardi. Monophasic action potentials generated by bidomain modeling as a tool for detecting

cardiac repolarization times. *Am. J. Physiol. Heart Circ. Physiol.*, 293:H2771–H2785, 2007.

[94] J. V. Tranquillo, D. O. Burwell, and C. S. Henriquez. Analytical model of extracellular potentials in a tissue slab with a finite bath. *IEEE Trans. Biomed. Eng.*, 52 (2):334–338, 2005.

[95] N. Trayanova. Defibrillation of the heart: insights into mechanisms from modelling studies. *Exp. Physiol.*, 91(2):323–337, 2006.

[96] K. J. Sampson and C. G. S. Henriquez. Simulation and prediction of functional block in the presence of structural and ionic heterogeneity. *Am. J. Physiol. Heart Circ. Physiol.*, 281:H2597–H2603, 2001.

[97] M.-C. Trudel, B. Dubé, M. Potse, R. M. Gulrajani, and L. J. Leon. Simulation of QRST integral maps with a membrane-based computer heart model employing parallel processing. *IEEE Trans. Biomed. Eng.*, 51:1319– 1329, 2004.

[98] D.-W. Liu and Antzelevitch. Characteristics of the delayed rectifier current (I_{kr} and I_{ks}) in canine ventricular epicardial, midmyocardial, and endocardial myocytes. *Circ Res.*, 76:351–365, 1995.

[99] M. L. Koller, M. L. Riccio, and R. F. Gilmour. Dynamic restitution of action potential duration during electrical alternans and ventricular fibrillation. *Am. J. Physiol. Heart Circ. Physiol.*, 275:H1635–H1642, 1998.

[100] E. Lepeschkin and B. Surawicz. The measurement of the QT interval of the electrocardiogram. *Circulation,* 6:378–88, 1952.

[101] M. J. Janse, E. A. Sosunov, R. Coronel, T. Opthof, E. P. Anyukhovsky, J. M. T. De Bakker, A. N. Plotnikov, I. N. Shlapakova, P. Danilo, J. G. P. Tijssen, and M. R. Rosen. Repolarization gradients in the canine left ventricle before and after induction of short-term cardiac memory. *Circulation*, 112:1711–1718, 2005.

[102] P. G. A. Volders, K. Sipido, E. Carmeliet, R. L. Spatjens, H. J. Wellens, and M. A. Vos. Repolarizing K^+ currents I_{to} and I_{Ks} are larger in right than in left canine ventricular myocardium. *Circulation,* 99:206–210, 1999.

[103] C. Antzelevitch. Heterogeneity and cardiac arrhythmias: An overview. *Heart Rhythm*, 4(7):964–972, 2007.

[104] C. Antzelevitch. Role of spatial dispersion of repolarization in inherited and acquired sudden cardiac death syndromes. *Am. J. Physiol. Heart Circ. Physiol.*, 293:H2024–H2038, 2007.

[105] F. G. Akar, G. X. Yan, C. Antzelevitch, and D. S. Rosenbaum. Unique topographical distribution of M cells underlies reentrant mechanism of torsade de pointes in the long-QT syndrome. *Circulation*, 105:1247–53, 2002.

[106] C. Patel, J. F. Burke, H. Patel, P. Gupta, P. R. Kowey, C. Antzelevitch, and G.-X. Yan. Is there a significant transmural gradient in repolarization time in the intact heart? Cellular basis of the T wave. *Circ. Arrhythmia Electrophysiol.*, 2:80–88, 2009.

[107] T. Opthof, R. Coronel, and M. J. Janse. Is there a significant transmural gradient in repolarization time in the intact heart? Repolarization gradients in intact heart. *Circ. Arrhythmia Electrophysiol.*, 2:89–96, 2009.

[108] N. Ueda, D. P. Zipes, and J. Wu. Functional and transmural modulation of M cell behavior in canine ventricular wall. *Am. J. Physiol. Heart Circ. Physiol.*, 287:H2569–H2575, 2004.

[109] A. J. Pullan, M. L. Buist, and L. K. Cheng. *Mathematical modeling the electrical activity of the heart: from cell to body surface and back again*, World Sci. (2005).

[110] F. B. Sachse. *Computational Cardiology: Modeling of Anatomy, Electrophysiology, and Mechanics*, Springer, New York, 2004.

[111] K.H. ten Tusscher and A.V. Panfilov. Modelling of the ventricular conduction system. *Progr. Biophys. Mol. Biol.*, 96 (1-3): 152–170, 2008.

[112] P. E. McSharry, G. Clifford, L. Tarassenko, and L.A. Smith. A dynamical model for generating synthetic electrocardiogram signals. *IEEE Trans. Biomed. Eng.*, 50(3); 289–294, 2003.

[113] M. Gidea, C. Gidea, and W. Byrd, Deterministic models for simulating electrocardiographic signals. *Commun. Nonlin. Sci. Numer. Simul.*, 16(10): 3871–3880, 2011.

[114] N. Jafarnia-Dabanloo, D. C. McLernon, H. Zhang, A. Ayatollahi, and V. Johari-Majd. A modified Zeeman model for producing HRV signals and its application to ECG signal generation. *J. Theor. Biol*., 244(2): 180–189, 2007.

[115] W. Thanom and R. N. K. Loh. Nonlinear control of heartbeat models. *Syst. Cybern. Inform*., 9(1):21–27, 2011.

[116] J. Honerkamp. The heart as a system of coupled nonlinear oscillators. *J. Math. Biol*., 18(1): 69–88, 1983.

[117] S. Sato, S. Doi, and T. Nomura. Bonhoeffer–van der Pol oscillator model of the sino-atrial node: a possible mechanism of heart rate regulation. *Methods Inf. Med*., 33(1):116–119, 1994.

[118] R. L. Winslow, D. Cai, A. Varghese, and Y.-C. Lai. Generation and propagation of normal and abnormal pacemaker activity innetwork models of cardiac sinus node and atrium. *Chaos Solit. Fract*., 5(3-4): 491–512, 1995.

[119] M. G. Signorini, S. Cerutti, and D. Di Bernardo. Simulation of heartbeat dynamics: a nonlinear model. *Int. J. Bifurc. Chaos*, 8(08):1725–1731, 1998.

[120] D. Di Bernardo, M. G. Signorini, and S. Cerutti. A model of two nonlinear coupled oscillators for the study of heartbeat dynamics. *Int. J. Bifur. Chaos*, 8(08): 1975–1985, 1998.

[121] K. Grudzinski and J. J. Zebrowski. Modeling cardiac pacemakers with relaxation oscillators. *Physica A*, 336(1-2):153–162, 2004.

[122] A. M. Dos Santos, S. R. Lopes, and R. L. Viana. Rhythm synchronization and chaotic modulation of coupled van der Pol oscillators in a model for the heartbeat. *Physica A*, 338(3-4):335–355, 2004.

[123] M. Yoneyama and K. Kawahara. Coupled oscillator systems of cultured cardiac myocytes: fluctuation and scaling properties. *Phys. Rev. E*, 70:021904 (1–9), 2004.

[124] A. M. Dos Santos, S. R. Lopes, and R. L. Viana. Synchronization regimes for two coupled noisy Lienard-type driven oscillators. *Chaos Solit. Fract*., 36(4):901–910, 2008.

[125] B. Z. Kaplan, I. Gabay, G. Sarafian, and D. Safarian. Biological applications of the “filtered” van der Pol oscillator. *J. Frank.Inst*., 345(3):226–232, 2008.

[126] S. R. F. S. M. Gois and M. A. Savi. An analysis of heart rhythm dynamics using a three coupled oscillator model. *Chaos Solit. Fract*., 41(5):2553–2565, 2009.

[127] M. Suchorsky and R. Rand. Three oscillator model of the heartbeat generator. *Commun. Nonlin. Sci. Numer. Simul*., 14(5):2434–2449, 2009.

[128] S. Das and K. Maharatna. Fractional dynamical model for the generation of ECG like signals from filtered coupled van-der Pol oscillators. *Comput. Methods Prog. Biomed*., 112(3):490–507, 2013.

[129] F. A. Roberge, P. Bhereur, and R. A. Nadeau. A cardiac pacemaker model. *Med. Biol. Eng*., 9(1):3–12, 1971.

[130] O. Kongas, R. von Hertzen, and J. Engelbrecht. Bifurcation structure of a periodically driven nerve pulse equation modeling cardiac conduction. *Chaos Solit. Fract*., 10(1):119–136, 1999.

[131] J. J. Zebrowski, K. Grudzinski, T. Buchner, P. Kuklik, J. Gac, G. Gielerak, P. Sanders, and R. Baranowski. Nonlinear oscillator model reproducing various phenomena in the dynamics of the conduction system of the heart. *Chaos*, 17 (1):015121(1–10), 2007.

[132] H. Sheheitli and R. Rand. Origin of arrhythmias in a heart model. *Commun. Nonlin. Sci. Numer. Simul*., 14:3707–3714, 2009.

[133] B. Van der Pol and J. van der Mark. The heartbeat considered as a relaxation oscillation, and an electrical model of the heart. *Philos. Mag*., 6 (1928) 763–775.

[134] E. Ryzhii and M. Ryzhii. Modeling of heartbeat dynamics with a system of coupled nonlinear oscillators. *Commun. Comput. Inform. Sci*., 404:67–75, 2014.

[135] C. Morris and H. Lecar. Voltage oscillations in the barnacle giant muscle fiber. *Biophys. J*., 35(1):193–213, 1981.

[136] D. Postnov, S. K. Han, and S. Kook. Synchronization of diffusively coupled oscillators near the homoclinic bifurcation. *Phys. Rev. E*, 60(3):2799–2807, 1999.

[137] S. Wirkus and R. Rand. The dynamics of two coupled van der Pol oscillators with delay coupling. *Nonlin. Dyn.*, 30(3):205–221, 2002.

[138] O. Kongas, R. von Hertzen, and J. Engelbrecht. Bifurcation structure of a periodically driven nerve pulse equation modeling cardiac conduction. *Chaos Solit. Fract.*, 10(1):119–136, 1999.

[139] R. FitzHugh. Impulses and physiological states in theoretical models of nerve membrane. *Biophys. J.*, 1(6):445–466, 1961.

[140] J. Nagumo, S. Arimoto, and S. Yoshizawa. An active pulse transmission line simulating nerve axon. *Proc. IRE.*, 50(10):2061–2070, 1962.

[141] L. F. Shampine and S. Thompson. Solving DDEs in MATLAB. *Appl. Num. Math.*, 37(4):441–458, 2001.

[142] J. Kierzenka, L. F. Shampine, and S. Thompson. Solving delay differential equations with DDE23. *http://www.mathworks.com/dde_tutorial* .

[143] EKG refresh and practice. *http://www.chicago.medicine.uic.edu* .

[144] M. R. Boyett, H. Honjo, and I. Kodama. The sinoatrial node, a heterogeneous pacemaker structure. *Cardiovasc. Res.*, 47(4):658–687, 2000.

[145] F. L. Meijler and M. J. Janse. Morphology and electrophysiology of the mammalian atrioventricular node. *Physiol. Rev.*, 68(2):608–647, 1988.

[146] P.A. Boyden, M. Hirose, and W. Dun. Cardiac Purkinje cells. *Heart Rhythm.*, 7(1):127–135, 2010.

[147] J. M. Rogers and A. D. McCulloch. A collocation-Galerkin finite element model of cardiac action potential propagation. *IEEE Trans. Biomed. Eng.*, 41(8):743–757, 1994.

[148] Illustrated book on electrocardiography. Cardiophile MD, *http://cardiophile.org/electrocardiography/* .

[149] V. Fuster, R. A. Walsh, and R. A. Harrington. *Hurst's the Heart*. 13th ed., McGrow Hill Medical, New York, 2011.

[150] R. J. Bauer and G. Mo, W. Krzyzanski. Solving delay differential equations in S-ADAPT by method of steps. *Comput.Methods Prog. Biomed*., 111(3):715–734, 2013.

[151] E. Ryzhii and M. Ryzhii. A heterogeneous coupled oscillator model for simulation of ECG signals. *Comput. Methods Programs Biomed*., 117(1):40–49, 2014.

[152] M. Mase, L. Glass, M. Disertori, and F. Ravelli. Nodal recovery, dual pathway physiology, and concealed conduction determine complex AV dynamics in human atrial tachyarrhythmias. *Am. J. Physiol. Heart Circ. Physiol*., 303: H1219–H1228, 2012.

[153] G. W. Beeler and H. Reuter. Reconstruction of the action potential of ventricular myocardial fibers. *J. Physiol.*, 268:177–210, 1977.

[154] M. Nabauer, D. J. Beuckelmann, P. Uberfuhr, and G. Steinbeck. Regional differences in current density and rate-dependent properties of the transient outward current in subepicardial and subendocardial myocytes of human left ventricle. *Circulation*, 93:168–177, 1996.

[155] E. Wettwer, G. J. Amos, H. Posival, and U. Ravens. Transient outward current in human ventricular myocytes of subepicardial and subendocardial origin. *Circ. Res.*, 75:473–482, 1994.

[156] M. Courtemanche, R. J. Ramirez, and S. Nattel. Ionic mechanisms underlying human atrial action potential properties: insights from a mathematical model. *Am. J. Physiol. Heart Circ. Physiol.*, 275:H301–H321, 1998.

Biography

Elena Ryzhii was born in Russia, Moscow in 1968. She received Medical Doctor degree (MD) in 1992, Residency (Pediatric) in 1994 in Moscow Medical Academy, Russia. From 2007-2010 she was a PhD student in Graduate Department of Information system in University of Aizu, Japan. Now she is pursuing the PhD degree at Tohoku University. Her research interests include computer simulations of electrical cardiac activity by means of whole heart, ion-channel, oscillators model, studying arrhythmias and influence of electromagnetic radiation on the cardiac electrical activity.

List of publications

Journals

[J1] E. Ryzhii and D. Wei, "Computer simulation of atypical Brugada syndrome," *Journal of Electrocardiology*, vol. 42(4), pp. 319–327, July-August 2009 (DOI:10.1016/j.jelectrocard.2008.12.015).

[J2] E. Ryzhii, "Investigation of spatial action potential distributions in myocardium using three-dimensional biventricular heart model," *Journal of Communication Technology and Electronics*, vol. 57(1), pp. 87-96, January 2012 (DOI:10.1134/S1064226911120230).

[J3] E. Ryzhii and M. Ryzhii, "A heterogeneous coupled oscillator model for simulation of ECG signals," *Computer Methods and Programs in Biomedicine*, vol. 117(1), pp. 40-49, October 2014 (DOI:10.1016/j.cmpb.2014.04.009).

Conferences

[C1] E. Ryzhii and D. Wei, "Simulation of atypical Brugada syndrome using the whole-heart model," *Circulation Journal*, vol. 72, suppl. 1, p. 378, 2008 *The 72nd Annual Scientific Meeting of the Japanese Circulation Society* (JCS 2008), Fukuoka, Japan, 28-30 March, 2008.

[C2] D. Wei, S. Hasegawa, K. Takahashi, E. Ryzhii, and X. Zhu, "A virtual reality for catheter-based EPS based on whole-heart model," *International Journal of Bioelectromagnetism*, vol. 11(1), pp. 2-6, 2009; *The 7th International Symposium on Noninvasive Functional Source Imaging of the Brain and Heart* & *The 7th International Conference on Bioelectromagnetism* (NFCI & ICBEM 2009), Rome, Italy, 29-31 May, 2009.

[C3] E. Ryzhii, M. Ryzhii, and D. Wei, "Computer simulation study of gender differences in cardiac repolarization: normal case and the Brugada syndrome," *The*

13th Congress of the International Society for Holter and Noninvasive Electrocardiology (ISHNE 2009), Yokohama, Japan, 4-6 June, 2009.

[C4] E. Ryzhii, M. Ryzhii, and D. Wei, "Extension of whole-heart model by coupling with human ventricular cell model," *Progress in Electromagnetics Research Symposium* (PIERS 2009), Key: 09023012131, Moscow, Russia, 18-21 August, 2009.

[C5] E. Ryzhii and M. Ryzhii. "Heterogeneous oscillator model of cardiac conduction system", *Progress in Electromagnetic Research Symposium* (PIERS 2013), Key: 130319055945, Stockholm, Sweden, 12-15 August, 2013.

[C6] E. Ryzhii and M. Ryzhii, "Modeling of heartbeat dynamics with a system of coupled nonlinear oscillators," *Communications in Computer and Information Science*, vol. 404, pp. 67-75, 2014 (DOI: 10.1007/978-3-642-54121-6_6); *The 1st International Aizu Conference on Biomedical Informatics and Technology* (ACBIT 2013), Aizu-Wakamatsu, Japan, 16-17 September, 2013.

[C7] E. Ryzhii, M. Ryzhii, and V. Savchenko, "Effect of coupling on the pacemaker synchronization in coupled oscillator ECG model," in *Proceedins of 2014 IEEE International Conference on Biomedical Engineering and Sciences (IECBES 2014),* Miri, Malaysia, 8-10 December, pp. 281–286.

[C8] E. Ryzhii and M. Ryzhii, "Response of oscillator model of cardiac conduction system on modulated electromagnetic radiation," *Progress in Electromagnetic Research Symposium*, (PIERS2015), Key: 150205062540, Prague, Czech Republic, 6-9 July, 2015.

[C9] E. Ryzhii and M. Ryzhii, "Formation of second-degree atrioventricular blocks in the cardiac heterogeneous oscillator model," *The 37th Annual International Conference of the IEEE Engineering in Medicine and Biology Society* (EMBC15), Milan, Italy, 25-29 August, 2015 (accepted).

Acknowledgment

I would like to express my deep appreciation to my first research supervisor, Professor Daming Wei, for offering me an opportunity of doing this research work at the Biomedical Information Technology (BIT) laboratory of the University of Aizu, for my education on computer science methods and for his introduction to biomedical modeling. I would also like to thank other BIT laboratory members for their continuous encouragement and support which have been important for me.

I will be forever thankful to Professor Yoshifumi Saijo (Chairman of the thesis examination committee) for taking the role of my second supervisor and mentor, and for all his invaluble help and guidance.

I would like to thank Professors Shin-ichiro Umemura and Makoto Yoshizawa for serving on my thesis committee, for taking the time to read my thesis and for offering their brillant comments and suggestions.

I extend my many thanks to Professor Taiichi Otsuji for his extraordinary moral support, for his competent advices and for great efforts related with this thesis.

I owe my deepest gratitude to my parents and my parents in law for their love and encouragement in my life.

Finally, I wish to express my heartfelt gratitude to my fellow researcher, dear husband, not only for help with the computer modeling, but for his own patience, understanding, and support throughout all this work, and for bringing happiness and meaning to my everyday life.